

# The erosion of large primary atmospheres typically leaves behind substantial secondary atmospheres on temperate rocky planets

---

Received: 5 December 2023

---

Accepted: 13 September 2024

---

Published online: 27 September 2024

---

 Check for updates

---

Joshua Krissansen-Totton <sup>1,2</sup> ✉, Nicholas Wogan <sup>2,3</sup>, Maggie Thompson<sup>4,5</sup> & Jonathan J. Fortney<sup>6</sup>

Exoplanet exploration has revealed that many—perhaps most—terrestrial exoplanets formed with substantial H<sub>2</sub>-rich envelopes, seemingly in contrast to solar system terrestrials, for which there is scant evidence of long-lived primary atmospheres. It is not known how a long-lived primary atmosphere might affect the subsequent habitability prospects of terrestrial exoplanets. Here, we present a new, self-consistent evolutionary model of the transition from primary to secondary atmospheres. The model incorporates all Fe-C-O-H-bearing species and simulates magma ocean solidification, radiative-convective climate, thermal escape, and mantle redox evolution. For our illustrative example TRAPPIST-1, our model strongly favors atmosphere retention for the habitable zone planet TRAPPIST-1e. In contrast, the same model predicts a comparatively thin atmosphere for the Venus-analog TRAPPIST-1b, which would be vulnerable to complete erosion via non-thermal escape and is consistent with JWST observations. More broadly, we conclude that the erosion of primary atmospheres typically does not preclude surface habitability, and frequently results in large surface water inventories due to the reduction of FeO by H<sub>2</sub>.

Understanding the distribution of life in the Universe is inextricably linked to whether Earth's long-term habitability is a rare or common feature of habitable zone terrestrial planets. One potentially underexplored dimension of exceptionalness is the ways in which initial volatile inventories may shape subsequent geochemical evolution to preclude (or enhance) long-term habitability. The Kepler era of exoplanet exploration revealed two distinct types of planets of an intermediate size with no solar system analog: volatile-rich sub-Neptunes ( $R > \sim 1.7R_E$ ) and terrestrial-density super-Earths ( $R \leq \sim 1.7R_E$ ). While sub-Neptune bulk composition (H<sub>2</sub>, H<sub>2</sub>O, etc.) is a subject of ongoing investigation, and the possibility of different formation pathways for super-Earths and sub-Neptunes has not been discounted<sup>1–5</sup>, there is evidence that these two planetary types derive from the same volatile-

rich parent population: super-Earths arise from the complete erosion of primary atmospheres, whereas sub-Neptunes have retained a substantial portion of their primary atmospheres<sup>6</sup>. The dominant mechanism for primary atmosphere erosion remains a topic of debate, but extreme ultraviolet (XUV) driven atmospheric escape and mass loss driven by interior heat flow both offer plausible explanations<sup>7–12</sup>. One important implication of this population-level understanding is that many—perhaps most—now-rocky exoplanets formed with substantial, long-lived primary atmospheres. This is broadly consistent with theoretical expectations that rapidly accreted terrestrial bodies ought to capture nebular gas<sup>13,14</sup>.

Crucially, however, the abovementioned formation pathway for super-Earths is distinct from that of the Earth and other solar system

---

<sup>1</sup>Department of Earth and Space Sciences/Astrobiology Program, University of Washington, Seattle, WA 98195, USA. <sup>2</sup>NASA NExSS Virtual Planetary Laboratory, University of Washington, Seattle, WA 98195, USA. <sup>3</sup>NASA Ames Research Center, Moffett Field, CA 94035, USA. <sup>4</sup>Department of Earth and Planetary Sciences, ETH Zurich, Zürich, Switzerland. <sup>5</sup>NASA Hubble Fellowship Program Sagan Fellow, Earth and Planets Laboratory, Carnegie Institution for Science, Washington DC 20015, USA. <sup>6</sup>Department of Astronomy and Astrophysics, University of California, Santa Cruz, Santa Cruz, CA 95064, USA.

✉ e-mail: [jshkt@uw.edu](mailto:jshkt@uw.edu)

terrestrial planets, for which there is no evidence of prolonged initial H<sub>2</sub>-rich envelopes, and limited evidence for nebula capture of volatiles<sup>15,16</sup>. Instead, the volatile endowments of solar system terrestrial bodies were sourced from chondritic material, perhaps with some small volatile contribution from planetesimals that formed beyond the snow line<sup>17–19</sup>. Recently, Young, et al.<sup>20</sup> argued that Earth's water inventory, oxygen fugacity, and core density can be explained by thermochemical equilibration between primordial H<sub>2</sub> and the rocky embryos that ultimately built Earth, but the extent to which this intriguing hypothesis can be reconciled with isotopic tracers of Earth's accretion has yet to be fully explored.

Distinct formation pathways for solar system terrestrials and exoplanets raise an important question: how might the presence of a long-lived primary atmosphere affect the subsequent habitability prospects of rocky exoplanets, given that solar system terrestrial bodies may have obtained their volatile endowments in an atypical manner? Now that atmospheric characterization of rocky planets around M-dwarfs is possible with JWST, an understanding of how primary atmospheres affect secondary atmosphere evolution is needed. There have been preliminary investigations on this topic<sup>21,22</sup>. In particular, Kite and Barnett<sup>23</sup> argued that XUV-driven loss of primary atmospheres will typically drag along high molecular weight volatiles, leaving behind a desiccated terrestrial planet, unless surface volatiles are replenished by mantle degassing. While instructive, these calculations are most applicable to highly irradiated (uninhabitable) planets and treat all non-hydrogen species as a single high molecular weight composite. Note that this escape process is inseparable from the thermal evolution of the post-accretional magma ocean; terrestrial planets are expected to form hot, and volatiles are partitioned between the partially molten mantle and atmosphere during early evolution. There has been no self-consistent investigation of how high molecular weight volatile element inventories partition and escape during primary atmosphere loss, or whether temperate terrestrial exoplanets that previously possessed a thick primary atmosphere would retain sufficient volatiles to sustain a biosphere.

Indeed, classical models of magma ocean thermal-climate-redox evolution are typically limited to H<sub>2</sub>O and CO<sub>2</sub> (and occasionally O<sub>2</sub>) bulk atmospheric compositions<sup>24–28</sup>. This assumption of a relatively oxidizing atmosphere is based on evidence for Earth's rapid differentiation and mantle oxidation after accretion<sup>29,30</sup>, along with the absence of any evidence for a long-lived H<sub>2</sub>-rich atmosphere<sup>15</sup>. Attempts to extrapolate these Earth-analog models to terrestrial exoplanets<sup>26,28,31</sup> typically ignore any H<sub>2</sub>-rich initial atmosphere under the assumption that such atmospheres are too short-lived to affect subsequent evolution. In recent years, more generalized magma ocean models have been developed that can accommodate diverse redox chemistries and atmospheric compositions<sup>32–35</sup>. This body of work suggests a broader range of magma ocean atmospheres are possible, even for literal Earth twins. However, there has yet to be a self-consistent investigation of magma ocean evolution accommodating the reducing power of an initial H<sub>2</sub> envelope coupled to secular oxidation caused by XUV-driven escape, to investigate the transition from primary to secondary atmospheres.

Here, we present the first such self-consistent model of coupled magma ocean–redox–climate evolution. We are particularly interested in planetary volatile inventories post primary atmosphere loss, and the implied habitability prospects for terrestrial planets that formed with large nebular atmospheres. Planetary volatile inventories can significantly influence long-term habitability prospects of terrestrial planets. For example, planetary carbon inventories affect climate-stabilizing silicate weathering feedbacks<sup>36,37</sup> and even mantle dynamics and melt production<sup>38</sup>. Similarly, large water inventories affect redox evolution<sup>28,39</sup>, resulting in abiotic oxygen-rich atmospheres that are not conducive to abiogenesis<sup>40</sup>. Large water inventories may also suppress carbon cycle feedbacks with implications for surface climate evolution<sup>41</sup>. If the loss of a primary atmosphere systematically modifies

planetary volatile inventories, then the subsequent geochemical cycling of terrestrial exoplanets might be dramatically affected in observable ways, even billions of years after their primary atmospheres have been eroded. In what follows, we present a generalized, coupled atmosphere-interior evolution model to investigate the astrobiological legacy of primary atmospheres and to make testable predictions on the habitability prospects of rocky exoplanets for space-based observations.

## Results

### Modeling Approach

Figure 1 shows a schematic of the new model used in this study, PACMAN-P (PACMAN for Primary atmospheres). This is a significant upgrade to the original PACMAN model described in Krissansen-Totton and Fortney<sup>42</sup>. The subsections in the Methods section describe the individual components of the model, but broadly speaking we simultaneously solve for geochemical and thermal equilibrium as the magma ocean solidifies from the core-mantle boundary to the surface. At each time step, we find the multiphase equilibrium of all C, H, O, and Fe-bearing species between the atmosphere and the magma ocean. The resulting atmospheric species determine surface temperature, as calculated using a radiative-convective climate model that balances absorbed stellar radiation, outgoing longwave radiation, and internal heatflow. Internal heatflow is determined by parameterized mantle convection with temperature-dependent mantle viscosity, and driven by the heat of accretion, assumed radionuclides, and the latent heat of mantle solidification. Imposed stellar bolometric and XUV evolution—including a super luminous pre-main sequence—drives atmospheric escape, which is either XUV-limited or diffusion limited, depending on the composition of the upper atmosphere (computed via the climate model). Crucially, C-bearing and O-bearing species can be lost to space via hydrodynamic drag in the XUV-limited regime. We do not attempt to model atmosphere-interior interactions after the magma ocean has solidified, but we do continue to track stellar evolution and consequent atmospheric escape. To generate imminently testable predictions, we use TRAPPIST-1e and b<sup>43</sup> as case studies in all model calculations, but we note that qualitative model behavior is general to all temperate planets that form with substantial nebular atmospheres. Example calculations for other planetary systems (as well as Earth + Venus validation calculations) are presented in supplementary materials. A Monte Carlo approach is used to investigate sensitivity to initial volatile inventories, and uncertainties in stellar evolution, atmospheric escape, and other planetary parameters.

### TRAPPIST-1 simulations

Figure 2 shows the time evolution of TRAPPIST-1e for an approximately Bulk Silicate Earth (BSE)-like initial volatile endowment (i.e. no large H<sub>2</sub> envelope), an Earth-like mantle FeO abundance, and nominal point estimates for all other parameters (see Methods). Figure 2a shows the evolution of surface and mantle temperature, Fig. 2b shows the planetary energy budget consisting of OLR, ASR, and interior heatflow, Fig. 2c shows the solidification radius as it moves from the core-mantle boundary to the surface. Figure 2d shows the evolution of the oxygen fugacity of the magma ocean and growing solid mantle, Fig. 2e shows the evolution of atmospheric composition, and Fig. 2f–h, and i show inventories of Fe, H, C, and O respectively (and Figs. 3, 4, S1, and S2 follow the same layout). Mass is conserved except for H, C, and O-bearing species lost to thermal escape. The dashed vertical line in all subplots denotes the termination of the magma ocean i.e. when surface temperature drops below the solidus. After the termination of the magma ocean, only stellar evolution and atmospheric escape continue—there is no further chemical interaction between surface volatiles and the silicate interior, though solid mantle redox state does evolve with mantle temperature. The model is therefore conservative regarding habitability prospects since, in reality, surface volatile reservoirs will be

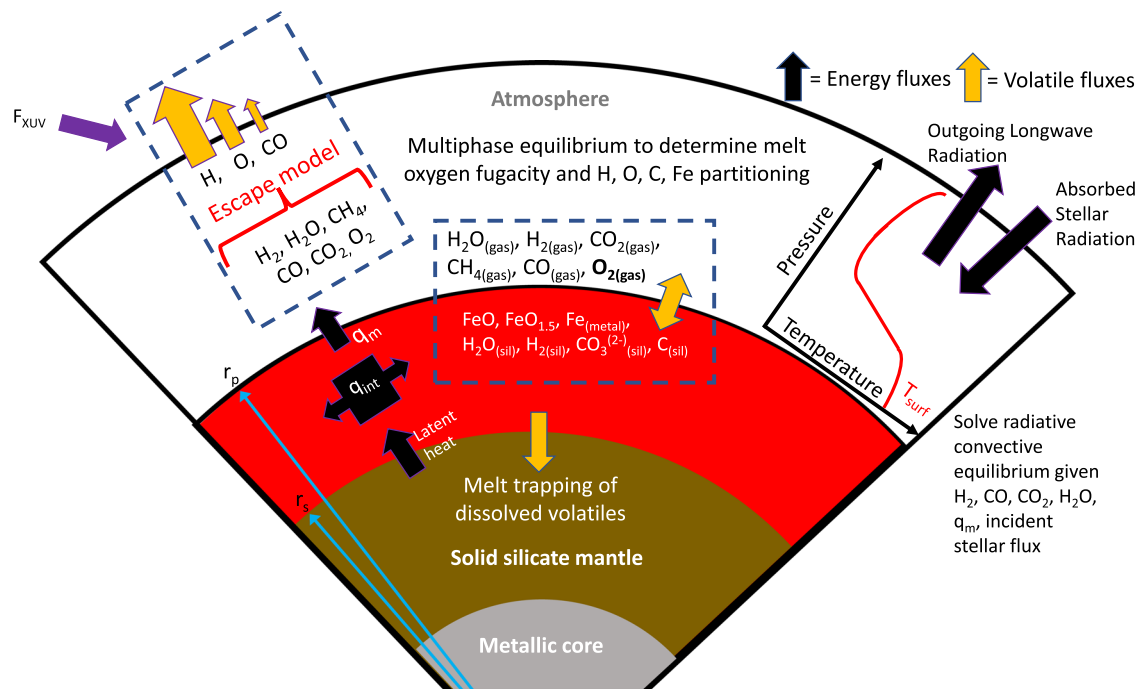


**Fig. 1 | Schematic overview of coupled redox-atmosphere-interior evolution model, PACMAN-P.** The model is initialized with a completely molten mantle, and the solidification radius,  $r_s$ , evolves from the core-mantle boundary to the surface,  $r_p$ , as the planet cools. At each timestep, we calculate multiphase thermochemical equilibrium between C, H, O, and Fe-bearing species to find the mantle redox state and the partitioning of volatiles between the magma ocean and the atmosphere. Surface climate,  $T_{surf}$ , is calculated using a radiative-convective model given

atmospheric volatile inventories. Under highly reducing conditions created by large  $H_2$  envelopes, the reaction of  $H_2$  with the silicate magma ocean produces metallic iron, that is either sequestered in the core or remains in the mantle (two endmember assumptions). Atmospheric escape is either XUV-limited or diffusion limited depending on stratospheric composition, and under the former regime we calculate the hydrodynamic drag of O and CO.

replenished by magmatic degassing after magma ocean solidification. No metallic iron is produced in this comparatively oxidized scenario.

In this example calculation for TRAPPIST-1e, the atmosphere is dominated by CO and  $CO_2$  throughout the planet's evolution due to the high solubility of water in silicate melts and comparatively low BSE-like H abundance (equivalent to a few Earth oceans). During the magma ocean stage, the atmosphere evolves from CO-dominated to  $CO_2$ -dominated, in part due to secular cooling, but also because H loss when the magma ocean is shallow (large solidification radius) oxidizes the melt-atmosphere system. The magma ocean ends after only a few  $\sim 10^7$  years because there is insufficient water to maintain surface temperatures above the solidus; the planet remains in a runaway greenhouse state for longer, but there is insufficient greenhouse warming from  $CO_2$  (with modest amounts of  $H_2O$  and  $H_2$ ) to keep the surface molten. The remaining water vapor is mostly lost to space, leaving behind a  $CO_2$ - $O_2$  atmosphere, where the  $O_2$  is a consequence of H escape post magma ocean solidification (reduced atmospheric species like CO,  $CH_4$ , and  $H_2$  are oxidized to  $CO_2$  and  $H_2O$ ). Atmospheric  $H_2O$  is not lost completely because a cold trap is established as stellar bolometric luminosity falls. It is conceivable that water degassing post magma ocean solidification could transition this planet to a habitable state, as more than an Earth ocean is retained in the solid mantle and comparatively little C is lost to escape; whether surface liquid water can be stabilized depends on the balance of water degassing and atmospheric escape during the remaining pre-main sequence<sup>44</sup>. Suffice to say habitability is a possible outcome, but by no means guaranteed for this BSE-like initial condition.

Next, we consider the exact same scenario, except that TRAPPIST-1e is endowed with a substantial (0.1% planetary mass) initial  $H_2$  envelope on top of the BSE-like volatile endowment (Fig. 3). Note that the additional C and O associated with a nebular atmosphere (assuming solar C:H and O:H) would not dramatically alter our assumed initial

carbon and free oxygen inventories<sup>45</sup>. In this case, we make the end-member assumption that all metallic iron formed by the reduction of FeO is retained in the mantle, but results are qualitatively similar for the opposite case where all metallic iron is sequestered in the core (see below). In Fig. 3, the large  $H_2$  endowment results in a much longer-lived magma ocean (a few  $\sim 10^8$  years) due to the strong greenhouse warming from the  $H_2 + H_2O$  atmosphere. The atmosphere is  $H_2$ -dominated during the magma ocean phase (Fig. 3e), but later transitions to water-dominated due to oxidation from H loss and water exsolution from the magma ocean. Exsolved water is predominantly a byproduct of the reduction of the mantle by the nebular atmosphere,  $FeO + H_2 \rightarrow H_2O + Fe$ . Note that atmospheric H increases during rapid stages of magma ocean solidification even though total planetary H is decreasing because the exsolution of water melt is more rapid than H escape, but during the final (slow) stages of solidification, both planetary H and atmospheric H decline. A reducing,  $H_2$ -dominated ( $CH_4$ -rich) atmosphere persists briefly after magma ocean solidification, and a solidified TRAPPIST-1e transitions to a habitable state (Fig. 3a) with a deep ( $\sim 20$  km) surface ocean. Shortly after, cumulative H escape flips the redox balance of the surface to net oxidized ( $H_2O$ - $CO_2$ - $O_2$ ) and a  $CO_2$ - $O_2$  dominated atmosphere persists as most water is condensed on the surface (Fig. 3e). While some carbon is lost to escape during the pre-main sequence (Fig. 3h), a large  $CO_2$  inventory remains that could be sequestered as carbonates and enable a silicate weathering thermostat.

We contrast this habitable outcome for TRAPPIST-1e to the magma ocean evolution of TRAPPIST-1b (Fig. 4) with the identical initial composition (0.1% nebular atmosphere, Earth-like initial FeO, etc.), and the same endmember assumption whereby all metallic iron remains in the mantle. Here, the magma ocean persists until virtually all fluid H is lost to space (Fig. 4e) due to higher received bolometric and XUV fluxes. Essentially all planetary carbon is lost to space

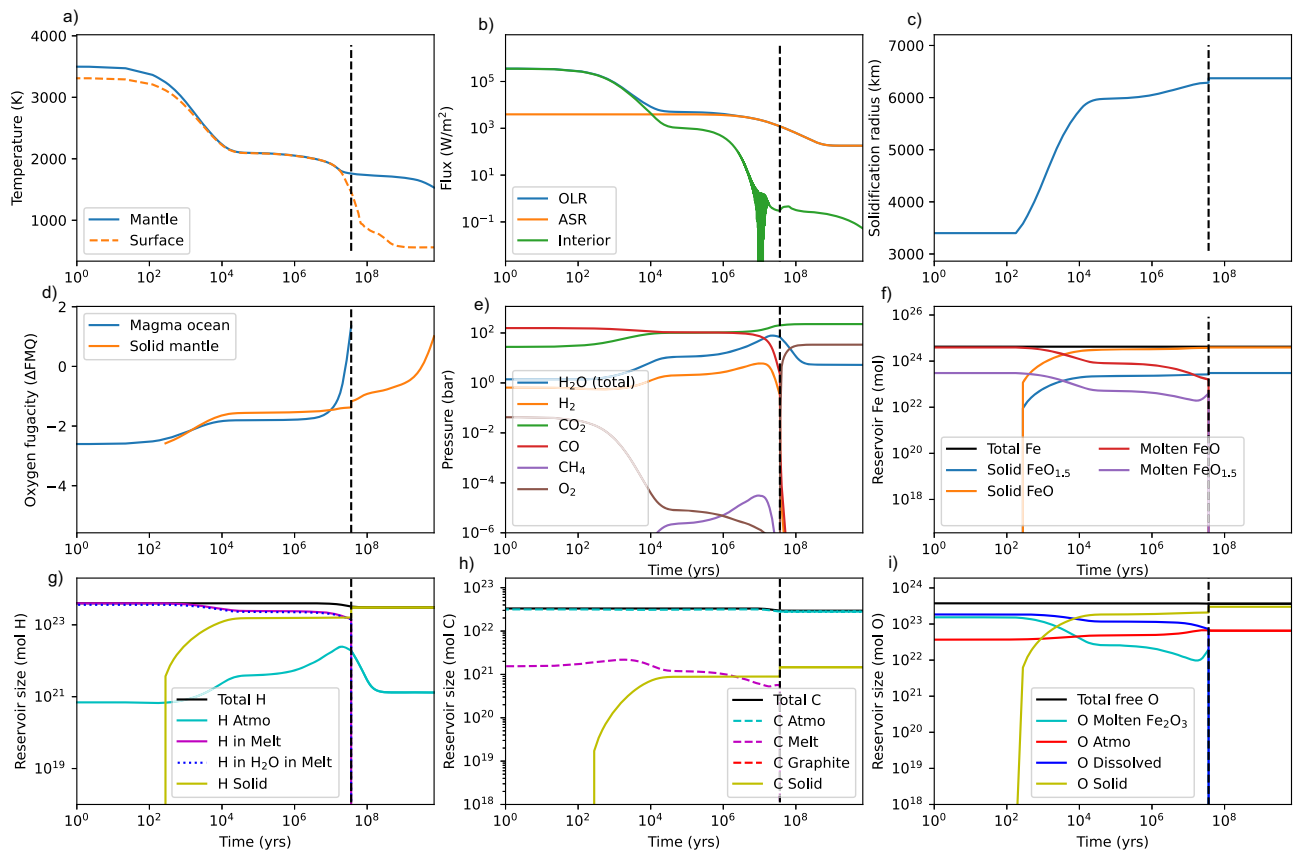


**Fig. 2 | Time-evolution of TRAPPIST-1e, with Earth-like initial volatile inventories (no substantial primary atmosphere) from post-accretion magma ocean to present (8 Gyr).** Subplot (a) denotes the time-evolution of surface (orange) and mantle potential temperature (blue), (b) denotes the evolution of outgoing long-wave radiation (OLR, blue), absorbed shortwave radiation (ASR, orange), and interior heatflow (green), and subplot (c) shows the evolution of the magma ocean solidification front from the core-mantle boundary to the surface. Subplot (d) shows solid mantle (orange) and magma ocean redox (blue) relative to the Fayalite-Quartz-Magnetite (FMQ) buffer, (e) shows the evolution of atmospheric composition including  $\text{H}_2\text{O}$ ,  $\text{H}_2$ ,  $\text{CO}_2$ ,  $\text{CO}$ ,  $\text{CH}_4$ , and  $\text{O}_2$ . Subplot (f) denotes iron speciation in both the magma ocean and the solid silicate mantle—in this oxidizing Earth-analog case no metallic iron is produced. Subplot (g) shows both solid and fluid reservoirs

of H; total dissolved hydrogen (purple) and hydrogen dissolved as  $\text{H}_2\text{O}$  (blue-dotted) are essentially identical in this oxidized scenario where dissolved  $\text{H}_2$  is minimal. Subplot (h) denotes solid and fluid reservoirs of C and subplot (i) denotes solid and fluid reservoirs of free oxygen, including oxygen bound to ferric iron, atmospheric species, and O in volatiles dissolved in the melt ( $\text{H}_2\text{O}$ ,  $\text{CO}_2$ ) reservoirs, respectively. Vertical dashed black lines show the termination of the magma ocean, which takes  $\sim 4 \times 10^7$  years in this case. The short duration of the magma ocean is attributable to the small H inventory, which in turn means limited time for the hydrodynamic drag of C and O; substantial C and O inventories are retained post-magma ocean solidification, and subsequent habitability is not precluded. Note that we do not explicitly model mantle-atmosphere exchange after magma ocean solidification, only escape and stellar evolution.

(Fig. 4h), consistent with previous predictions for highly irradiated terrestrial planets<sup>23</sup>. After the magma ocean ends, TRAPPIST-1b is left with a comparatively tenuous ( $\sim$ few bar)  $\text{O}_2$  atmosphere that would likely be highly susceptible to non-thermal escape<sup>46–49</sup>, which we do not consider here. Carbon is lost more completely than oxygen due to the low solubilities of C-bearing species in silicate melts. The small mantle volatile content implies limited potential for replenishing the atmosphere of TRAPPIST-1b by volcanic degassing. Results are qualitatively similar if all metallic iron is assumed to be sequestered in the core (Fig. S7), except that the final mantle redox state is around FMQ + 4 as opposed to FMQ-3 and a more substantial  $\text{O}_2$  atmosphere remains.

### Monte Carlo Analysis

To systematically map out the parameter space of possible evolutionary pathways from primary to secondary atmospheres, we conducted Monte Carlo analyses of the evolution of TRAPPIST-1e (and b) over a broad range of initial conditions, escape, and stellar evolution parameters (see Methods). We focus on initial nebular atmospheres (yielding endogenous water) as opposed to water-rich bulk compositions due to ice accretion to be conservative with respect to atmospheric retention prospects. Figure 5 shows the outcome of these

Monte Carlo calculations as a function of initial  $\text{H}_2$ , which ranges from an order of magnitude below Bulk Silicate Earth (BSE) all the way up to a substantial (1–2 wt% H) nebular atmosphere. The first two columns denote TRAPPIST-1e and the last two columns denote TRAPPIST-1b outputs; the two columns for each planet represent endmember cases whereby all metallic iron is sequestered in the core, and all metallic iron remains in the silicate mantle, respectively. The four rows show final total atmospheric pressure, partial pressures of surface volatiles, final carbon inventories, and final hydrogen inventories, respectively.

The outputs for TRAPPIST-1e reveal that, after 8 Gyr of evolution, a large surface inventory of water remains for planets with substantial ( $>$ BSE) initial H inventories. A Venus-like  $\text{CO}_2$ -dominated atmosphere remains for smaller initial H inventories. The median final planetary carbon inventory for TRAPPIST-1e is comparable to BSE abundances (i.e. most carbon is typically retained and not lost via hydrodynamic drag). We do not consider initial H inventories beyond  $\sim 10^{23}$  kg ( $\sim 2$  wt%) since TRAPPIST-1e often retains H-rich atmospheres for its entire 8 Gyr evolution in these cases, in conflict with observations<sup>50</sup>. For TRAPPIST-1b, a thinner,  $\text{O}_2$ -dominated atmosphere is the most common outcome across a broad range of initial H inventories. Final planetary carbon inventories are typically orders of magnitude lower than for TRAPPIST-1e due to more protracted hydrodynamic drag and

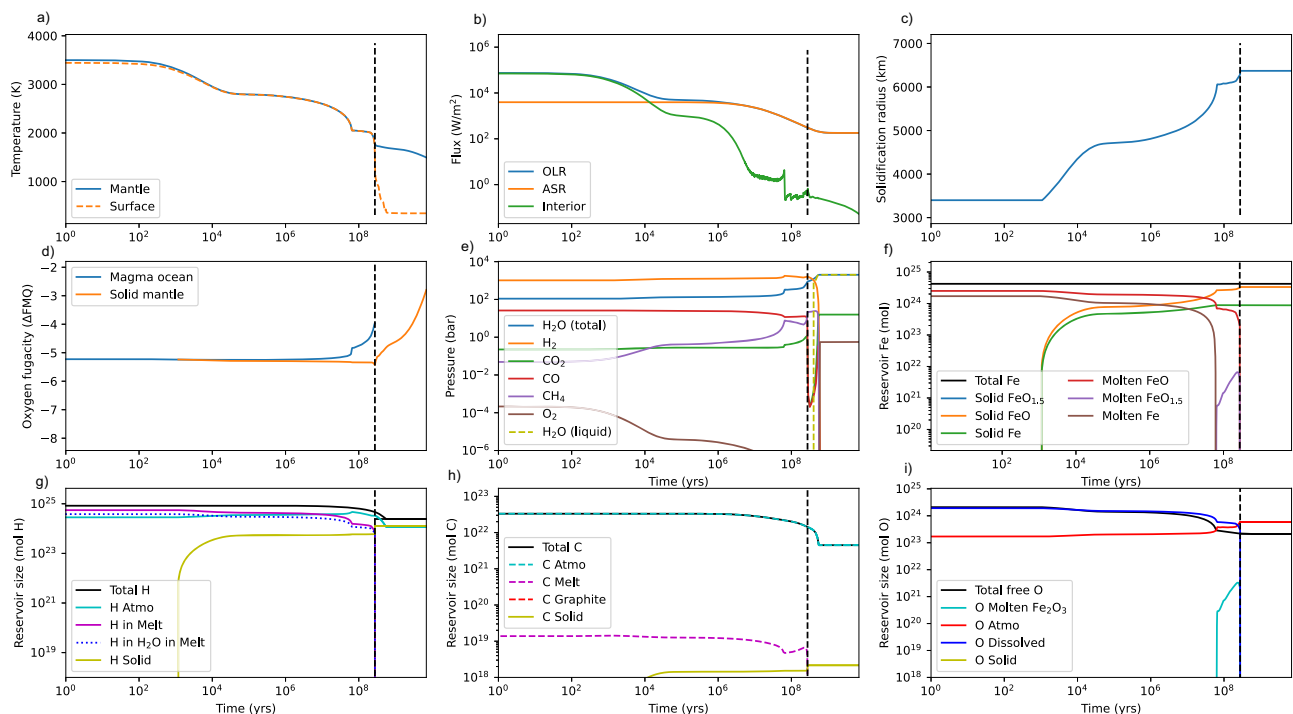


**Fig. 3 | Time-evolution of TRAPPIST-1e, with a large initial H<sub>2</sub> envelope from post-accretion magma ocean to present (8 Gyr).** Subplot (a)–(i) are identical to those in Fig. 2. In this case, an H<sub>2</sub>-dominated atmosphere persists for the duration of the magma ocean (e). Vertical dashed black lines show the termination of the magma ocean, which takes  $\sim 3 \times 10^8$  years in this case. The longer duration of the magma ocean is attributable to the large H inventory, which in turn means more time for the hydrodynamic drag of C and O; nonetheless substantial H (g), C (h), and O (i) inventories are retained post magma ocean solidification, and subsequent

habitability is not precluded. In fact, reaction of H<sub>2</sub> with the silicate magma ocean generates abundant H<sub>2</sub>O that ultimately forms a deep surface ocean ( $\sim 7$  Earth oceans). In this particular case, we make the endmember assumption that all metallic iron generated by the reaction of FeO and H<sub>2</sub> remains in the mantle, and so metallic species are present in (f). The atmospheric outcomes are qualitatively similar if all metallic iron is assumed to be sequestered in the core (see Fig. S6). Note that we do not explicitly model mantle-atmosphere exchange after magma ocean solidification, only escape and stellar evolution.

higher XUV fluxes during the pre-main sequence. TRAPPIST-1b is often completely desiccated after 8 Gyr of evolution with either no surface water (initial H  $< 3 \times 10^{21}$  kg) or limited water vapor in a dense O<sub>2</sub> atmosphere, and water in the silicate mantle that is an order of magnitude less than BSE.

Broadly speaking, the Monte Carlo results shown in Fig. 5 confirm what was suggested by the illustrative cases above (Figs. 2–4). The reaction of a hydrogen-rich primary atmosphere with the silicate mantle produces water rich composition for both planets (see also Kimura and Ikoma<sup>51</sup>, Kimura and Ikoma<sup>52</sup>). The comparatively short runaway greenhouse phase of TRAPPIST-1e (few 100 Myr) means that most of this water is retained, alongside sizeable carbon inventories. A silicate weathering thermostat and temperate, habitable conditions are not precluded on TRAPPIST-1e for initial H inventories equal to or exceeding BSE.

In contrast, because TRAPPIST-1b resides interior to the runaway greenhouse limit throughout its evolution, virtually all the surface water produced by the reduction of FeO with H<sub>2</sub> is lost to space, sometimes leaving behind a thin O<sub>2</sub>-dominated atmosphere. The top subplots of Fig. 5 which show final, total surface volatile pressure (bar) are overplotted with a plausible estimate of the maximum atmospheric loss to non-thermal processes<sup>46,47</sup>, which are not explicitly considered here. For TRAPPIST-1b, final surface pressure is comparable to or below this threshold for a wide range of initial H inventories, thereby providing a natural explanation for the apparent airlessness (or thin atmospheres) of TRAPPIST-1b and c suggested by thermal emission observations with JWST<sup>53,54</sup>. This theoretical prediction of surface H, C, and O depletion is qualitatively consistent with Kite and Barnett<sup>23</sup>. In contrast, a substantial atmosphere is predicted for TRAPPIST-1e regardless of initial H inventory.

The non-monotonic behavior of final pressure vs. initial hydrogen can be understood intuitively. At least some hydrogen is needed for the XUV-driven drag of heavier species, otherwise C and O-bearing species cannot escape thermally. Increasing initial H on highly irradiated planets first decreases final C and O as these species are dragged along in the hydrodynamic wind<sup>23</sup>. However, adding more H<sub>2</sub> also liberates more O via FeO reduction as described above, and so at very high initial H<sub>2</sub> inventories not all O is typically lost. Moreover, the high mixing ratios of O<sub>2</sub> and H<sub>2</sub>O mean that most of the absorbed XUV radiation drives H loss and the drag of O, whereas C is somewhat shielded from complete thermal escape by its low mixing ratio.

## Discussion

The calculations described above make clear predictions for the atmospheric retention and habitability prospects for terrestrial planets around low mass stars. TRAPPIST-1e is used as an illustrative example since, in many respects, it is a “worst case scenario” for habitability: its M8 host star underwent a protracted pre-main sequence subjecting its planetary system to high bolometric and XUV fluxes for hundreds of millions of years (planets around early M-dwarfs experience less cumulative XUV). Moreover, TRAPPIST-1e is closest to the inner edge of the habitable zone<sup>55</sup> and thus underwent a longer runaway greenhouse during the pre-main sequence compared to f and g. Consequently, the calculations have implications for habitability prospects for Earth-sized planets around M-dwarfs more broadly. Indeed, we include example calculations applying our model to other M-dwarf hosted planetary systems (LP 890-9 and Proxima Centauri) in the supplementary materials and find very similar results. We conclude that habitability is not precluded by formation with, and subsequent loss of, an H-rich primary atmosphere, or by the extreme XUV

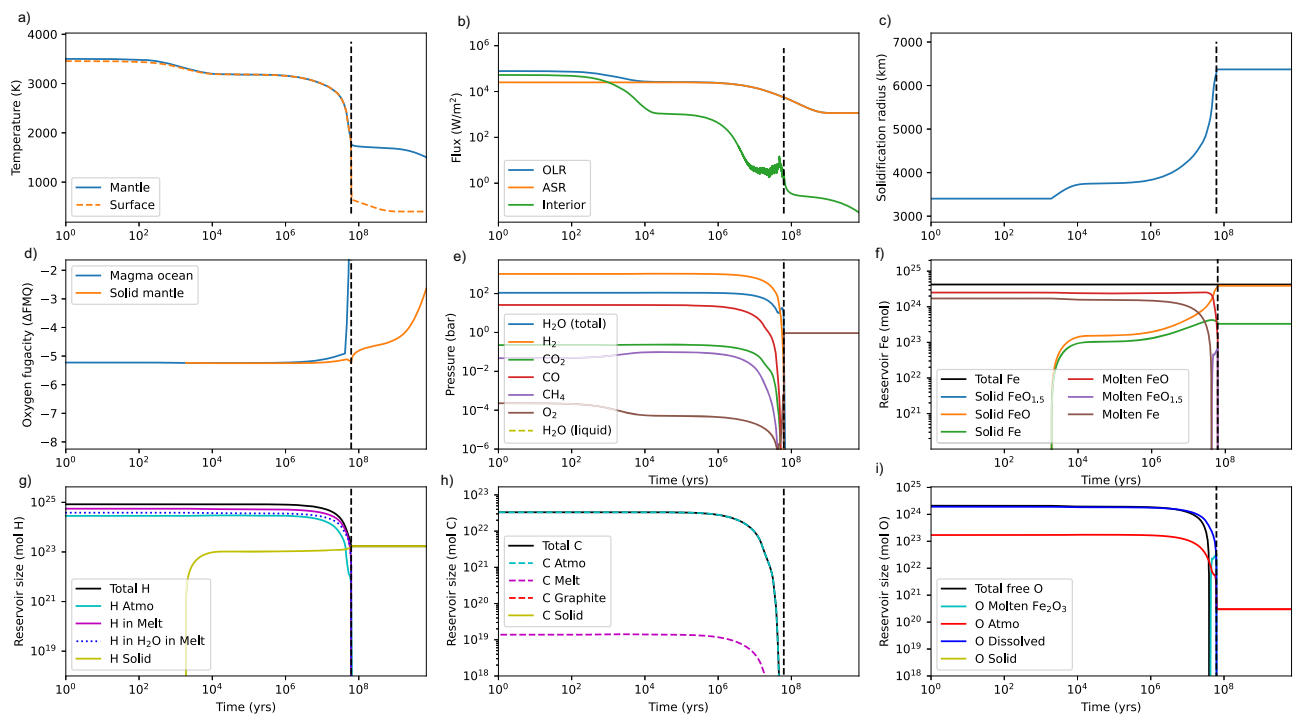


**Fig. 4 | Time-evolution of TRAPPIST-1b, with a large initial H<sub>2</sub> envelope (i.e. the same initial volatile inventories as for TRAPPIST-1e in Fig. 3) from post-accretion magma ocean to present (8 Gyr).** Subplot (a)–(i) are identical to those above. In this case, an H<sub>2</sub>-dominated atmosphere transitions to an H<sub>2</sub>O-dominated atmosphere as H is lost to space and the magma ocean degasses. Unlike for TRAPPIST-1e, virtually all atmospheric H (g) and C (h) are lost to space due to higher experienced XUV fluxes. A small (few bar) O<sub>2</sub> atmosphere is retained that would be

vulnerable to non-thermal escape mechanisms. As in Fig. 3, we make the end-member assumption that all metallic iron generated by the reaction of FeO and H<sub>2</sub> remains in the mantle, and so metallic iron is present in (f). The atmospheric outcomes are qualitatively similar if all metallic iron is assumed to be sequestered in the core (see Fig. S7). Note that we do not explicitly model mantle-atmosphere exchange after magma ocean solidification, only escape and stellar evolution.

environment created by pre-main sequence M-dwarfs. Our results are qualitatively consistent with planetary population synthesis models that similarly predict water-rich temperate, terrestrial planets around M-dwarfs from the reaction of nebular H<sub>2</sub> with silicates<sup>51</sup>. More broadly, these findings suggest temperate planets around M-dwarfs remain compelling targets for atmospheric characterization and astrobiological investigation.

Indeed, these simulations permit a stronger conclusion than that of Krissansen-Totton<sup>56</sup>, which found that the airlessness of TRAPPIST-1b and c does not imply e and f are airless. Here, the calculations in Fig. 5 support the affirmative statement that TRAPPIST-1e is likely to have retained an atmosphere despite vigorous hydrodynamic escape of volatiles in the high XUV environment of the TRAPPIST-1 star. By extension, f and g are even less likely to be airless for the same reason (see Supplementary Fig. S18), although for cooler planets nightside condensation of volatiles must also be considered<sup>57,58</sup>. This conclusion holds for a broad range of initial H inventories all the way from Earth-like, up to maximum initial H-envelope consistent with lack of H<sub>2</sub>-rich atmosphere today (Fig. 5).

With that said, the simulations described above have several caveats that we will now consider. First, if cumulative non-thermal escape fluxes are much larger than most current estimates, then TRAPPIST-1e—and other temperate planets around late M-dwarfs—may be airless regardless of initial volatile endowment. In Fig. 5 the assumed shaded upper limit(s) to non-thermal escape is based loosely on estimates in Dong, et al.<sup>46</sup>, who find ion escape rate of 0.3–2 bar/Gyr for TRAPPIST-1b and 0.1–0.2 bar/Gyr for TRAPPIST-1e assuming CO<sub>2</sub>-dominated atmosphere, as well as Garcia-Sage, et al.<sup>47</sup>, who report an upper limit to ion escape rates from Proxima Centauri b of approximately 6 bar/Gyr assuming the highest possible thermospheric temperature and completely open magnetic field lines. However, for H-O

atmospheres Dong, et al.<sup>48</sup> estimated ion escape rates around TRAPPIST-1g of up to 20 bar/Gyr, ostensibly due to the lack of radiative cooling from CO<sub>2</sub>. Substantial impact erosion rates have also been suggested for TRAPPIST-1<sup>59</sup>, although these are seemingly improbable because the fragile resonance of the TRAPPIST-1 system puts upper limits on the mass flux since the formation of the resonant chain<sup>60</sup>. In any case, given the results described above, if the outer planets of the TRAPPIST-1 system are shown to be airless, then this would suggest either non-thermal loss rates higher than expected in C-bearing atmospheres (e.g. Ref. 48) or initial volatile inventories substantially smaller than that of the Earth<sup>42,61</sup>. While thermal escape rates far larger than our parametrization permits have been suggested<sup>62</sup>, these results must be reconciled with atmospheric retention in the early solar system, and also disagree with escape models that incorporate detailed atomic line cooling, which instead predict secondary atmospheres that are robust to thermal escape under high XUV fluxes<sup>63</sup>.

We similarly emphasize that post magma ocean evolution is not fully modeled in this study; after magma ocean solidification we consider only continued stellar evolution and thermal escape, to enable fair comparison of final outcomes of model runs with different duration magma oceans. In reality, volatile cycling between the mantle and interior via degassing and weathering may occur<sup>42,56</sup>. Importantly, scenarios where substantial H<sub>2</sub>O and C inventories are retained after 8 Gyr evolution do not necessarily guarantee habitability due to the omission of atmosphere-interior exchange processes. One potential impediment to habitability could be the formation of dense, high-pressure ices at the base of ocean that impede carbon cycling and nutrient exchange with the rocky interior<sup>64</sup>. For the largest initial H<sub>2</sub> inventories we consider, the partial pressure of water at the surface of TRAPPIST-1e at the end of our calculations is 2–9 kbar (Fig. 5). Given the final surface temperature distribution for TRAPPIST-1e (Fig. S8)

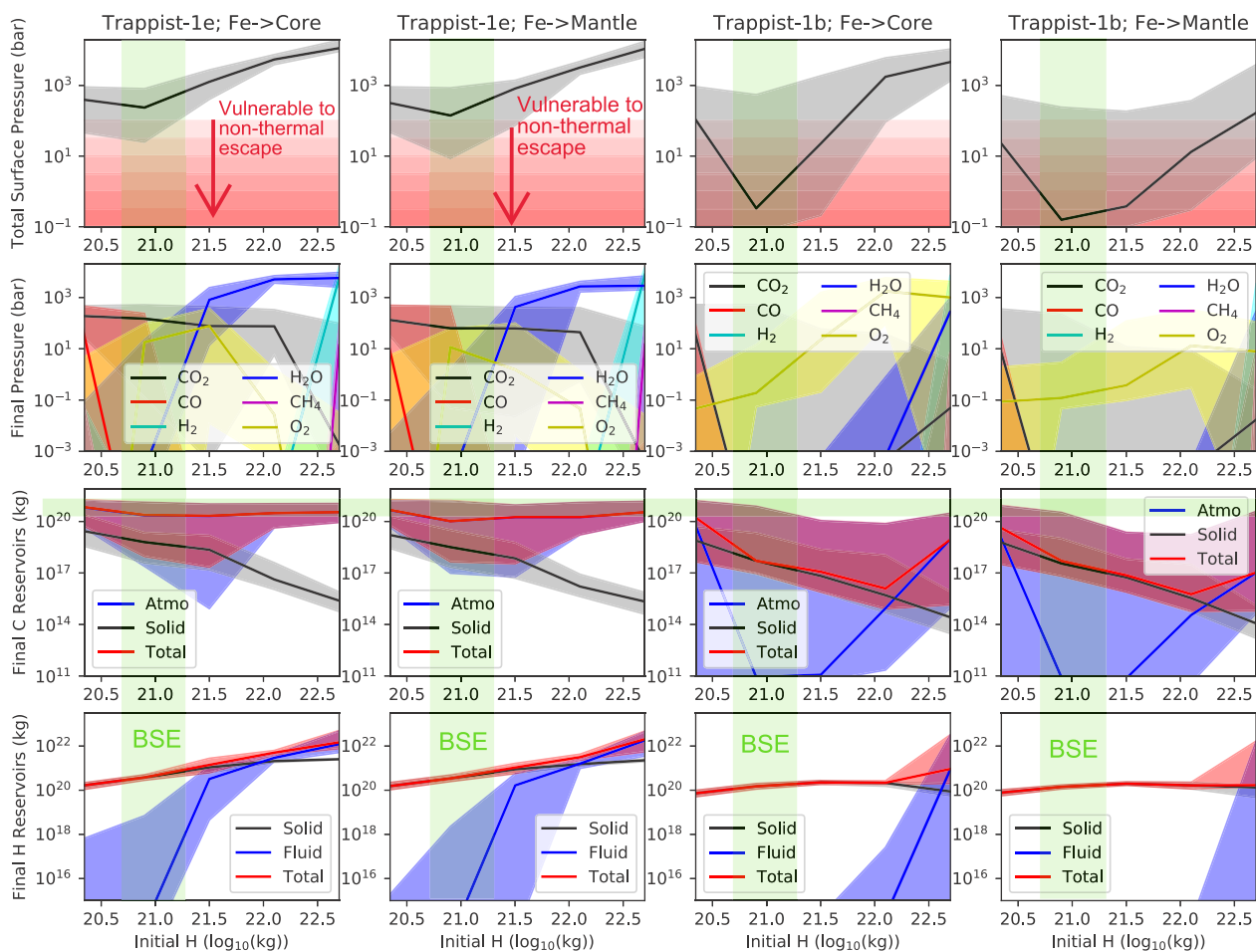


**Fig. 5 | Monte Carlo evolutionary calculation showing outcomes for TRAPPIST 1e (left two columns) and TRAPPIST-1b (right two columns) after 8 Gyr of coupled atmosphere-interior-redox evolution, as a function of initial H endowment.** Rows denote total surface pressure (bar), partial pressures of surface volatiles (bar), final atmosphere and interior carbon inventories (kg C), and final atmosphere and interior hydrogen inventories (kg H), respectively. The two columns for each planet denote endmember cases whereby all metallic iron is sequestered in the core (left), and all metallic iron remains in the silicate mantle (right). Solid lines and shaded regions denote median model outputs and 1-sigma

confidence intervals, respectively. The green-shaded ranges denote approximate modern Bulk Silicate Earth (BSE) volatile abundances, and the red gradients show total surface volatile inventories increasingly vulnerable to non-thermal escape—final volatile inventories in the red-shaded region represent model runs that could result in airless planets. Broadly speaking, TRAPPIST-1e is expected to retain substantial volatiles and habitability is not precluded, whereas TRAPPIST-1b is likely to be left with a comparatively thin  $O_2$  atmosphere susceptible to complete erosion via non-thermal loss.

high-pressure ices are not predicted to form at the base of this ocean<sup>65</sup>. Of course, if TRAPPIST-1e accreted large amounts of water ice<sup>66</sup> then larger surface water inventories are possible. But the accretion of nebular gas and subsequent loss of the primary atmosphere does not, on its own, yield too much water to preclude habitability. More broadly, our results indicate that sufficient surface and interior volatile reservoirs are retained to permit subsequent biogeochemical cycling. A more detailed exploration of atmosphere-interior evolution post magma ocean is a topic for future work, although we note that the possibility of degassing of mantle H, C, and O would only help to replenish surface inventories and buffer against atmospheric escape.

Secondly, our atmosphere-interior-redox evolution model is limited to C, H, O, and Fe-bearing species interacting with a silicate mantle. This simplification omits the influence of other volatiles and redox-sensitive species. For example, the redox sensitivity of Si is neglected; under highly reducing conditions,  $H_2$  may reduce silica to produce additional water and metallic Si via the reaction:  $SiO_2 + 2H_2 \rightarrow 2H_2O + Si_{(metal)}$ . However, the inclusion of metallic Si is unlikely to significantly modify outcomes for the range of initial H inventories considered in this study. Schlichting and Young<sup>67</sup> performed a core-silicate-atmosphere equilibrium calculation for sub-Neptunes and find

that mantle  $SiO_2$  is relatively insensitive to H inventory, and that metallic Si constitutes less than 0.01% of total metallic phases across all H inventories considered. We similarly neglect Si-bearing volatiles and their effect on thermal and redox evolution. While silicate vapor is unlikely to be important for the temperatures considered here<sup>68</sup>, silane ( $SiH_4$ ) is a potentially substantial atmospheric constituent for magma ocean worlds with large H inventories<sup>69</sup>. Specifically, the reaction of  $H_2$  and  $SiO_2$  can generate  $SiH_4 + H_2O$  at surface temperatures in excess of  $\sim 1000$  K<sup>69</sup>. While a full exploration of the effect of Si-bearing volatiles on planetary redox evolution is a subject for future work, we can investigate sensitivity to  $H_2 \rightarrow H_2O$  conversion by repeating calculations for a broad range of initial FeO contents. Supplementary Fig. S10 and S11 repeats our nominal calculations for initial FeO contents varying from 0.02 to 0.2 mantle mole fraction and demonstrates that the conversion of  $H_2$  to water is efficient in all cases; this suggests that the formation of water and silane is unlikely to dramatically change the results presented here; silane will be similarly photo-dissociated and H lost to space as the Si-H bond strength is comparable to the C-H bond strength in  $CH_4$ <sup>70,71</sup>.

Note also that N- and S-bearing species are omitted from the simulations, except for an assumed fixed  $N_2$  background in climate

calculations. Adding additional volatile species would not directly influence retention/escape of C, H, and O-bearing species, but future work ought to explore how N and S inventories are shaped by an extended H-rich atmosphere and pre-main sequence phase, and how the resultant silicate and atmospheric reservoirs might differ from BSE abundances as well as the implications for habitability e.g.<sup>72,73</sup>. Qualitatively, it is reasonable to expect similar outcomes for N as C given their insolubility in silicate melts, comparable cosmochemical abundances, and molecular weights.

The simulations described above do not permit C, H, and O-bearing species to partition into metallic iron. This does not substantially affect the endmember case whereby all metallic iron remains in the silicate mantle because all volatiles that partition into metallic phases remain in the mantle for subsequent degassing. However, if C-H-O partition into metallic phases and the metallic iron is permanently sequestered in the core, then this could diminish prospects for atmospheric retention and habitability. We instead argue that after accretionary core formation is complete (a process which we do not model here) volatile partitioning into metallic phases is minimal for the parameter space we consider. Dissolved carbon mole fractions in reducing silicate melts are typically low, around  $10^{-7}$  in most of our model runs, but here we will suppose they are  $\sim 10^{-5}$  to account for the contribution from neglected dissolved reduced species<sup>74</sup>. In our simulations, the metallic iron to ferrous iron mole fractions in the molten mantle are usually low, except for the highest initial H inventories, where they exceed 1. Thus, supposing a metal partition coefficient for carbon of  $D_C = 100$ <sup>75,76</sup>, then the amount of carbon that partitions into metallic phases in equilibrium is  $10^{-5} \times 100 \times$  (moles metallic Fe). For an Earth-like mantle FeO endowment (0.06 mole fraction), and half of that FeO reduced to metallic Fe by the nebular atmosphere, we have  $10^{-5} \times 100 \times (0.03 \times 6.7 \times 10^{25} \text{ mol mantle}) = 2 \times 10^{21} \text{ mol C}$  sequestered in metallic phases after core formation. This is a small fraction of the atmospheric inventory, which is around  $10^{22}$ – $10^{23} \text{ mol C}$  (Fig. 5). The high abundances of carbon-bearing species detected in warm sub-Neptune atmospheres such as TOI 270d<sup>77,78</sup> also argues against C being mostly lost to metallic phases, even under strongly reducing conditions. For hydrogen, Schlichting and Young<sup>67</sup> report only 1–10% of total planetary hydrogen partitions into the metallic core for temperatures ranging from 3000 to 5000 K, a deficit that's unlikely to affect the broad conclusions of this paper. Other work has similarly concluded a low core H content for Earth<sup>79</sup>. Of course, a more complete exploration of this topic would require an explicit exploration of volatile partitioning during N-body growth and core formation (e.g. Refs. 80, 81) with co-evolving climate and atmospheric escape; this ambitious undertaking is left for future work.

To conclude, for habitable zone planets, the transition from sub-Neptune to terrestrial planet via XUV-driven escape of a primary atmosphere typically does not strip the planet of high molecular weight volatiles, and instead is likely to leave behind large surface water inventories. This improves the habitability prospects for terrestrial planets around late M-dwarfs that accrete primary atmospheres. Consistent with previous calculations, the transition from sub-Neptune to terrestrial planets for highly irradiated, Venus-analogs is likely to strip high mean molecular weight volatiles and leave behind thin atmospheres (and small mantle volatile inventories) that are susceptible to erosion via non-thermal escape processes. The two conclusions above provide a natural explanation for the apparent airlessness or thin  $\text{O}_2$ - $\text{CO}_2$  atmospheres of TRAPPIST-1b and c favored by JWST observations. In contrast, the same model predicts that TRAPPIST-1e, f, and g are unlikely to be airless rocks given plausible initial inventories and thermal escape histories. If all the planets in the TRAPPIST-1 system are airless despite the predictions above, then this would strongly suggest either unexpectedly large non-thermal escape fluxes or initial volatile endowments much smaller than that of the Earth.

## Methods

### Radiative-convective climate model

The open-source radiative transfer code petitRADTRANS<sup>82</sup> was used to compute surface temperature as a function of atmospheric composition. Specifically, we precomputed outgoing longwave radiation (OLR) fluxes as a function of surface temperature, stratospheric temperature,  $\text{CO}_2$ , CO,  $\text{H}_2$ , and  $\text{H}_2\text{O}$  inventories. In addition to line lists for  $\text{H}_2\text{O}$ ,  $\text{CO}_2$ , and CO<sup>83</sup>, we include continuum opacities for  $\text{H}_2\text{O}$ - $\text{H}_2\text{O}$ ,  $\text{CO}_2$ - $\text{CO}_2$ ,  $\text{H}_2$ - $\text{H}_2$ , and CO-CO collisionally induced absorption<sup>82</sup>. Sensitivity tests show that  $\text{H}_2$ -He and  $\text{H}_2\text{O}$ - $\text{CO}_2$  CIA can be neglected for the atmospheres we consider, i.e. their additions to opacity are small compared to other sources of error. Given the lack of CO-CO CIA data, we use  $\text{N}_2$ - $\text{N}_2$  CIA as an analog based on isoelectronicity and identical molecular weights. Following previous magma ocean studies<sup>28,32,84</sup>, a dry adiabat, to moist adiabat, to isothermal temperature structure was assumed; the temperature profile transitions from dry adiabat to moist adiabat when the partial pressure of water vapor drops below saturation, and the atmosphere transitions to isothermal when the temperature reaches the planetary skin temperature. Note that water is the only condensable species for the temperature ranges relevant to this study. For surface temperatures below the critical point of water (647 K) water partitions into atmospheric and condensed surface reservoirs as specified by saturated vapor pressure. At each timestep in the evolutionary model, we solve for the surface temperature that balance OLR—which itself depends on surface volatile inventories and atmospheric temperature profile—, heating from the interior,  $q_m$  (described below) and absorbed shortwave radiation (ASR):

$$OLR(T_{surf}, \zeta_{\text{H}_2\text{O}}, \zeta_{\text{H}_2}, \zeta_{\text{CO}_2}, \zeta_{\text{CO}}, T_e) = q_m(T_{surf}, T_p, r_s) + ASR(t) \quad (1)$$

Here, ASR evolves with bolometric luminosity (see below), modulated by planet-star separation and assumed albedo. Albedo is a fixed parameter that is sampled broadly in our Monte Carlo analysis. Attempting to model the complex cloud microphysics, aerosol properties, atmospheric circulation patterns, and climate system feedbacks that control planetary albedo across the primary-to-secondary atmospheric transition would be a challenging undertaking that would require a hierarchy of computational models including 3D GCMs. Instead, we take a conservative approach with respect to the duration of magma ocean solidification and assume a low albedo range (0–0.2). This range is consistent with what is expected for cloud-free runaway greenhouse atmospheres on planets around late M-dwarfs<sup>85,86</sup>, but also maximizes the duration of the runaway greenhouse compared to cloudy scenarios, and by extension the longevity of hydrodynamic escape. We later consider sensitivity tests with higher albedo values and find conclusions unchanged (see Supplementary Materials). The radiative effects of methane are neglected since methane abundances are only significant in  $\text{H}_2$ -dominated atmospheres, for which the greenhouse warming of  $\text{H}_2$  typically dominates. We assume a fixed 1 bar background of  $\text{N}_2$ , which is expected to have a minimal impact on climate evolution for typical (10–1000 s of bar) surface inventories of C-, H-, and O-bearing species. Note that there are sometimes rapid variations in interior heatflow (e.g. Figure 2 around  $\sim 10^7$  years) that are numerical artefacts attributable to an imperfect climate grid. By assuming an adiabat in the deep atmosphere, we neglect the possibility of a transition to a deep radiative zone<sup>87</sup>. This possibility is instead explored in supplementary materials and is found unlikely to affect qualitative conclusions. Additionally, more rapid magma ocean solidification would trap more volatiles in the mantle where they are shielded from early XUV fluxes and are available for later degassing – our climate model is therefore conservative on atmospheric loss. Finally, we conducted sensitivity tests with an independent, alternative climate model, *Clima*<sup>40</sup>, and found qualitatively similar conclusions.

### Magma ocean thermal evolution

All models are initialized with a completely molten mantle, and the subsequent thermal evolution of the magma ocean is governed by energy balance:

$$\rho_m c_p V_m \frac{dT_p}{dt} = \rho_m V_m Q_r + Q_c + \rho_m 4\pi r_s^2 \Delta H_f \frac{dr_s}{dt} - q_m 4\pi r_p^2 \quad (2)$$

Here,  $V_m = 4\pi(r_p^3 - r_s^3)/3$  is the volume of the molten mantle,  $\rho_m$  is the average density of the mantle,  $Q_r$  is radionuclide heat production per unit mass,  $r_p$  is planetary radius,  $\Delta H_f$  is the latent heat of fusion of silicates,  $r_s$  is the solidification radius,  $c_p$  is the specific heat of silicates,  $Q_c$  is the heatflow from the metallic core<sup>28</sup>,  $T_p$  is mantle potential temperature, and  $dr_s/dt$  is the time-evolution of the solidification radius. The heatflow from the interior to the atmosphere,  $q_m$ , is calculated using a 1-D convective parameterization, with temperature-dependent magma ocean viscosity,  $\nu(T_p)$ :

$$q_m = \frac{k(T_p - T_{surf})}{(r_p - r_s)} \left( \frac{Ra}{Ra_{cr}} \right)^\beta \quad (3)$$

Where  $T_{surf}$  is surface temperature, and  $k$  is thermal conductivity. The Rayleigh number,  $Ra$ , is given by

$$Ra = \frac{\alpha g (T_p - T_{surf}) (r_p - r_s)^3}{\kappa \nu (T_p)} \quad (4)$$

Here,  $\kappa$  is thermal diffusivity,  $Ra_{cr}$  is the critical Rayleigh number,  $g$  is surface gravity, and  $\alpha$  is thermal expansivity. These equations continue to govern the thermal evolution of the mantle after the magma ocean has solidified, except with  $dr_s/dt = 0$  (see below). The temperature-dependent mantle viscosity parameterization is identical to that of Krissansen-Totton, et al.<sup>28</sup> and smoothly transitions from low viscosity at high melt fractions to a solid-like “mush” at low melt fractions.

### Magma ocean geochemical evolution

At every timestep in the evolutionary model, we simultaneously solve a coupled system of equations describing the partitioning of C, H, O-bearing volatiles between atmosphere, molten silicate mantle (and metallic) phases, melt oxygen fugacity, iron speciation, and surface temperature. This system of equations is iteratively solved simultaneously with the radiative-convective climate model to self-consistently determine redox, climate, and volatile speciation at each time-step. Gas speciation is determined by the following equations:

$$\ln \left( \frac{K_1}{fO_2^{0.5}} \right) + \ln(fH_2O) = \ln(fH_2) \quad (5)$$

$$\ln \left( \frac{K_2}{fO_2^{0.5}} \right) + \ln(fCO_2) = \ln(fCO) \quad (6)$$

$$\ln \left( \frac{K_3}{fO_2^2} \right) + \ln(fCO_2) + 2 \ln(fH_2O) = \ln(fCH_4) \quad (7)$$

Here,  $K_1$ ,  $K_2$ , and  $K_3$  are temperature-dependent equilibrium constants<sup>88</sup>, and  $fX$  represents the fugacity of volatile species  $X$  (bar).

We adopt the following silicate melt solubility laws for  $CO_2$ ,  $H_2O$ <sup>89</sup>, and  $H_2$ <sup>90</sup>:

$$\ln \left( \frac{m_{CO_2} M_{melt}}{M_{CO_2}} \right) = \frac{m_{H_2O} M_{melt}}{M_{H_2O}} d_{H_2O} + a_{CO_2} \ln(fCO_2) + F_1 \quad (8)$$

$$\ln \left( \frac{m_{H_2O} M_{melt}}{M_{H_2O}} \right) = a_{H_2O} \ln(fH_2O) + F_2 \quad (9)$$

$$\log_{10}(m_{H_2} \times 10^6) = 0.524139 \times \log_{10}(fH_2) + 1.100836 \quad (10)$$

Here,  $M_X$  are molar masses of respective species (kg/mol), and  $M_{melt} = 0.06452$  kg/mol is the average molar mass of silicate melts. The terms  $m_X$  represent the mass fraction of dissolved volatile species in the melt phase (kg X/kg melt), and the remaining terms are empirical constants, or weakly pressure-dependent constants in the case of  $F_1$  and  $F_2$ .

We also permit graphite precipitation under C-rich, highly reducing conditions. Specifically, if the dissolved  $CO_2$  mass fraction,  $m_{CO_2}$ , is less than graphite saturation then the melt is undersaturated and all carbon is partitioned between  $CO_2$ ,  $CO$ , and  $CH_4$ . Conversely, if dissolved carbon exceeds graphite saturation then the excess C partitions into solid graphite (total moles  $n_{graphite}$ ) and the remaining dissolved carbonate concentration in the melt equals graphite saturation (see supplementary materials for details).

The speciation equations above are constrained by mass conservation across all phases. Hydrogen atom conservation is given by:

$$n_H = n_{atm} \left( 4 \frac{fCH_4}{P} + 2 \frac{fH_2O}{P} + 2 \frac{fH_2}{P} \right) + 2m_{H_2O} \frac{\Pi_{melt}}{M_{H_2O}} + 2m_{H_2} \frac{\Pi_{melt}}{M_{H_2}} \quad (11)$$

Here,  $n_H$  is the total number of moles of H,  $n_{atm}$  is the total number of moles in the atmosphere,  $P$  is surface pressure, and  $\Pi_{melt} = \rho_m V_m$  is the mass of the magma ocean (kg).

Carbon atom conservation is similarly given by:

$$n_C = n_{atm} \left( \frac{fCH_4}{P} + \frac{fCO_2}{P} + \frac{fCO}{P} \right) + m_{CO_2} \frac{\Pi_{melt}}{M_{CO_2}} + n_{graphite} \quad (12)$$

Here,  $n_C$  is the total moles carbon in the fluid system. Note that we are ignoring  $CO$  and  $CH_4$  dissolution because dissolved carbon dioxide and graphite are expected to dominate. This is a conservative assumption for atmospheric loss since adding further reduced species would potentially shield dissolved carbon from escape.

Finally, we impose oxygen atom conservation. Magma ocean models often neglect oxygen conservation on the grounds that the mantle is an infinite reservoir of oxygen atoms. This assumption is not justified for large surface volatile inventories where the reaction of molecular  $H_2$  with the silicate interior can potentially modify bulk mantle redox; if oxygen conservation is not imposed, then more water can be created than there are oxygen atoms in the mantle. Oxygen conservation is given by the following equation:

$$n_O + n_{O-bound-Fe} = n_{atm} \left( 2 \frac{fH_2O}{P} + 2 \frac{fCO_2}{P} + \frac{fCO}{P} + 2 \frac{fO_2}{P} \right) + 2m_{CO_2} \frac{\Pi_{melt}}{M_{CO_2}} + m_{H_2O} \frac{\Pi_{melt}}{M_{H_2O}} \quad (13)$$

Here,  $n_O$  is the total number of “free” oxygen atoms, that is, those not bound up as  $FeO$ ,  $SiO_2$ ,  $Al_2O_3$  etc. which we do not explicitly consider. Free oxygen is partitioned between  $FeO_{1.5}$  and atmospheric + dissolved volatile species. It is necessary to include a correction  $n_{O-bound-Fe}$  for free oxygen bound up in ferric iron (0.5 mol per  $FeO_{1.5}$ )

and for instances where additional free oxygen is liberated by the reduction of ferrous iron to metallic iron i.e.  $\text{FeO} + \text{H}_2 = \text{H}_2\text{O} + \text{Fe}$  (we return to the formalism for this below). Since the model conserves H, O, C, and Fe atoms, redox is conserved by construction.

Finally, total surface pressure and the total number of moles in the atmosphere are related as follows:

$$P = \frac{n_{\text{atm}}g}{4\pi r_p^2 \times 10^5} \left( M_{\text{CH}_4} \frac{f_{\text{CH}_4}}{P} + M_{\text{CO}_2} \frac{f_{\text{CO}_2}}{P} + M_{\text{CO}} \frac{f_{\text{CO}}}{P} + M_{\text{H}_2} \frac{f_{\text{H}_2}}{P} + M_{\text{H}_2\text{O}} \frac{f_{\text{H}_2\text{O}}}{P} + M_{\text{O}_2} \frac{f_{\text{O}_2}}{P} \right) \quad (14)$$

Where the factor of  $10^5$  is necessary to convert between fugacities (bar) and SI units of pressure (Pa). If oxygen fugacity is treated as a free variable, then our gases plus dissolved species code closely reproduces that in Gaillard, et al.<sup>33</sup>

Since mantle redox is co-evolving with the atmosphere, we need to relate oxygen fugacity to iron speciation in the melt. For oxidized regimes this is governed by the empirical relationship between ferrous and ferric iron in Kress and Carmichael<sup>91</sup>:

$$\ln\left(\frac{X_{\text{FeO}_{1.5}}}{X_{\text{FeO}}}\right) = 0.196 \times \ln(f_{\text{O}_2}) + c(T, P, X_i) \quad (15)$$

Here,  $X_{\text{FeO}_{1.5}}$  and  $X_{\text{FeO}}$  are the molar fractions of ferric and ferrous iron in the melt, respectively, and  $c(T, P, X_i)$  represents a series of T-dependent, P-dependent, and melt-composition dependent coefficients (see Supplementary Materials); metallic phases are assumed to be negligible under oxidizing conditions.

In contrast, for low oxygen fugacities, ferric iron is negligible and oxygen fugacity is governed by the relationship between metallic iron and ferrous iron in the melt:

$$2 \times \log_{10}\left(\frac{1.5X_{\text{FeO}}}{0.8X_{\text{Fe}}}\right) = \log_{10}(f_{\text{O}_2}) - \log_{10}(f_{\text{O}_2}(\text{IW})) \quad (16)$$

Here, the oxygen fugacity at the iron wustite (IW) buffer is calculated from surface temperature and pressure using Frost<sup>92</sup>. The mole fraction of iron in the metallic phase,  $X_{\text{Fe}}$  equals 1, and activity coefficients representative of typical surface conditions have been chosen for iron oxide, 1.5, and metallic iron, 0.8<sup>93,94</sup>. For greater numerical efficiency, we imposed a smooth transition in oxygen fugacity between equation (i) and (ii) at intermediate redox states, as described in the supplementary materials. In all cases, we enforce conservation of iron in the melt (although in some instances we permit total iron to evolve with time if iron is sequestered into the metallic core, as described below):

$$X_{\text{FeO}} + X_{\text{FeO}_{1.5}} = X_{\text{FeO}_{\text{Tot}}} \quad (17)$$

$$X_{\text{FeO}_{\text{Tot}}}|_{t=0} = X_{\text{FeO}_{\text{Tot}}} + \frac{m_{\text{Fe}}M_{\text{melt}}}{M_{\text{Fe}}} \quad (18)$$

Taken as a whole, given total silicate melt mass ( $\Pi_{\text{melt}}$ ), the number of hydrogen ( $n_{\text{H}}$ ), carbon ( $n_{\text{C}}$ ), oxygen atoms ( $n_{\text{O}}$ ), and the iron content of melt, our model simultaneously solves for surface volatile speciation at a given surface temperature. The model then iteratively calculates OLR, ASR, and heat flux from the interior,  $q_m$ , to solve for radiative-convective equilibrium and geochemical equilibrium every timestep (using the previous timestep as a guess for computational efficiency). Consistent with other magma ocean models, we assume the dissolved volatile concentration of the melt at the surface is equal to the dissolved volatile content at depth given increasing volatile solubility with pressure and the comparatively low viscosity of the magma ocean favoring rapid chemical equilibration (although see Salvador and Samuel<sup>95</sup> for possible limitations to this assumption).

Similarly, while we recognize that iron speciation and mantle redox is pressure sensitive<sup>96–98</sup>, we only compute iron speciation and oxygen fugacity at the surface of the magma ocean since only the surface melt interacts directly with the atmosphere.

### Stellar evolution and atmospheric escape

Standard parameterizations of bolometric luminosity<sup>99</sup> and XUV luminosity evolution are adopted for the sun<sup>100</sup> and TRAPPIST-1<sup>101</sup>. Atmospheric escape is either diffusion limited or XUV limited, depending on the stellar XUV flux and the composition of the upper atmosphere, which is defined here as everything above the tropopause. To simplify escape calculations,  $\text{H}_2\text{O}$ ,  $\text{CO}_2$ ,  $\text{CH}_4$ ,  $\text{H}_2$  are assumed to photodissociate such that the only upper atmosphere species are atomic H, atomic O, and  $\text{CO}$ <sup>102</sup>. If the upper atmosphere is H-poor, then escape will be diffusion-limited as H escapes via diffusion through an O and CO background; neither O nor CO can escape in the diffusion-limited regime. In contrast, in the XUV-limited regime, the hydrodynamic outflow of H may drag along O (and even CO) following previous parameterizations<sup>103–105</sup>. Thermosphere temperature and the cold-trap temperature modulate the drag of heavier species and the amount of H-bearing gases that reach the upper atmosphere, respectively. The escape model also incorporates broad parameterizations of XUV-driven escape efficiency, and a smooth transition from the diffusion-limited to XUV-limited regime. Our escape scheme is described in Supplementary Materials and is similar to that of Krissansen-Totton, et al.<sup>28</sup>, except that we assume that carbon escapes as CO rather than  $\text{CO}_2$  (a conservative assumption that makes the loss of C easier), and a correction is made for  $\text{CH}_4$  in reducing atmospheres.

### Time evolution

Volatile reservoirs co-evolve with the solidification of the magma ocean as governed by the following system of equations. We distinguish between the solid reservoirs (silicate mantle below solidus), and fluid reservoirs (atmosphere + volatiles dissolved in the magma ocean).

The time evolution of solid,  $\Pi_{\text{H-solid}}$  (kg), and fluid,  $\Pi_{\text{H-fluid}}$  (kg), hydrogen reservoirs is governed by the following equations:

$$\frac{d\Pi_{\text{H-solid}}}{dt} = 4\pi\rho_m r_s^2 \frac{dr_s}{dt} \left[ \left( m_{\text{H}_2\text{O}} \frac{M_{\text{H}_2}}{M_{\text{H}_2\text{O}}} \right) ((1-f_{\text{TL}})k_{\text{H}_2\text{O}} + f_{\text{TL}}) + m_{\text{H}_2} f_{\text{TL}} \right] \quad (19)$$

$$\frac{d\Pi_{\text{H-fluid}}}{dt} = -\frac{d\Pi_{\text{H-solid}}}{dt} + \phi_{\text{H}} \quad (20)$$

Here,  $f_{\text{TL}}$  is the melt fraction trapped in the mantle as the solidification front moves towards the surface<sup>42,106</sup>, which in turn depends on the rate of change in mantle temperature,  $k_{\text{H}_2\text{O}} = 0.01$  is the partition coefficient for water between fluid and crystalline phases, and  $\phi_{\text{H}}$  is the escape flux of H. In the supplementary materials we investigate the sensitivity of our results to melt trapping assumptions and find it has a negligible effect.

For free oxygen, the time-evolution equations governing solid,  $\Pi_{\text{O-solid}}$  (kg), and fluid,  $\Pi_{\text{O-fluid}}$  (kg), reservoirs are:

$$\frac{d\Pi_{\text{O-solid}}}{dt} = 4\pi\rho_m r_s^2 \frac{dr_s}{dt} \left[ m_{\text{FeO}_{1.5}} \frac{M_{\text{O}}}{M_{\text{FeO}_{1.5}}} + m_{\text{H}_2\text{O}} \frac{M_{\text{O}}}{M_{\text{H}_2\text{O}}} ((1-f_{\text{TL}})k_{\text{H}_2\text{O}} + f_{\text{TL}}) + m_{\text{CO}_2} \frac{M_{\text{O}}}{M_{\text{CO}_2}} ((1-f_{\text{TL}})k_{\text{CO}_2} + f_{\text{TL}}) \right] - \chi_{\text{metal}} \quad (21)$$

**Table 1 | free parameters in our model, the nominal parameter value for illustrative calculations (Figs. 2–4), and the full Monte Carlo range shown in later calculations (Fig. 5)**

Parameter name	Variable	Nominal point estimate	Monte Carlo range	Explanation/Reference
Initial conditions	Initial carbon, C (kg)	$4 \times 10^{20}$	$10^{20}$ – $10^{21.5}$	Approximate bulk silicate Earth carbon inventory <sup>11–13</sup>
	Initial free oxygen, O (kg)	$6 \times 10^{21}$	$10^{21}$ – $10^{22}$	Approximately Earth-like (ensures post-solidification mantle redox around quartz-fayalite-magnetite buffer if no nebular atmosphere).
Initial hydrogen, H (kg)	Initial hydrogen, H (kg)	$4 \times 10^{20}$	$10^{20}$ – $10^{23}$	Point estimate is approximate bulk silicate Earth inventory, range encompasses large primary atmosphere.
	Initial radionuclide U, Th, and K inventory (relative Earth)	1.0	0.33–30.0	Scalar multiplication of Earth's radionuclide inventories in Lebrun, et al. <sup>27</sup> . Allows for modest tidal heating.
	Initial mantle FeO (mole fraction)	0.06	0.06	Earth-like value assumed for nominal calculations, but supplementary material investigates broad range of FeO (0.02–0.2)
Stellar evolution and escape parameters	TRAPPIST-1 XUV saturation time, $t_{\text{sat}}$	3.14	$3.14^{+2.22}_{-1.46}$ Gyr	XUV evolution parameters drawn randomly from joint distribution <sup>10</sup> .
	Post saturation phase XUV decay exponent, $\beta_{\text{decay}}$	-1.17	$-1.17^{+0.27}_{-0.28}$	XUV evolution parameters drawn randomly from joint distribution <sup>10</sup> .
Escape efficiency at low XUV flux, $\epsilon_{\text{low}}$	Saturated $\log_{10}(F_{\text{XUV}}/F_{\text{BOLOMETRIC}})$ flux ratio	-3.03	$-3.03^{+0.25}_{-0.23}$	XUV evolution parameters drawn randomly from joint distribution <sup>10</sup> .
	Escape efficiency at low XUV flux, $\epsilon_{\text{low}}$	0.2	0.01–0.3	See escape section in Krissansen-Totton, et al. <sup>28</sup> .
Transition parameter for diffusion limited to XUV-limited escape, $\lambda_{\text{tra}}$	Transition parameter for diffusion limited to XUV-limited escape, $\lambda_{\text{tra}}$	1.0	$10^{-6}$ – $10^*$	See escape section in Krissansen-Totton, et al. <sup>28</sup> .
	XUV energy that contributes to XUV escape above hydrodynamic threshold, $\zeta_{\text{high}}$	50%	0–100%	See escape section in Krissansen-Totton, et al. <sup>28</sup> .
Cold trap temperature variation, $\Delta T_{\text{cold-trap}}$	Cold trap temperature variation, $\Delta T_{\text{cold-trap}}$	0 K	-30 to +30 K	Cold trap temperature, $T_{\text{cold-trap}}$ , equals planetary skin temperature plus a fixed, uniformly sampled variation, $T_{\text{cold-trap}} = T_{\text{eq}}(1/2)^{0.25} + \Delta T_{\text{cold-trap}}$ . Here, $T_{\text{eq}}$ is the planetary equilibrium temperature given assumed albedo.
	Thermosphere temperature, $T_{\text{thermo}}$	1000 K	200–5000 K*	114–116
Interior parameter	Mantle viscosity coefficient	10 Pa	$10^{-10^3}$ Pa s*	Solid mantle kinematic viscosity, $\nu_{\text{rock}}$ , ( $\text{m}^2/\text{s}$ ) is given by the following equation: $\nu_{\text{rock}} = V_{\text{core}} 3.8 \times 10^7 \exp(\frac{35000}{334T_p}) / \rho_m$ . Here $T_p$ is mantle potential temperature (K) and $\rho_m$ is mantle density ( $\text{kg}/\text{m}^3$ ). See Krissansen-Totton, et al. <sup>28</sup> .
	Bond albedo during magma ocean solidification	0.2	0.0–0.2	85,86

\*Denotes this variable was sampled uniformly in log space. All others (except stellar XUV parameters) sampled uniformly in linear space.

$$\frac{d\Pi_{O\text{-fluid}}}{dt} = -4\pi\rho_m r_s^2 \frac{dr_s}{dt} \left[ m_{FeO_{1.5}} \frac{M_O}{M_{FeO_{1.5}}} + m_{H_2O} \frac{M_O}{M_{H_2O}} ((1-f_{TL})k_{H_2O} + f_{TL}) \right. \\ \left. + m_{CO_2} \frac{M_O}{M_{CO_2}} ((1-f_{TL})k_{CO_2} + f_{TL}) \right] - \phi_O + \psi_{metal} \quad (22)$$

Here,  $k_{CO_2}$  is the partition coefficient for  $CO_2$  between fluid and crystalline phases, and  $\phi_O$  is the escape flux of O. The metal corrections,  $\psi_{metal}$  and  $\chi_{metal}$  are described below.

The time-evolution equations governing carbon reservoirs are as follows:

$$\frac{d\Pi_{C\text{-solid}}}{dt} = 4\pi\rho_m r_s^2 \frac{dr_s}{dt} \left( m_{CO_2} \frac{M_C}{M_{CO_2}} \right) ((1-f_{TL})k_{CO_2} + f_{TL}) \quad (23)$$

$$\frac{d\Pi_{C\text{-fluid}}}{dt} = -\frac{d\Pi_{C\text{-solid}}}{dt} - \phi_C \quad (24)$$

Where C reservoirs and escape flux are similarly denoted. Note that we neglect transfer of graphite to the solid interior due to its buoyancy in silicate melts.

Finally, we include three additional equations to track the evolution of solid ferrous ( $\Pi_{FeO\text{-solid}}$ ), ferric ( $\Pi_{FeO_{1.5}\text{-solid}}$ ), and metallic iron ( $\Pi_{Fe\text{-solid}}$ ) in the solid mantle interior:

$$\frac{d\Pi_{FeO_{1.5}\text{-solid}}}{dt} = 4\pi\rho_m r_s^2 \frac{dr_s}{dt} m_{FeO_{1.5}} \quad (25)$$

$$\frac{d\Pi_{FeO\text{-solid}}}{dt} = 4\pi\rho_m r_s^2 \frac{dr_s}{dt} m_{FeO} \quad (26)$$

$$\frac{d\Pi_{Fe\text{-solid}}}{dt} = 4\pi\rho_m r_s^2 \frac{dr_s}{dt} m_{Fe} \quad (27)$$

We are assuming surface speciation of iron governs the partitioning of iron into solid phases, which is an oversimplification of redox stratification. However, since we are most interested in speciation at the surface, and because the mantle is assumed not to interact with the atmosphere post-solidification (see below), this simplification is appropriate.

The time evolution of the solidification radius,  $r_s$ , is governed by the movement of the solidus-mantle adiabat intercept as the mantle cools, and is calculated analytically<sup>28</sup>.

### Treatment of metallic iron

The system of equations described above are agnostic on the fate of metallic iron that forms in the melt. Rather than attempt to solve the complex coupled geodynamical + geochemical problem of core formation, we instead consider two endmember scenarios for metallic iron:

(1) All metallic iron remains entrained in the silicate melt, until partitioned into the solid silicate mantle via Eq. (27). This endmember is plausible given the persistence of metallic iron in Mercury's reducing crust<sup>107</sup> as well as plausible proposed mechanisms for iron droplet entrainment or buoyancy<sup>108,109</sup>. In this scenario, the metal correction terms are given by:

$$\chi_{metal} = \psi_{metal} = 4\pi\rho_m r_s^2 \frac{dr_s}{dt} m_{Fe} \frac{M_O}{M_{Fe}} \quad (28)$$

This ensures the transfer of metallic iron to the solid mantle permanently adds free oxygen to fluid phases. Simultaneously, we apply the following correction to fluid phase equilibria for free oxygen

liberated by metallic iron in the melt:

$$n_{O\text{-as-Fe}} = \Pi_{melt} \frac{M_O}{M_{Fe}} (X_{FeO_{Tot}}|_{t=0} - X_{FeO_{Tot}}) \frac{M_{Fe}}{M_{melt}} - \frac{\Pi_{melt} m_{FeO_{1.5}}}{M_O} \left( \frac{0.5M_O}{M_{Fe} + 1.5M_O} \right) \quad (29)$$

Here  $X_{FeO_{Tot}}|_{t=0}$  is a constant, but  $X_{FeO_{Tot}} = X_{FeO} + X_{FeO_{1.5}}$  may evolve with melt redox as iron is partitioned between oxidized and metallic phases.

(2) All metallic iron is instantaneously removed to the metallic core. This is plausible on the grounds that iron droplets have a much higher density than the surrounding silicate melt and are expected to sink on timescales shorter than the typical magma ocean solidification<sup>110</sup>. In this scenario,

$$\chi_{metal} = 0 \quad (30)$$

$$\psi_{metal} = 4\pi\rho_m r_s^2 \frac{dr_s}{dt} m_{Fe} \frac{M_O}{M_{Fe}} (X_{FeO_{Tot}}|_{t=0} - X_{FeO_{Tot}}) \frac{M_{Fe}}{M_{melt}} \quad (31)$$

Here, we assume the solidification of the magma ocean does not add free oxygen-consuming metallic iron to the solid mantle because that metal instantly moves to the core. In contrast, free oxygen is still permanently liberated in the fluid phase when melt with a lower-than-initial FeO content solidifies. In this case, the free oxygen in the fluid phase is similarly corrected using Eq. (29).

### Post magma ocean evolution

Our focus is on the transition from primary to secondary atmosphere evolution, and so we do not attempt to model the full diversity of processes shaping atmospheric evolution after the surface temperature drops below the solidus. However, to allow comparisons between outcomes of different magma ocean duration, we do continue atmospheric evolution after magma ocean solidification permitting atmospheric escape to continue alongside stellar evolution, and continuous re-equilibration of surface volatiles at a plausible quench temperature (1000 K); surface climate evolves self-consistently with atmospheric composition and stellar evolution. No exchange of volatiles between the atmosphere and interior occurs post-magma ocean solidification. This is a conservative assumption for investigating atmospheric preservation since real planets may replenish escaping volatiles by magmatic degassing. The end of the magma ocean is defined as when the surface temperature drops below the solidus; volatiles dissolved in the magma ocean at this time are assumed to remain trapped in the mantle, thereby minimizing the surface volatile inventory susceptible to subsequent escape.

### Monte Carlo approach

To accommodate uncertainty in initial composition, atmospheric escape, atmosphere-interior interaction, and interior evolution processes, we present both nominal "point estimate" calculations, and results from Monte Carlo ensembles that broadly sample uncertain planetary parameters. Table 1 includes the unknown free-parameters in our model, the nominal parameter value for illustrative purposes, and the full Monte Carlo range shown in later calculations.

### Data availability

Full time-evolution outputs from nominal model calculations have been permanently archived on Zenodo: 10.5281/zenodo.13161895

### Code availability

The Python code for the PACMAN-P magma ocean evolutionary model is available on the lead author's Github and has also been permanently archived on Zenodo: 10.5281/zenodo.13206993

## References

- Mousis, O. et al. Irradiated ocean planets bridge super-Earth and sub-Neptune populations. *Astrophys. J. Lett.* **896**, L22 (2020).
- Zeng, L. et al. Growth model interpretation of planet size distribution. *Proc. Natl Acad. Sci.* **116**, 9723–9728 (2019).
- Neil, A. R., Liston, J. & Rogers, L. A. Evaluating the evidence for water world populations using mixture models. *Astrophys. J.* **933**, 63 (2022).
- Venturini, J., Guilera, O. M., Haldemann, J., Ronco, M. P. & Morasini, C. The nature of the radius valley—Hints from formation and evolution models. *Astronomy Astrophys.* **643**, L1 (2020).
- Izidoro, A. et al. The exoplanet radius valley from gas-driven planet migration and breaking of resonant chains. *Astrophys. J. Lett.* **939**, L19 (2022).
- Bean, J. L., Raymond, S. N. & Owen, J. E. The nature and origins of sub-Neptune size planets. *J. Geophys. Res.: Planets* **126**, e2020JE006639 (2021).
- Lopez, E. D. & Fortney, J. J. The role of core mass in controlling evaporation: the Kepler radius distribution and the Kepler-36 density dichotomy. *Astrophys. J.* **776**, 2 (2013).
- Ginzburg, S., Schlichting, H. E. & Sari, R. e. Core-powered mass-loss and the radius distribution of small exoplanets. *Mon. Not. Roy. Astron. Soc.* **476**, 759–765 (2018).
- Fulton, B. J. & Petigura, E. A. The California-Kepler survey. VII. Precise planet radii leveraging Gaia DR2 reveal the stellar mass dependence of the planet radius gap. *Astron. J.* **156**, 264 (2018).
- Chen, H. & Rogers, L. A. Evolutionary analysis of gaseous sub-Neptune-mass planets with MESA. *Astrophys. J.* **831**, 180 (2016).
- Owen, J. E. & Wu, Y. Kepler planets: a tale of evaporation. *Astrophys. J.* **775**, 105 (2013).
- Ikoma, M. & Hori, Y. In situ accretion of hydrogen-rich atmospheres on short-period super-Earths: implications for the Kepler-11 planets. *Astrophys. J.* **753**, 66 (2012).
- Hayashi, C., Nakazawa, K. & Mizuno, H. Earth's melting due to the blanketing effect of the primordial dense atmosphere. *Earth Planet. Sci. Lett.* **43**, 22–28 (1979).
- Wetherill, G. W. Formation of the terrestrial planets. *Annu. Rev. Astron. Astrophys.* **18**, 77–113 (1980).
- Zahnle, K. J. & Carlson, R. W. In *Planetary Astrobiology* (eds Meadows, V. S., Arney, G. N., Schmidt, B. E. & Des Marais, D. J.) 3–37 (University of Arizona Press, 2020).
- Zahnle, K. J. Earth's earliest atmosphere. *Elements* **2**, 217–222 (2006).
- Rubie, D. C. et al. Accretion and differentiation of the terrestrial planets with implications for the compositions of early-formed Solar System bodies and accretion of water. *Icarus* **248**, 89–108 (2015).
- Carlson, R. W., Brasser, R., Yin, Q.-Z., Fischer-Gödde, M. & Qin, L. Feedstocks of the terrestrial planets. *Space Sci. Rev.* **214**, 1–32 (2018).
- Fischer-Gödde, M. & Kleine, T. Ruthenium isotopic evidence for an inner Solar System origin of the late veneer. *Nature* **541**, 525–527 (2017).
- Young, E. D., Shahar, A. & Schlichting, H. E. Earth shaped by primordial H<sub>2</sub> atmospheres. *Nature* **616**, 306–311 (2023).
- Luger, R. et al. Habitable evaporated cores: transforming mini-Neptunes into super-Earths in the habitable zones of M dwarfs. *Astrobiology* **15**, 57–88 (2015).
- Owen, J. E. & Mohanty, S. Habitability of terrestrial-mass planets in the HZ of M Dwarfs—I. H/He-dominated atmospheres. *Mon. Not. Roy. Astron. Soc.* **459**, 4088–4108 (2016).
- Kite, E. S. & Barnett, M. N. Exoplanet secondary atmosphere loss and revival. *Proc. Natl Acad. Sci.* **117**, 18264–18271 (2020).
- Abe, Y. Thermal evolution and chemical differentiation of the terrestrial magma ocean. *Evol. Earth Planets* **74**, 41–54 (1993).
- Hamano, K., Abe, Y. & Genda, H. Emergence of two types of terrestrial planet on solidification of magma ocean. *Nature* **497**, 607–610 (2013).
- Schaefer, L., Wordsworth, R. D., Berta-Thompson, Z. & Sasselov, D. Predictions of the atmospheric composition of GJ 1132b. *Astrophys. J.* **829**, 63 (2016).
- Lebrun, T. et al. Thermal evolution of an early magma ocean in interaction with the atmosphere. *J. Geophys. Res.: Planets* **118**, 1155–1176 (2013).
- Krissansen-Totton, J., Fortney, J. J., Nimmo, F. & Wogan, N. Oxygen false positives on habitable zone planets around sun-like stars. *AGU Adv.* **2**, e2020AV000294 (2021).
- Trail, D., Watson, E. B. & Tailby, N. D. The oxidation state of Hadean magmas and implications for early Earth's atmosphere. *Nature* **480**, 79–82 (2011).
- Delano, J. W. Redox history of the Earth's interior since ~ 3900 Ma: implications for prebiotic molecules. *Origins Life Evol. Biosphere* **31**, 311–341 (2001).
- Barth, P. et al. Magma ocean evolution of the TRAPPIST-1 planets. *Astrobiology* **21**, 1325–1349 (2021).
- Lichtenberg, T. et al. Vertically resolved magma ocean–protoatmosphere evolution: H<sub>2</sub>, H<sub>2</sub>O, CO<sub>2</sub>, CH<sub>4</sub>, CO, O<sub>2</sub>, and N<sub>2</sub> as primary absorbers. *J. Geophys. Res.: Planets* **126**, e2020JE006711 (2021).
- Gaillard, F. et al. Redox controls during magma ocean degassing. *Earth Planet. Sci. Lett.* **577**, 117255 (2022).
- Bower, D. J., Hakim, K., Sossi, P. A. & Sanan, P. Retention of water in terrestrial magma oceans and carbon-rich early atmospheres. *Planet. Sci. J.* **3**, 93 (2022).
- Katyal, N. et al. Effect of mantle oxidation state and escape upon the evolution of Earth's magma ocean atmosphere. *Astron. Astrophys.* **643**, A81 (2020).
- Foley, B. J. The role of plate tectonic–climate coupling and exposed land area in the development of habitable climates on rocky planets. *Astrophys. J.* **812**, 36 (2015).
- Orcutt, B. N., Daniel, I. & Dasgupta, R. *Deep Carbon: Past to Present* (Cambridge University Press, 2019).
- Unterborn, C. T., Kabbes, J. E., Pigott, J. S., Reaman, D. M. & Panero, W. R. The role of carbon in extrasolar planetary geodynamics and habitability. *Astrophys. J.* **793**, 124 (2014).
- Wordsworth, R., Schaefer, L. & Fischer, R. Redox evolution via gravitational differentiation on low-mass planets: implications for abiotic oxygen, water loss, and habitability. *Astron. J.* **155**, 195 (2018).
- Wogan, N. F., Catling, D. C., Zahnle, K. J. & Lupu, R. Origin-of-life molecules in the atmosphere after big impacts on the early Earth. *Planet. Sci. J.* **4**, 169 (2023).
- Kite, E. S., & Ford, E. B. Habitability of exoplanet waterworlds. *Astron. J.* **864**, 75 (2018).
- Krissansen-Totton, J. & Fortney, J. J. Predictions for observable atmospheres of trappist-1 planets from a fully coupled atmosphere–interior evolution model. *Astrophys. J.* **933**, 115 (2022).
- Gillon, M. et al. Seven temperate terrestrial planets around the nearby ultracool dwarf star TRAPPIST-1. *Nature* **542**, 456–460 (2017).
- Miyazaki, Y. & Korenaga, J. Inefficient water degassing inhibits ocean formation on rocky planets: an insight from self-consistent mantle degassing models. *Astrobiology* **22**, 713–734 (2022).
- Lodders, K., Palme, H. & Gail, H.-P. In *The Solar System* (eds Trümper, J. E.) 712–770 (Landolt-Börnstein—Group VI Astronomy and Astrophysics, 2009).

46. Dong, C. et al. Atmospheric escape from the TRAPPIST-1 planets and implications for habitability. *Proc. Natl Acad. Sci.* **115**, 260–265 (2018).
47. Garcia-Sage, K., Glocer, A., Drake, J., Gronoff, G. & Cohen, O. On the magnetic protection of the atmosphere of Proxima Centauri b. *Astrophys. J. Lett.* **844**, L13 (2017).
48. Dong, C., Huang, Z. & Lingam, M. Role of planetary obliquity in regulating atmospheric escape: G-dwarf versus M-dwarf Earth-like exoplanets. *Astrophys. J. Lett.* **882**, L16 (2019).
49. Airapetian, V. S. et al. How hospitable are space weather affected habitable zones? The role of ion escape. *Astrophys. J. Lett.* **836**, L3 (2017).
50. De Wit, J. et al. Atmospheric reconnaissance of the habitable-zone Earth-sized planets orbiting TRAPPIST-1. *Nat. Astron.* **2**, 214–219 (2018).
51. Kimura, T. & Ikoma, M. Predicted diversity in water content of terrestrial exoplanets orbiting M dwarfs. *Nat. Astron.* **6**, 1296–1307 (2022).
52. Kimura, T. & Ikoma, M. Formation of aqua planets with water of nebular origin: effects of water enrichment on the structure and mass of captured atmospheres of terrestrial planets. *Mon. Not. Roy. Astron. Soc.* **496**, 3755–3766 (2020).
53. Greene, T. P. et al. Thermal emission from the Earth-sized exoplanet TRAPPIST-1 b using JWST. *Nature* **618**, 39–42 (2023).
54. Zieba, S. et al. No thick carbon dioxide atmosphere on the rocky exoplanet TRAPPIST-1 c. *Nature* **620**, 746–749 (2023).
55. Turbet, M. et al. Water condensation zones around main sequence stars. *Astronomy & Astrophysics* **679**, A126 (2023).
56. Krissansen-Totton, J. Implications of atmospheric non-detections for Trappist-1 inner planets on atmospheric retention prospects for outer planets. *ApJL* **951**, L39 (2023).
57. Turbet, M. et al. Modeling climate diversity, tidal dynamics and the fate of volatiles on TRAPPIST-1 planets. *Astron. Astrophys.* **612**, A86 (2018).
58. Turbet, M. et al. A review of possible planetary atmospheres in the TRAPPIST-1 system. *Space Sci. Rev.* **216**, 1–48 (2020).
59. Kral, Q. et al. Cometary impactors on the TRAPPIST-1 planets can destroy all planetary atmospheres and rebuild secondary atmospheres on planets f, g, and h. *Mon. Not. Roy. Astron. Soc.* **479**, 2649–2672 (2018).
60. Raymond, S. N. et al. An upper limit on late accretion and water delivery in the TRAPPIST-1 exoplanet system. *Nat. Astron.* **6**, 80–88 (2022).
61. Lissauer, J. J. Planets formed in habitable zones of M dwarf stars probably are deficient in volatiles. *Astrophys. J.* **660**, L149 (2007).
62. Van Looveren, G., Güdel, M., Saikia, S. B., & Kislyakova, K. Airy worlds or barren rocks? On the survivability of secondary atmospheres around the TRAPPIST-1 planets. *Astronomy & Astrophysics* **683**, A153 (2024).
63. Nakayama, A., Ikoma, M. & Terada, N. Survival of terrestrial N<sub>2</sub>-O<sub>2</sub> atmospheres in violent XUV environments through efficient atomic line radiative cooling. *Astrophys. J.* **937**, 72 (2022).
64. Noack, L. et al. Water-rich planets: How habitable is a water layer deeper than on Earth? *Icarus* **277**, 215–236 (2016).
65. Journaux, B. et al. Holistic approach for studying planetary hydrospheres: Gibbs representation of ices thermodynamics, elasticity, and the water phase diagram to 2,300 MPa. *J. Geophys. Res.: Planets* **125**, e2019JE006176 (2020).
66. Agol, E. et al. Refining the transit-timing and photometric analysis of TRAPPIST-1: masses, radii, densities, dynamics, and ephemerides. *Planet. Sci. J.* **2**, 1 (2021).
67. Schlichting, H. E. & Young, E. D. Chemical equilibrium between cores, mantles, and atmospheres of super-earths and sub-neptunes and implications for their compositions, interiors, and evolution. *Planet. Sci. J.* **3**, 127 (2022).
68. Misener, W. & Schlichting, H. E. The importance of silicate vapour in determining the structure, radii, and envelope mass fractions of sub-Neptunes. *Mon. Not. Roy. Astron. Soc.* **514**, 6025–6037 (2022).
69. Misener, W., Schlichting, H. E. & Young, E. D. Atmospheres as windows into sub-Neptune interiors: coupled chemistry and structure of hydrogen-silane-water envelopes. *Mon. Not. Roy. Astron. Soc.* **524**, 981–992 (2023).
70. Barton, T. J. & Boudjouk, P. *Organosilicon Chemistry: A Brief overview* (ACS Publications, 1990).
71. Voge, H. Carbon-hydrogen bond strengths in methane. *J. Chem. Phys.* **16**, 984–986 (1948).
72. Shorttle, O., Jordan, S., Nicholls, H., Lichtenberg, T. & Bower, D. J. Distinguishing oceans of water from magma on mini-Neptune K2-18b. *Astrophys. J. Lett.* **962**, L8 (2024).
73. Wogan, N. F. et al. JWST observations of K2-18b can be explained by a gas-rich mini-Neptune with no habitable surface. *Astrophys. J. Lett.* **963**, L7 (2024).
74. Dasgupta, R. & Grewal, D. S. In *Deep Carbon* (eds Orcutt, B. N., Daniel, I., Dasgupta, R.) 4–39 (Cambridge University Press, 2019).
75. Fischer, R. A., Cottrell, E., Hauri, E., Lee, K. K. & Le Voyer, M. The carbon content of Earth and its core. *Proc. Natl Acad. Sci.* **117**, 8743–8749 (2020).
76. Grewal, D. S., Dasgupta, R., Sun, C., Tsuno, K. & Costin, G. Delivery of carbon, nitrogen, and sulfur to the silicate Earth by a giant impact. *Sci. Adv.* **5**, eaau3669 (2019).
77. Benneke, B. et al. JWST Reveals CH<sub>4</sub>, CO<sub>2</sub>, and H<sub>2</sub>O in a metal-rich miscible atmosphere on a two-earth-radius exoplanet. Preprint at <https://arxiv.org/abs/2403.03325> (2024).
78. Holmberg, M. & Madhusudhan, N. Possible Hycean conditions in the sub-Neptune TOI-270 d. *Astron. Astrophys.* **683**, L2 (2024).
79. Clesi, V. et al. Low hydrogen contents in the cores of terrestrial planets. *Sci. Adv.* **4**, e1701876 (2018).
80. Rubie, D. C. et al. Heterogeneous accretion, composition and core-mantle differentiation of the Earth. *Earth Planet. Sci. Lett.* **301**, 31–42 (2011).
81. Chen, H. & Jacobson, S. A. Impact induced atmosphere-mantle exchange sets the volatile elemental ratios on primitive Earths. *Earth Planet. Sci. Lett.* **594**, 117741 (2022).
82. Mollière, P. et al. petitRADTRANS-A Python radiative transfer package for exoplanet characterization and retrieval. *Astron. Astrophys.* **627**, A67 (2019).
83. Rothman, L. S. et al. HITEMP, the high-temperature molecular spectroscopic database. *J. Quantitative Spectrosc. Radiat. Transfer* **111**, 2139–2150 (2010).
84. Marcq, E., Salvador, A., Massol, H. & Davaille, A. Thermal radiation of magma ocean planets using a 1-D radiative-convective model of H<sub>2</sub>O-CO<sub>2</sub> atmospheres. *J. Geophys. Res.: Planets* **122**, 1539–1553 (2017).
85. Pluriel, W., Marcq, E. & Turbet, M. Modeling the albedo of Earth-like magma ocean planets with H<sub>2</sub>O-CO<sub>2</sub> atmospheres. *Icarus* **317**, 583–590 (2019).
86. Kopparapu, R. K. et al. Habitable zones around main-sequence stars: new estimates. *Astrophys. J.* **765**, 131 (2013).
87. Selsis, F., Leconte, J., Turbet, M., Chaverot, G. & Bolmont, É. A cool runaway greenhouse without surface magma ocean. *Nature* **620**, 287–291 (2023).
88. Burcat, A. & Ruscic, B. *Third Millennium Ideal Gas and Condensed Phase Thermochemical Database for Combustion (with update from active thermochemical tables)*. (Argonne National Lab.(ANL), Argonne, IL (United States), 2005).
89. Iacono-Marziano, G., Morizet, Y., Le Trong, E. & Gaillard, F. New experimental data and semi-empirical parameterization of H<sub>2</sub>O-CO<sub>2</sub> solubility in mafic melts. *Geochim. Cosmochim. Acta* **97**, 1–23 (2012).

90. Hirschmann, M., Withers, A., Ardia, P. & Foley, N. Solubility of molecular hydrogen in silicate melts and consequences for volatile evolution of terrestrial planets. *Earth Planet. Sci. Lett.* **345**, 38–48 (2012).
91. Kress, V. C. & Carmichael, I. S. The compressibility of silicate liquids containing Fe<sub>2</sub>O<sub>3</sub> and the effect of composition, temperature, oxygen fugacity and pressure on their redox states. *Contrib. Mineral. Petrol.* **108**, 82–92 (1991).
92. Frost, B. R. In *Oxide Minerals* (ed. Lindsley, D. H.) 1–10 (De Gruyter, 2018).
93. Hirschmann, M. Magma oceans, iron and chromium redox, and the origin of comparatively oxidized planetary mantles. *Geochim. Cosmochim. Acta* **328**, 221–241 (2022).
94. Ma, Z. Thermodynamic description for concentrated metallic solutions using interaction parameters. *Metallur. Mater. Trans. B* **32**, 87–103 (2001).
95. Salvador, A. & Samuel, H. Convective outgassing efficiency in planetary magma oceans: insights from computational fluid dynamics. *Icarus* **390**, 115265 (2023).
96. Schaefer, L., Jacobsen, S. B., Remo, J. L., Petaev, M. & Sasselov, D. D. Metal-silicate partitioning and its role in core formation and composition on super-Earths. *Astrophys. J.* **835**, 234 (2017).
97. Armstrong, K., Frost, D. J., McCammon, C. A., Rubie, D. C. & Boffa Ballaran, T. Deep magma ocean formation set the oxidation state of Earth's mantle. *Science* **365**, 903–906 (2019).
98. Deng, J., Du, Z., Karki, B. B., Ghosh, D. B. & Lee, K. K. A magma ocean origin to divergent redox evolutions of rocky planetary bodies and early atmospheres. *Nat. Commun.* **11**, 2007 (2020).
99. Baraffe, I., Homeier, D., Allard, F. & Chabrier, G. New evolutionary models for pre-main sequence and main sequence low-mass stars down to the hydrogen-burning limit. *Astron. Astrophys.* **577**, A42 (2015).
100. Tu, L., Johnstone, C. P., Güdel, M. & Lammer, H. The extreme ultraviolet and X-ray Sun in Time: High-energy evolutionary tracks of a solar-like star. *Astron. Astrophys.* **577**, L3 (2015).
101. Birky, J., Barnes, R. & Fleming, D. P. Improved constraints for the XUV luminosity evolution of trappist-1. *Res. Notes AAS* **5**, 122 (2021).
102. Catling, D. C. & Kasting, J. F. *Atmospheric Evolution on Inhabited and Lifeless Worlds* (Cambridge University Press, 2017).
103. Odert, P. et al. Escape and fractionation of volatiles and noble gases from Mars-sized planetary embryos and growing protoplanets. *Icarus* **307**, 327–346 (2018).
104. Zahnle, K. J. & Kasting, J. F. Mass fractionation during transonic escape and implications for loss of water from Mars and Venus. *Icarus* **68**, 462–480 (1986).
105. Zahnle, K. & Kasting, J. F. Elemental and isotopic fractionation as fossils of water escape from Venus. *Geochim. Cosmochim. Acta* **361**, 228–244 (2023).
106. Hier-Majumder, S. & Hirschmann, M. M. The origin of volatiles in the Earth's mantle. *Geochem. Geophys. Geosyst.* **18**, 3078–3092 (2017).
107. Nittler, L. R. & Weider, S. Z. The surface composition of Mercury. *Elements: Int. Mag. Mineral. Geochem. Petrol.* **15**, 33–38 (2019).
108. Lichtenberg, T. Redox hysteresis of super-Earth exoplanets from magma ocean circulation. *Astrophys. J. Lett.* **914**, L4 (2021).
109. Rogers, J. G., Schlichting, H. E., & Young, E. D. Fleeting but Not Forgotten: The Imprint of Escaping Hydrogen Atmospheres on Super-Earth Interiors. *Astron. J.* **970**, 47 (2024).
110. Rubie, D., Melosh, H., Reid, J., Liebske, C. & Richter, K. Mechanisms of metal-silicate equilibration in the terrestrial magma ocean. *Earth Planet. Sci. Lett.* **205**, 239–255 (2003).
111. Marty, B. The origins and concentrations of water, carbon, nitrogen and noble gases on Earth. *Earth Planet. Sci. Lett.* **313**, 56–66 (2012).
112. Hirschmann, M. M. Constraints on the early delivery and fractionation of Earth's major volatiles from C/H, C/N, and C/S ratios. *Am. Mineralogist* **101**, 540–553 (2016).
113. Sun, C. & Dasgupta, R. Carbon budget of Earth's deep mantle constrained by petrogenesis of silica-poor ocean island basalts. *Earth Planet. Sci. Lett.* **611**, 118135 (2023).
114. Johnstone, C. P., Güdel, M., Lammer, H. & Kislyakova, K. G. Upper atmospheres of terrestrial planets: carbon dioxide cooling and the Earth's thermospheric evolution. *Astron. Astrophys.* **617**, A107 (2018).
115. Johnstone, C. P., Lammer, H., Kislyakova, K. G., Scherf, M. & Güdel, M. The young Sun's XUV-activity as a constraint for lower CO<sub>2</sub>-limits in the Earth's Archean atmosphere. *Earth. Planet. Sci. Lett.* **576**, 117197 (2021).
116. Lichtenegger, H. et al. Solar XUV and ENA-driven water loss from early Venus' steam atmosphere. *J. Geophys. Res. Space Phys.* **121**, 4718–4732 (2016).

## Acknowledgements

J.K.T acknowledges support from NASA Astrophysics Precursor Science Grant 80NSSC23K1471 and the Virtual Planetary Laboratory, which is a member of the NASA Nexus for Exoplanet System Science, and funded via NASA Astrobiology Program Grant 80NSSC23K1398.

## Author contributions

J.K.-T. designed the study and performed calculations, N.W. provided numerical methods expertise and contributed to magma ocean code development, M.T. contributed to the climate model development, J.J.F. provided expertise on radiative convective climate models and sub-Neptune evolution. All authors contributed to drafting and editing the manuscript.

## Competing interests

The authors declare no competing interests.

## Additional information

**Supplementary information** The online version contains supplementary material available at <https://doi.org/10.1038/s41467-024-52642-6>.

**Correspondence** and requests for materials should be addressed to Joshua Krissansen-Totton.

**Peer review information** *Nature Communications* thanks Emmanuel Marcq, and the other, anonymous, reviewer(s) for their contribution to the peer review of this work. A peer review file is available.

**Reprints and permissions information** is available at <http://www.nature.com/reprints>

**Publisher's note** Springer Nature remains neutral with regard to jurisdictional claims in published maps and institutional affiliations.

**Open Access** This article is licensed under a Creative Commons Attribution 4.0 International License, which permits use, sharing, adaptation, distribution and reproduction in any medium or format, as long as you give appropriate credit to the original author(s) and the source, provide a link to the Creative Commons licence, and indicate if changes were made. The images or other third party material in this article are included in the article's Creative Commons licence, unless indicated otherwise in a credit line to the material. If material is not included in the article's Creative Commons licence and your intended use is not permitted by statutory regulation or exceeds the permitted use, you will need to obtain permission directly from the copyright holder. To view a copy of this licence, visit <http://creativecommons.org/licenses/by/4.0/>.

© The Author(s) 2024

## **Supplementary Materials**

### **The erosion of large primary atmospheres typically leaves behind substantial secondary atmospheres on temperate rocky planets**

Joshua Krissansen-Totton<sup>1,2\*</sup>, Nicholas Wogan<sup>2,3</sup>, Maggie Thompson<sup>4</sup>, Jonathan J. Fortney<sup>5</sup>

<sup>1</sup>Department of Earth and Space Sciences/Astrobiology Program, University of Washington, Seattle WA, USA

<sup>2</sup>NASA NExSS Virtual Planetary Laboratory, University of Washington, Seattle, WA 98195, USA

<sup>3</sup>NASA Ames Research Center, Moffett Field, CA, USA

<sup>4</sup>Department of Earth Sciences, ETH Zurich, Switzerland

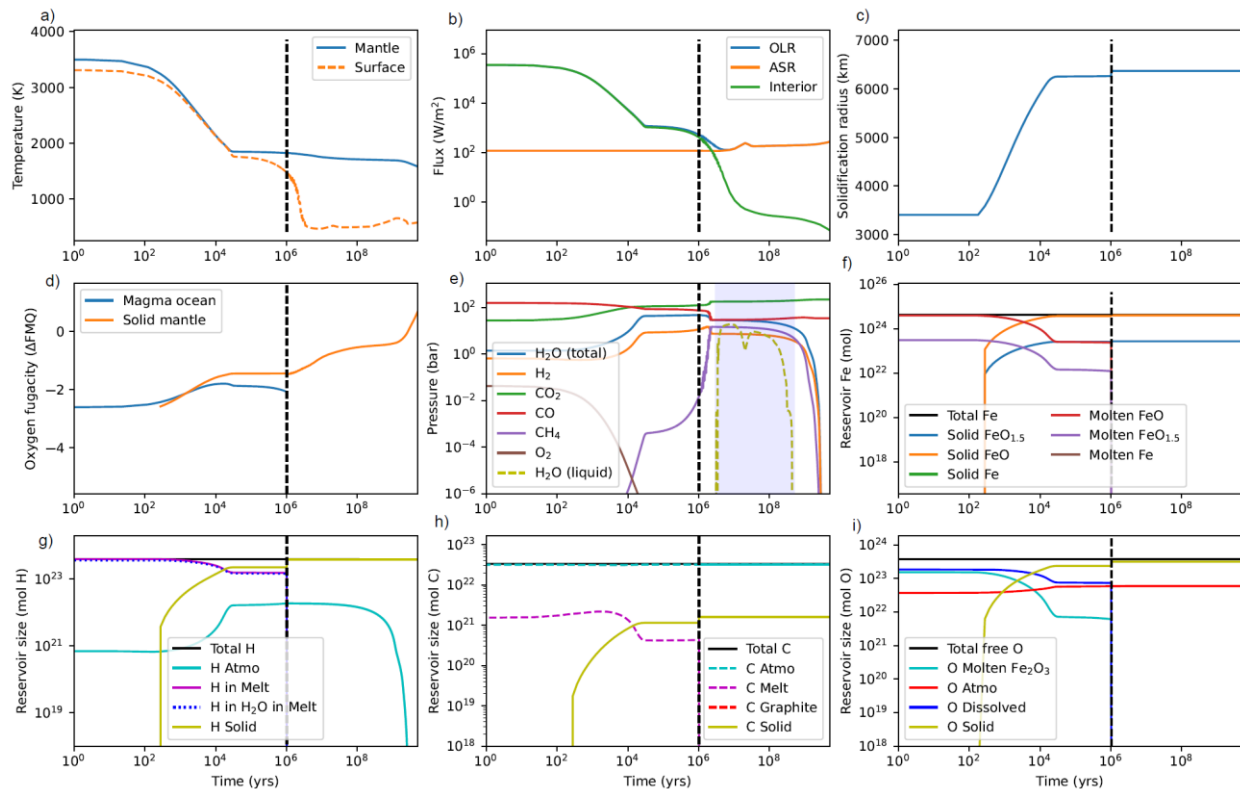
<sup>5</sup>Department of Astronomy and Astrophysics, University of California, Santa Cruz, Santa Cruz, CA 95064, USA

\*Contact: [joshkt@uw.edu](mailto:joshkt@uw.edu)

## Model Validation

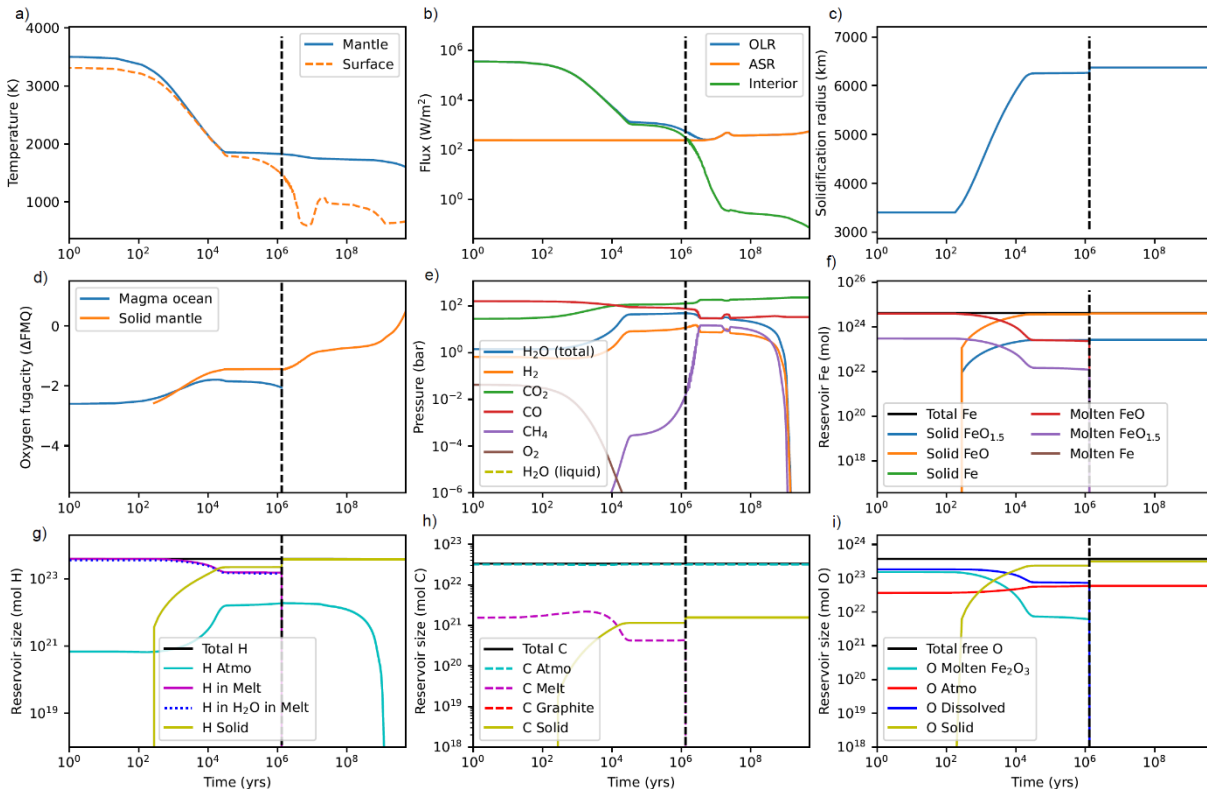
### Earth and Venus Validation

Fig. S1 and S2 show the magma ocean model applied to an Earth and Venus magma ocean, respectively. Here, we assume the traditional view whereby Earth and Venus do not form with a substantial  $H_2$  envelope and are left with only a few Earth oceans equivalent of H following the moon-forming impact, in the case of the Earth (and similar volatile endowments for Venus). Consistent with recent studies of Earth's magma ocean, it takes around  $\sim 1$  Myr for the magma ocean to solidify, and most water is retained in the mantle due to melt trapping and the high solubility of water in silicate melts [1-4]. The atmosphere that emerges from the magma ocean is  $CO_2$ -dominated, with some  $CO$  and a small amount of liquid water (5-10% of an Earth ocean) on the surface. Note that in this calculation Earth's surface water is all lost to space since we do not consider subsequent degassing of water in the mantle [1], nor include a temperate carbon cycle to draw down  $CO_2$  [5, 6]. The validation test for Venus is similar except that, for our assumed Bond albedo, water does not condense due to higher insolation, leading to the eventual desiccation by the loss of water to space. We leave a more detailed Earth-Venus comparison with this model for future work, but note that this generalization of magma ocean models to all C, H, O, and Fe-bearing species does not dramatically change the classical view of the Earth-Venus evolutionary dichotomy [7] when relatively oxidized starting conditions and chondritic compositions are assumed.



**Fig. S1: Nominal Earth.** Subplot (a) denotes the time-evolution of surface (orange) and mantle potential temperature (blue), (b) denotes the evolution of outgoing longwave radiation (OLR, blue), absorbed shortwave radiation (ASR, orange), and interior heatflow (green), and subplot (c) shows the evolution of the magma ocean solidification front from the core-mantle boundary to the surface. Subplot (d) shows solid mantle (orange) and magma ocean redox (blue) relative to the Fayalite-Quartz-Magnetite (FMQ)

buffer, (e) shows the evolution of atmospheric composition including  $\text{H}_2\text{O}$ ,  $\text{H}_2$ ,  $\text{CO}_2$ ,  $\text{CO}$ ,  $\text{CH}_4$ ,  $\text{O}_2$ , and condensed/liquid  $\text{H}_2\text{O}$ . Subplot (f) denotes iron speciation in both the magma ocean and the solid silicate mantle – in this oxidizing Earth-analog case no metallic iron is produced. Subplot (g) shows both solid and fluid reservoirs of H; total dissolved hydrogen (purple) and hydrogen dissolved as  $\text{H}_2\text{O}$  (blue-dotted) are essentially identical in this oxidized scenario where dissolved  $\text{H}_2$  is minimal. Subplot (h) denotes solid and fluid reservoirs of C and subplot (i) denotes solid and fluid reservoirs of free oxygen, including oxygen bound to ferric iron, atmospheric species, and O in volatiles dissolved in the melt ( $\text{H}_2\text{O}$ ,  $\text{CO}_2$ ) reservoirs respectively. Vertical dashed black lines show the termination of the magma ocean, which takes  $\sim 10^6$  years in this case. The blue shaded region denotes the timespan over which liquid water is stable on the surface – this provides a window of opportunity for  $\text{H}_2\text{O}$  degassing via volcanism, and the removal of  $\text{CO}_2$  via weathering to form carbonates (neither of which are included in this model).



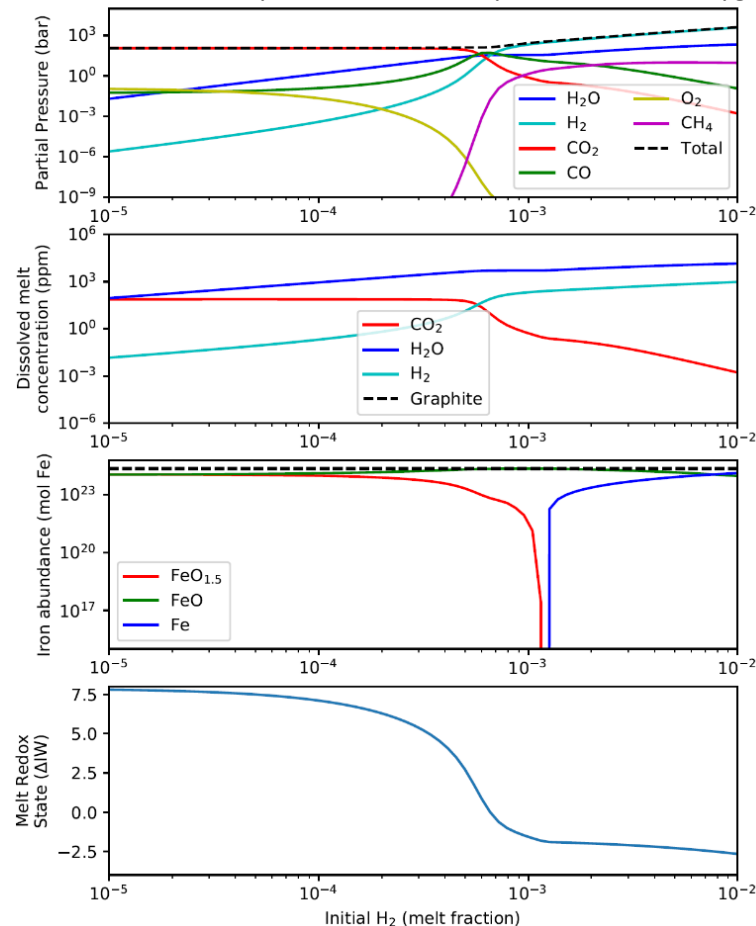
**Fig. S2: Nominal Venus.** Subplot (a) denotes the time-evolution of surface (orange) and mantle potential temperature (blue), (b) denotes the evolution of outgoing longwave radiation (OLR, blue), absorbed shortwave radiation (ASR, orange), and interior heatflow (green), and subplot (c) shows the evolution of the magma ocean solidification front from the core-mantle boundary to the surface. Subplot (d) shows solid mantle (orange) and magma ocean redox (blue) relative to the Fayalite-Quartz-Magnetite (FMQ) buffer, (e) shows the evolution of atmospheric composition including  $\text{H}_2\text{O}$ ,  $\text{H}_2$ ,  $\text{CO}_2$ ,  $\text{CO}$ ,  $\text{CH}_4$ ,  $\text{O}_2$ , atmospheric (non-condensed)  $\text{H}_2\text{O}$ . Subplot (f) denotes iron speciation in both the magma ocean and the solid silicate mantle – in this oxidizing Earth-analog case no metallic iron is produced. Subplot (g) shows both solid and fluid reservoirs of H; total dissolved hydrogen (purple) and hydrogen dissolved as  $\text{H}_2\text{O}$  (blue-dotted) are essentially identical in this oxidized scenario where dissolved  $\text{H}_2$  is minimal. Subplot (h) denotes solid and fluid reservoirs of C and subplot (i) denotes solid and fluid reservoirs of free oxygen, including oxygen bound to ferric iron, atmospheric species, and O in volatiles dissolved in the melt ( $\text{H}_2\text{O}$ ,  $\text{CO}_2$ ) reservoirs respectively. Vertical dashed black lines show the termination of the

magma ocean, which takes  $\sim 10^6$  years in this case. Liquid water is not stable on the surface at any point in this particular model run, and so hydrogen is lost to space until Venus is completely desiccated.

Note that for both the Earth-analog and Venus-analog calculations above around  $\sim 2\text{-}10\%$  of  $\text{CO}_2$  is retained in the mantle, broadly in line with previous studies [8, 9], as well as the TRAPPIST-1e results with BSE volatile endowments (Fig. 2). Far less C is retained in the mantle in Fig. 3 and 4, which is attributable to the reducing conditions created by the nebular atmosphere. Under reducing conditions,  $\text{CO}_2$  is a small fraction of the total atmospheric carbon, and so the resultant dissolved carbonate melt fraction is similarly low. We neglect  $\text{CH}_4$  and  $\text{CO}$  solubility – a conservative assumption that prevents reduced forms of C dissolving in the magma ocean, potentially shielding it from escape.

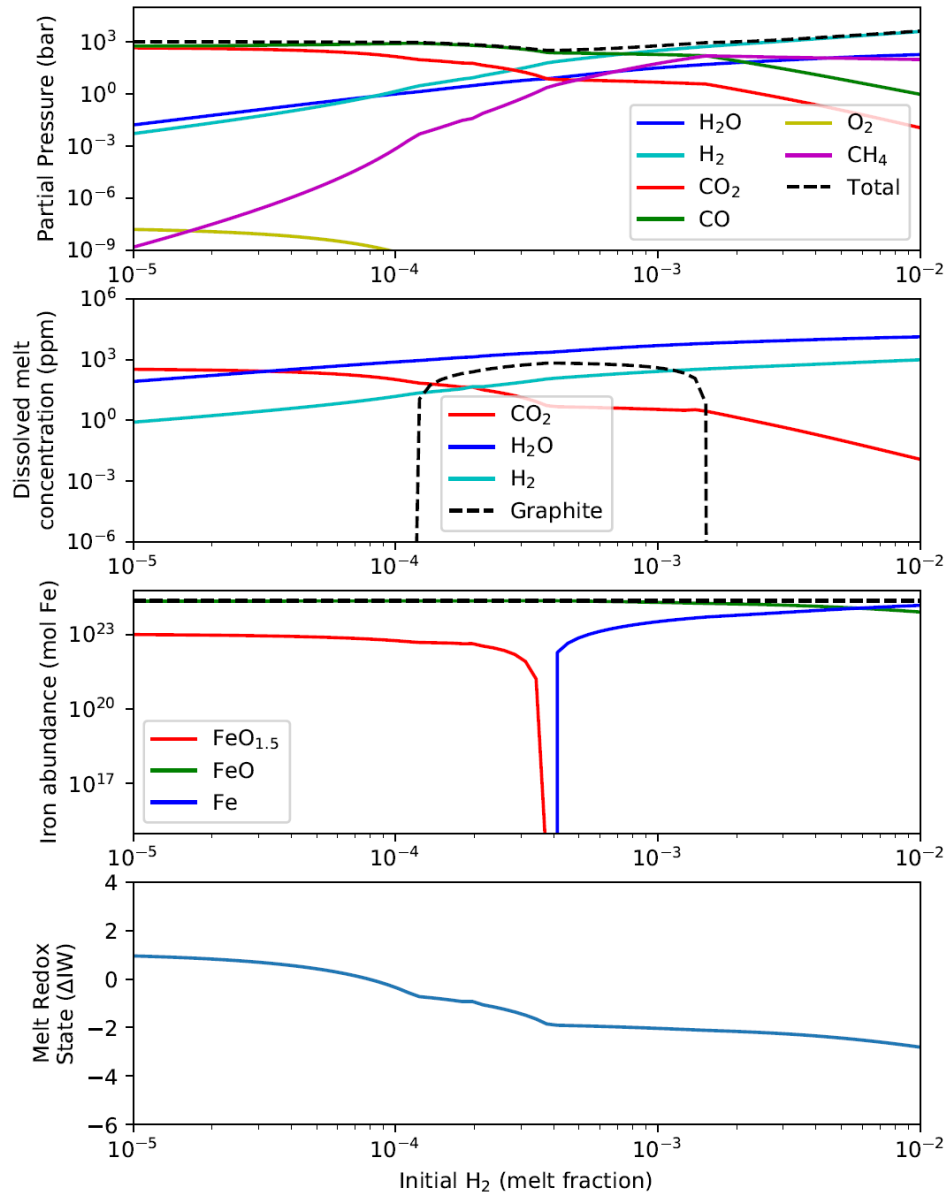
### Volatile-Partitioning Validation

Fig. S3 shows an example volatile partitioning + redox equilibration calculation for a test case with  $10^{22}$  kg free oxygen,  $2 \times 10^{24}$  kg melt,  $1500^\circ\text{C}$ , and 100 ppm C (initial melt fraction). The initial  $\text{H}_2$  melt fraction was varied from 10 ppm to 1%, and the multiphase equilibrium state is calculated at each point as described in Methods. Subplots denote gas phase partial pressures, dissolved species concentrations, iron speciation in the melt, and melt oxygen fugacity relative to the Iron-Wustite buffer, respectively. Conditions are relatively oxidizing at low initial H i.e.  $\text{CO}_2$  dominates the atmosphere,  $\sim$ half of iron oxidized to  $\text{FeO}_{1.5}$ , and an oxygen fugacity around  $\text{IW}+7.5$ . However, as the initial H inventory is increased the atmosphere transitions to  $\text{CO}$ -dominated, then  $\text{H}_2$  dominated. Iron speciation transitions from an  $\text{FeO}_{1.5}$ - $\text{FeO}$  system to a  $\text{FeO}$ - $\text{Fe}$  system, and melt oxygen fugacity approaches  $\text{IW}-3$ .



**Fig. S3:** Example multiphase equilibrium and volatile partitioning calculation. In this case the planet is endowed with  $10^{22}$  kg free oxygen,  $2 \times 10^{24}$  kg silicate melt (half Earth's mantle), 100 ppm C, and calculations are performed at  $1500^\circ\text{C}$ . From top to bottom, subplots denote atmospheric species, volatiles dissolved in the silicate melt, iron speciation in the melt, and melt redox state relative to IW.

Fig. S4 is similar except that the initial C endowment is higher (1000 ppm), and there is less free oxygen  $5 \times 10^{21}$  kg). Under these more reducing, carbon-rich conditions, a CO-rich atmosphere is expected for low initial H, and graphite can precipitate out of the melt. Note, however, that under extremely reducing conditions  $\text{CH}_4$  dominates over CO and  $\text{CO}_2$  and the melt is no longer graphite saturated.



**Fig. S4:** Example multiphase equilibrium and volatile partitioning calculation. In this case the planet is endowed with  $5 \times 10^{21}$  kg free oxygen,  $2 \times 10^{24}$  kg silicate melt (half Earth's mantle), and 1000 ppm C, and calculations are performed at  $1500^\circ\text{C}$ . From top to bottom, subplots denote atmospheric species, volatiles dissolved in the silicate melt, iron speciation in the melt, and melt redox state relative to IW.

## Supplementary Methods

### Graphite saturation

Following Ortenzi et al. [10], we permit graphite saturation when calculating melt-solid-gaseous partitioning of carbon. The concentration of carbon dissolved in a graphite-saturated melt in redox state dependent:

$$m_{CO_3, graphite-sat} = \frac{K_{1, graphite} K_{2, graphite} fO_2}{1 + K_{1, graphite} K_{2, graphite} fO_2} \quad (1)$$

$$m_{CO_2, graphite-sat} = \frac{(44/36.594)m_{CO_3, graphite-sat}}{1 - (1 - 44/36.594)m_{CO_3, graphite-sat}} \quad (2)$$

Here,  $fO_2$  is mantle oxygen fugacity, and we are converting between dissolved carbonate and carbon dioxide concentrations. The temperature and pressure-dependent equilibrium constants are defined as follows:

$$\begin{aligned} \log_{10}(K_{1, graphite}) &= 40.07639 - 2.53932 \times 10^{-2} T + 5.27096 \times 10^{-6} T^2 + 0.0267(P - 1) / T \\ \log_{10}(K_{2, graphite}) &= -6.24763 - 282.56 / T - 0.119242(P - 1000) / T \end{aligned} \quad (3)$$

When computing melt-volatile-redox equilibrium, if  $m_{CO_2, graphite-sat} > m_{CO_2}$  then the melt is assumed undersaturated with respect to graphite and  $n_{graphite} = 0$ . Otherwise, dissolved  $CO_2$  concentration is adjusted downwards such that  $m_{CO_2} = m_{CO_2, graphite-sat}$  and  $n_{graphite}$  is included in the carbon mass balance.

### Transition between iron speciation parameterizations

Recall that for comparatively oxidized silicates, the relationship between ferrous and ferric iron abundances is determined by oxygen fugacity [11]:

$$\begin{aligned} \ln\left(\frac{X_{FeO_{1.5}}}{X_{FeO}}\right) &= 0.196 \times \ln(fO_2) - 1.828 X_{FeO_{Tot}} + 11492/T - 6.675 - 2.243 X_{Al_2O_3} + 3.201 X_{CaO} \\ &+ 5.854 X_{Na_2O} + 6.215 X_{K_2O} - 3.36 \left(1 - \frac{1673}{T} - \ln\left(\frac{T}{1673}\right)\right) - 7.01 \times 10^{-7} \frac{P}{T} - 1.54 \times 10^{-10} P \frac{(T - 1673)}{T} \\ &+ 3.85 \times 10^{-17} \frac{P^2}{T} \end{aligned} \quad (4)$$

Here,  $X_i$  represent the mole fraction of the  $i$ -th species in the silicate melt where non Fe-bearing species are fixed bulk silicate Earth values [12],  $P$  (Pa) is pressure, and  $T$  (K) is the melt temperature. We assume metallic iron is negligible for this oxidized case.

For reducing melts, ferrous iron and metallic iron abundances are related to oxygen fugacity as follows:

$$2 \times \log_{10} \left( \frac{1.5 X_{FeO}}{0.8 X_{Fe}} \right) = \log_{10} (fO_2) - \log_{10} (fO_2 (IW)) \quad (5)$$

Here, ferric iron is assumed negligible, the mole fraction of iron in the metallic phase,  $X_{Fe}$  equals 1, and activity coefficients representative of typical surface conditions have been chosen for iron oxide, 1.5, and metallic iron, 0.8 [13, 14]. The oxygen fugacity at the iron wustite (IW) buffer is calculated from surface temperature and pressure using [15]:

$$\log_{10} (fO_2 (IW)) = \frac{-27215}{T} + 6.57 + 0.0552 \frac{(P-1)}{T} \quad (6)$$

According to this equation, metallic iron begins to form in the melt when oxygen fugacity is less than:

$$fO_2 (transition) = 10^{\left( 2 \log_{10} \left( \frac{1.5 X_{FeO_{Tot}}}{0.8} \right) + \log_{10} (fO_2 (IW)) \right)} \quad (7)$$

For oxygen fugacities exceeding 10x this transition oxygen fugacity, we assume iron speciation is governed entirely by equation (4). For, oxygen fugacities less than the transition oxygen fugacity,  $X_{FeO_{1.5}} = 0$  and iron is partitioned between metallic and ferrous phases by equation (5). For intermediate oxygen fugacities, metallic iron is zero but we make the following smooth interpolation for numerical efficiency:

$$\begin{aligned} \ln \left( \frac{X_{FeO_{1.5}}}{X_{FeO}} \right) = & 0.196 \times \ln (fO_2) - 1.828 X_{FeO_{Tot}} + \frac{11492}{T} - 6.675 - 2.243 X_{Al_2O_3} + 3.201 X_{CaO} + 5.854 X_{Na_2O} \\ & + 6.215 X_{K_2O} - 3.36 \left( 1 - \frac{1673}{T} - \ln \left( \frac{T}{1673} \right) \right) - 7.01 \times 10^{-7} \frac{P}{T} - 1.54 \times 10^{-10} P \frac{(T-1673)}{T} + 3.85 \times 10^{-17} \frac{P^2}{T} \\ & + 1 - \left( \frac{1}{\log_{10} (fO_2) - \log_{10} (fO_2 (transition))} \right) \end{aligned} \quad (8)$$

The final term ensures that  $X_{FeO_{1.5}}$  smoothly goes to zero as the iron wustite buffer is approached, and tends to zero as oxygen fugacity approaches ten times the transition abundance.

### Escape parameterization

Atmospheric thermal escape is assumed to be either diffusion-limited or XUV-limited, depending on atmospheric composition and the incident stellar XUV flux. In the diffusion limit, we assume that eddy diffusion dominates vertical transport at altitudes where water is more abundant than atomic H and O [16], and so escape of hydrogen is limited by the diffusion of atomic hydrogen through the background atmosphere:

$$\varphi_{diff} = b_H f_H \left( \frac{1}{H_n} - \frac{1}{H_H} \right) \quad (9)$$

$$b_H = \frac{b_{H-CO}pCO + b_{H-N_2}pN_2 + b_{H-O}pO}{pCO + pN_2 + pO} \quad (10)$$

$$H_H = \frac{8.314T_{cold-trap}}{M_H g} \quad (11)$$

$$H_n = \frac{8.314T_{cold-trap}}{\bar{M}g} \quad (12)$$

Here,  $b_{i-j}$  (mol/m/s) is the binary diffusion coefficient of the  $i$ -th species through the  $j$ -th species [17, 18]. These are weighted by the thermosphere mixing ratios of each non-condensable constituent (CO, N<sub>2</sub>, and atomic O), which are obtained from the upper atmosphere mixing ratios, and from assuming that all H<sub>2</sub>O, H<sub>2</sub>, O<sub>2</sub>, and CO<sub>2</sub> is photodissociated to CO, O and H (N<sub>2</sub> background is fixed); the mixing ratio of atomic hydrogen,  $f_H$ , is similarly calculated (see below). The scale height of hydrogen,  $H_H$  (m), and of the background gases,  $H_n$  (m), depend on upper atmosphere temperature,  $T_{cold-trap}$ . The diffusion limited escape flux is  $\varphi_{diff}$  (mol H/m<sup>2</sup>/s).

To calculate XUV-driven hydrodynamic escape of H, and associated O and CO<sub>2</sub> drag, we follow Odert et al. [19] and Zahnle and Kasting [18]. The total XUV-energy mass loss rate,  $\Phi_{XUV}$  (kg/m<sup>2</sup>/s) is specified by the following equation:

$$\Phi_{XUV} = \frac{\varepsilon(F_{XUV}, X_O, \zeta, \varepsilon_{lowXUV})F_{XUV}r_p}{4GM_p} \quad (13)$$

Here,  $F_{XUV}$  is the XUV flux (W/m<sup>2</sup>) received from the host star. The efficiency of hydrodynamic escape,  $\varepsilon$ , is a function of atmospheric composition and XUV stellar flux [20]. In general, the XUV-driven mass flux will be partitioned between H loss, O drag and, under very high XUV fluxes, CO drag [19, 20]. For example, the oxygen fractionation factor,  $\chi_O$ , can be obtained:

$$\chi_O = 1 - \frac{g(m_O - m_H)b_{H-O}}{\Phi_H k_B T_{thermo} (1 + X_O)} \quad (14)$$

Here,  $T_{thermo}$  is the thermosphere temperature described in the main text,  $k_B$  is the Boltzmann constant,  $m_i$  (kg) is the mass of the  $i$ -th species,  $X_O$  is the upper atmosphere mixing ratio of oxygen. The hydrogen escape flux,  $\Phi_H$  (molecules H/m<sup>2</sup>/s), can be obtained by analytically solving equations (4), (5), and (6) in Odert et al. [19].

Note that we do not explicitly track changing relative abundances of atmospheric constituents above the homopause. Instead, molecular mixing ratios above the cold trap are converted to atomic mixing ratios as follows:

$$f_H = \frac{2f_{H_2O} + 2f_{H_2} + 4f_{CH_4}}{3f_{H_2O} + 2f_{H_2} + 4f_{CH_4} + 2f_{O_2} + 2f_{CO_2} + f_{CO} + f_{N_2}} \quad (15)$$

$$f_O = \frac{f_{H_2O} + 2f_{O_2} + f_{CO_2}}{3f_{H_2O} + 2f_{H_2} + 4f_{CH_4} + 2f_{O_2} + 2f_{CO_2} + f_{CO} + f_{N_2}} \quad (16)$$

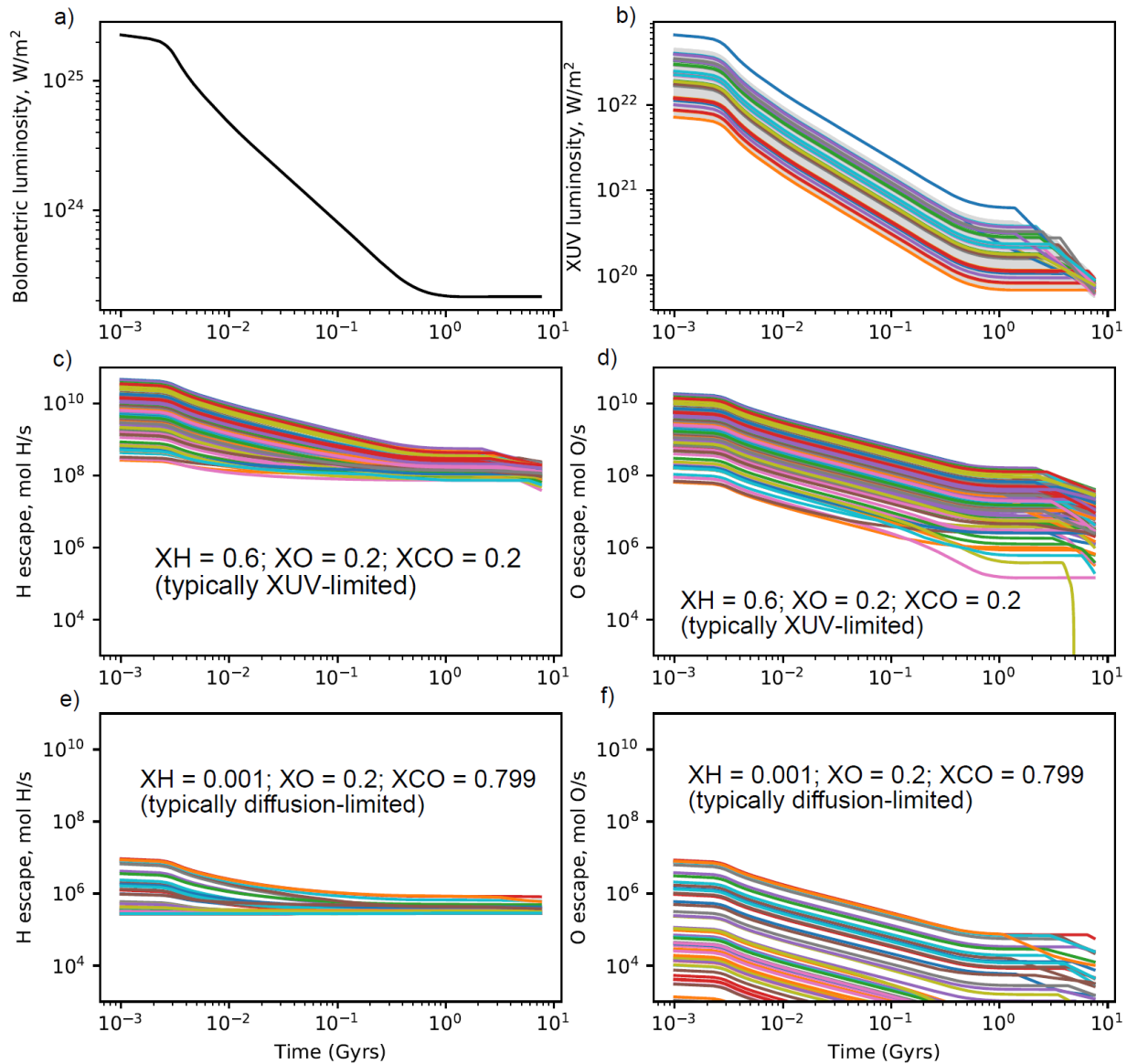
We assume that CO<sub>2</sub> is dissociated to CO and O, CO is robust against photodissociation, and that CH<sub>4</sub> can be treated as equivalent to CO for the purposes of estimating hydrodynamic loss of C. This means that the upper atmosphere CO abundance is given by:

$$f_{CO} = \frac{f_{CO} + f_{CO_2} + f_{CH_4}}{3f_{H_2O} + 2f_{H_2} + 4f_{CH_4} + 2f_{O_2} + 2f_{CO_2} + f_{CO} + f_{N_2}} \quad (17)$$

This approach is implicitly pessimistic about secondary atmosphere retention since we are effectively assuming well-mixed constituents all the way up to the exobase; this maximizes the abundance of high molecular weight constituents vulnerable to XUV-driven hydrodynamic drag. Accounting for the sedimentation of heavier species would only lower the amount of C and O that could be dragged to space.

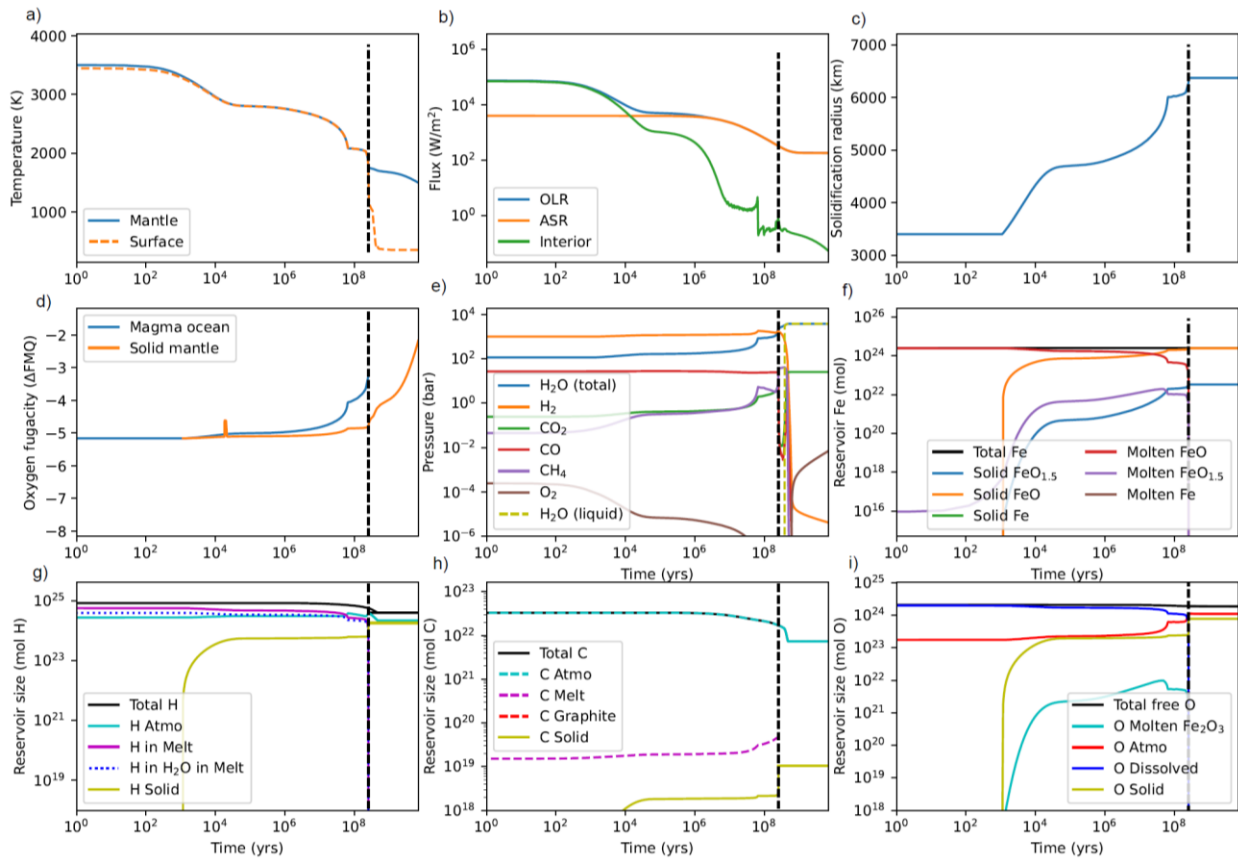
The combination of diffusion-limited and XUV-limited thermal escape parameterizations ensures diffusion-limited H escape for low stratospheric abundances, and a smoothly transition to XUV-driven escape as the upper atmosphere becomes steam or H<sub>2</sub> dominated [20]. The precise transition abundance is unknown and will, in general, depend on conductive and radiative cooling of the upper atmosphere as well as downward diffusive transport. Here, it is represented by the free parameter,  $\lambda_{tra}$ , which ranges from 10<sup>-6</sup> to 10<sup>1</sup> and is sampled uniformly in log space (corresponding to transition H mixing ratios from ~0.006 to 0.6). The efficiency of hydrodynamic escape is parameterized by loosely following the approach of Wordsworth et al. [21]. If the XUV-stellar flux is insufficient to drag oxygen, then the efficiency is equal to a constant,  $\epsilon_{lowXUV}$ , which is randomly sampled from 1% to 30%. Alternatively, if the XUV-stellar flux exceeds what is required to drag O, then some portion of the excess energy,  $\zeta_{high}$ , goes into driving further escape, whereas the rest,  $1 - \zeta_{high}$ , is assumed to be efficiently radiated away. The efficiency factor,  $\zeta_{high}$ , is randomly sampled from 0-100% for complete generality. See Krissansen-Totton et al. [20] for analytic expressions. We focus on XUV-driven mass loss rather than core-powered mass loss since this is expected to be the dominant mechanism for habitable zone, Earth-sized planets [22].

Fig. S5 illustrates example Monte Carlo stellar evolution and escape calculations. The top row of Fig S5 shows the input TRAPPIST-1 bolometric luminosity evolution and XUV luminosity evolution [23], respectively. The middle row shows show escape rates of H and O, respectively, for TRAPPIST-1b where an H-rich upper atmosphere is assumed (mixing ratio of atomic species, XH = 0.6, XO = 0.2, and XCO = 0.2). The bottom row of Fig S5 shows escape rates of H and O, respectively, for TRAPPIST-1b where an H-poor upper atmosphere is assumed (mixing ratio of atomic species, XH = 0.001, XO = 0.2, and XCO = 0.799). The individual lines represent luminosities and escape fluxes sampled from the full Monte Carlo ranges described in Table 1.



**Fig. S5: Illustrative stellar evolution and escape calculations showing Monte Carlo spread.** Subplot (a) shows input bolometric luminosity evolution of TRAPPIST-1, and (b) shows sampled input XUV luminosity evolution. Subplot (c) and (d) show H and O escape fluxes through time, respectively, for a H-rich atmosphere (XUV-limited regime) whereas (e) and (f) show H and O escape fluxes, respectively, for a H-poor atmosphere (diffusion-limited regime). For these illustrative calculations atmospheric composition is held constant to show the spread in fluxes as stellar luminosity evolves in time.

## Sensitivity Tests and Additional Results



**Fig. S6:** Identical to Fig. 3 in the main text showing TRAPPIST-1e with a large initial H endowment, but in this case we make the alternative endmember assumption whereby all metallic iron produced by hydrogen reducing FeO ( $\text{H}_2 + \text{FeO} \rightarrow \text{Fe} + \text{H}_2\text{O}$ ) is instantly sequestered in the metallic core. Subplot (a) denotes the time-evolution of surface (orange) and mantle potential temperature (blue), (b) denotes the evolution of outgoing longwave radiation (OLR, blue), absorbed shortwave radiation (ASR, orange), and interior heatflow (green), and subplot (c) shows the evolution of the magma ocean solidification front from the core-mantle boundary to the surface. Subplot (d) shows solid mantle (orange) and magma ocean redox (blue) relative to the Fayalite-Quartz-Magnetite (FMQ) buffer, (e) shows the evolution of atmospheric composition including  $\text{H}_2\text{O}$ ,  $\text{H}_2$ ,  $\text{CO}_2$ ,  $\text{CO}$ ,  $\text{CH}_4$ , and  $\text{O}_2$ . Subplot (f) denotes iron speciation in both the magma ocean and the solid silicate mantle. Subplot (g) shows both solid and fluid reservoirs of H including total dissolved hydrogen (purple) and hydrogen dissolved as  $\text{H}_2\text{O}$  (blue-dotted). Subplot (h) denotes solid and fluid reservoirs of C and subplot (i) denotes solid and fluid reservoirs of free oxygen, including oxygen bound to ferric iron, atmospheric species, and O in volatiles dissolved in the melt ( $\text{H}_2\text{O}$ ,  $\text{CO}_2$ ) reservoirs respectively. Vertical dashed black lines show the termination of the magma ocean.

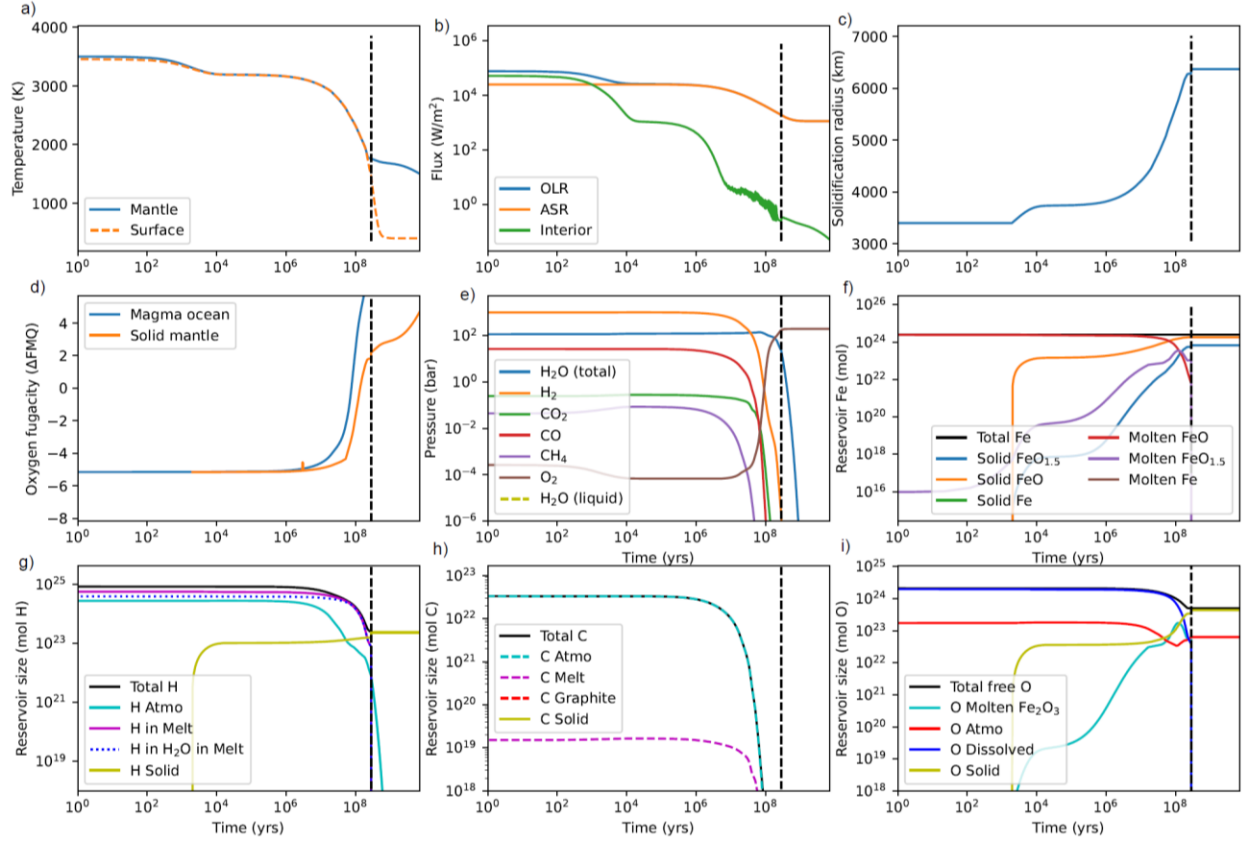


**Fig. S7:** Identical to Fig. 4 in the main text showing TRAPPIST-1b with a large initial H endowment, but in this case, we make the alternative endmember assumption whereby all metallic iron produced by hydrogen reducing FeO ( $\text{H}_2 + \text{FeO} \rightarrow \text{Fe} + \text{H}_2\text{O}$ ) is instantly sequestered in the metallic core. Subplot (a) denotes the time-evolution of surface (orange) and mantle potential temperature (blue), (b) denotes the evolution of outgoing longwave radiation (OLR, blue), absorbed shortwave radiation (ASR, orange), and interior heatflow (green), and subplot (c) shows the evolution of the magma ocean solidification front from the core-mantle boundary to the surface. Subplot (d) shows solid mantle (orange) and magma ocean redox (blue) relative to the Fayalite-Quartz-Magnetite (FMQ) buffer—the final surface is expected to be highly oxidized—(e) shows the evolution of atmospheric composition including  $\text{H}_2\text{O}$ ,  $\text{H}_2$ ,  $\text{CO}_2$ ,  $\text{CO}$ ,  $\text{CH}_4$ , and  $\text{O}_2$ . Subplot (f) denotes iron speciation in both the magma ocean and the solid silicate mantle. Subplot (g) shows both solid and fluid reservoirs of H including total dissolved hydrogen (purple) and hydrogen dissolved as  $\text{H}_2\text{O}$  (blue-dotted). Subplot (h) denotes solid and fluid reservoirs of C and subplot (i) denotes solid and fluid reservoirs of free oxygen, including oxygen bound to ferric iron, atmospheric species, and O in volatiles dissolved in the melt ( $\text{H}_2\text{O}$ ,  $\text{CO}_2$ ) reservoirs respectively. Vertical dashed black lines show the termination of the magma ocean.

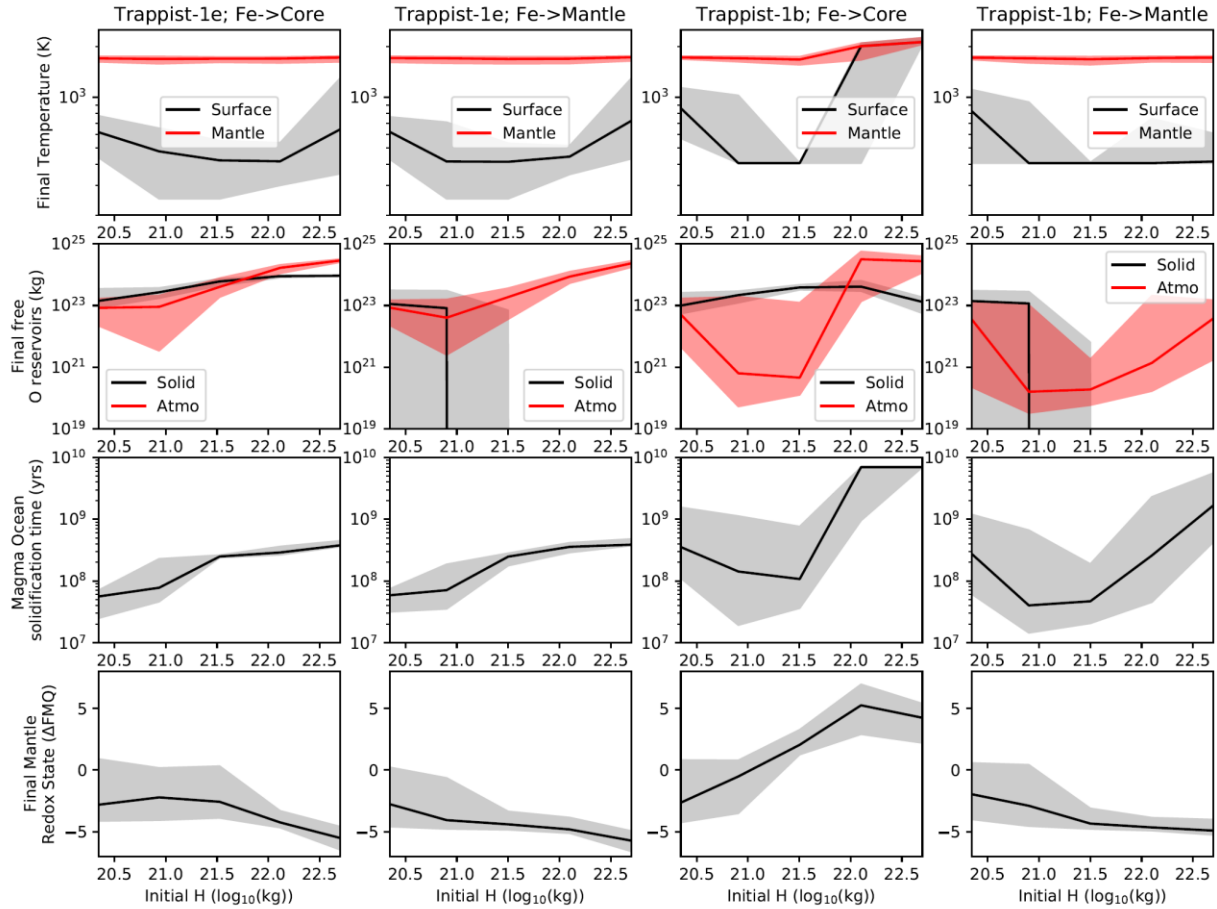


**Fig. S8:** Additional outputs from Monte Carlo calculations shown in Fig. 5 comparing outcomes for TRAPPIST 1e (left two columns) and TRAPPIST-1b (right two columns) after 8 Gyr of coupled atmosphere-interior-redox evolution, as a function of initial H endowment. Rows denote final mantle and surface temperatures (K), final atmosphere and interior free oxygen inventories (kg), the time taken for magma ocean solidification (years), and final mantle redox state relative to FMQ, respectively. The two columns for each planet denote endmember cases whereby all metallic iron is sequestered in the core (left), and all metallic iron remains in the silicate mantle (right). Solid lines and shaded regions denote median model outputs and 1-sigma confidence intervals, respectively. The negative free oxygen abundances indicate metallic iron exceeds ferric iron in the mantle (ferrous iron has zero free oxygen, metallic iron is effectively negative free oxygen – see methods). The magma ocean never solidifies in some cases for TRAPPIST-1b i.e. the solidification time equals the 8 Gyr age of the system. Finally, the final mantle redox state of TRAPPIST-1b may reflect whether metallic iron was sequestered in the core or remains in the mantle.

### Sensitivity to Planet Mass

In the nominal calculations, the mass and radii of TRAPPIST-1b and e were assumed to equal one Earth mass (and one Earth radii) respectively, to isolate the effects of differing instellation histories. Here, we perform a sensitivity test with the true mass and radii of each planet [24]. Results are shown in Fig S9 and are very similar to nominal calculations.

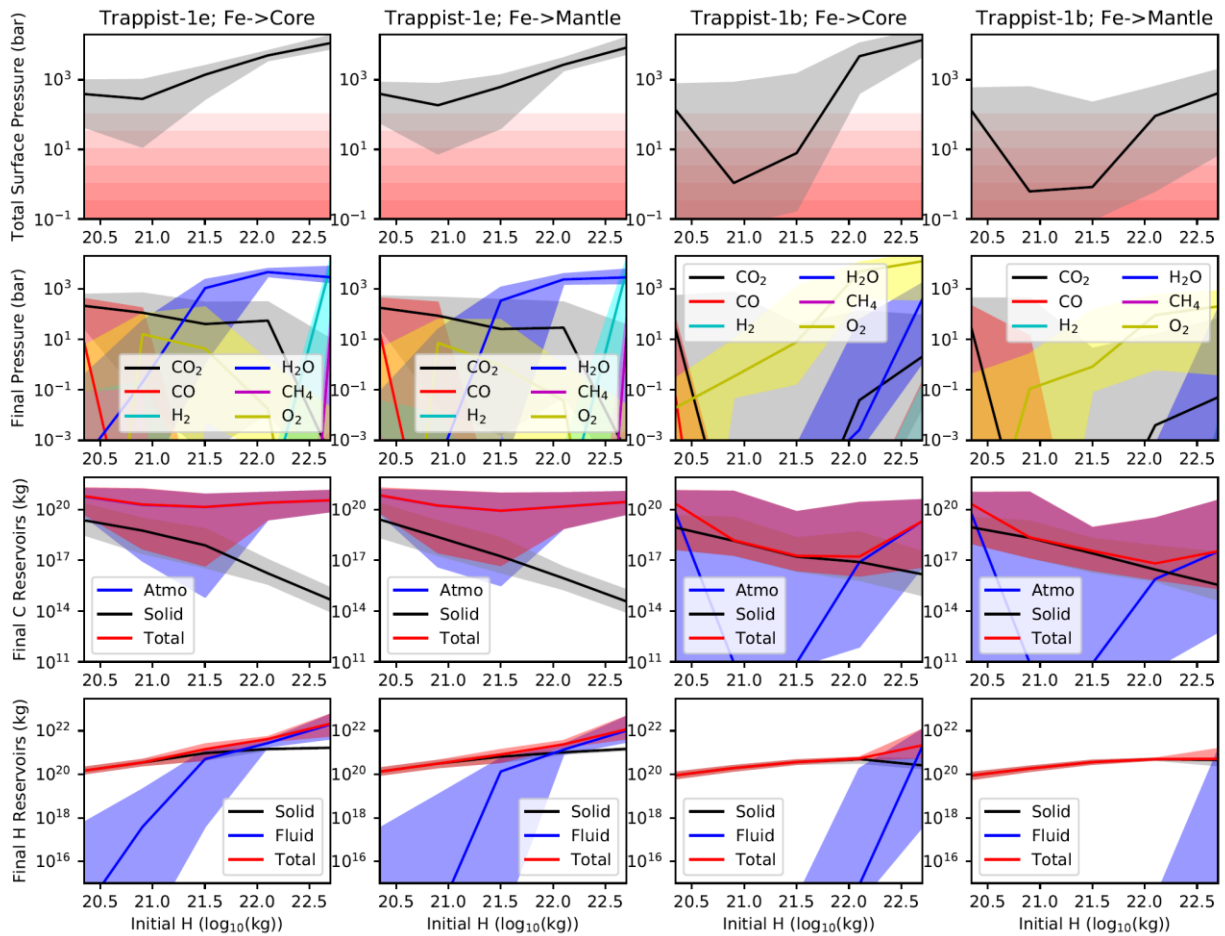


**Fig. S9:** Identical to Fig. 5 in the main text except that the true mass and radii of TRAPPIST-1e and b are assumed [24].

### Sensitivity to initial mantle FeO

In all nominal calculations in the main text, an Earth-like mantle FeO fraction was assumed (mole fraction 0.06). We repeated all nominal calculations with both smaller (0.02) and larger (0.2) initial FeO mole fractions to test sensitivity to this assumption. This range encompasses the range of silicate mantle iron content for solar system bodies, and differentiated exoplanets are likely to inherit similar compositions given expected silicate-metal elemental partitioning [25] and the muted variability in stellar rock-forming element abundances [26]. Fig. S10 shows the low initial iron case. Broadly speaking, results are similar to nominal calculations because there is still plenty of FeO available to be reduced. Fig. S11 shows the high initial FeO case, which results in somewhat higher final surface water inventories for TRAPPIST-1e since more iron oxide is available to be reduced. For TRAPPIST-1b, results are qualitatively similar to nominal calculations.

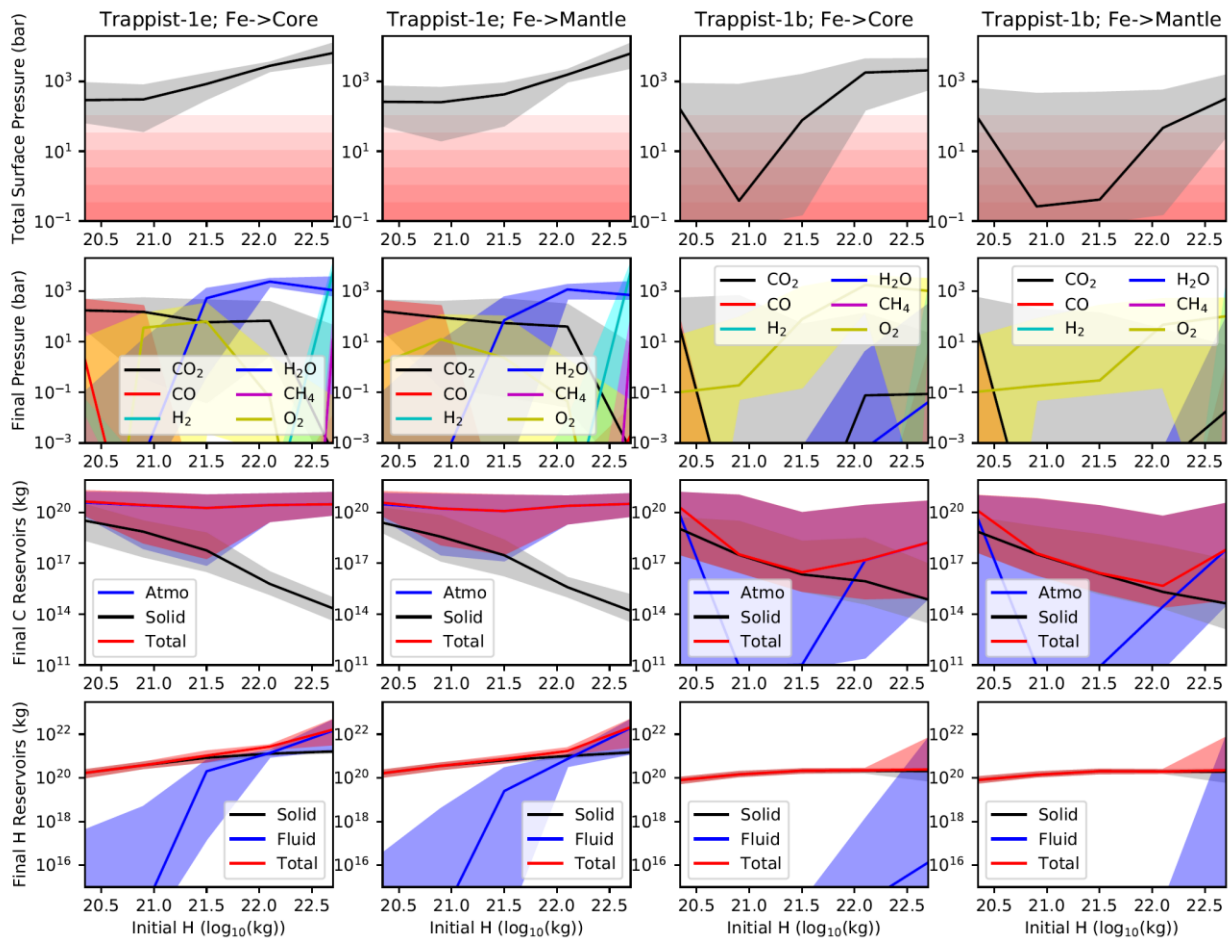


**Fig. S10:** Identical to Fig. 5 in the main text except that the initial mantle iron oxide content is three times smaller than that of the Earth.

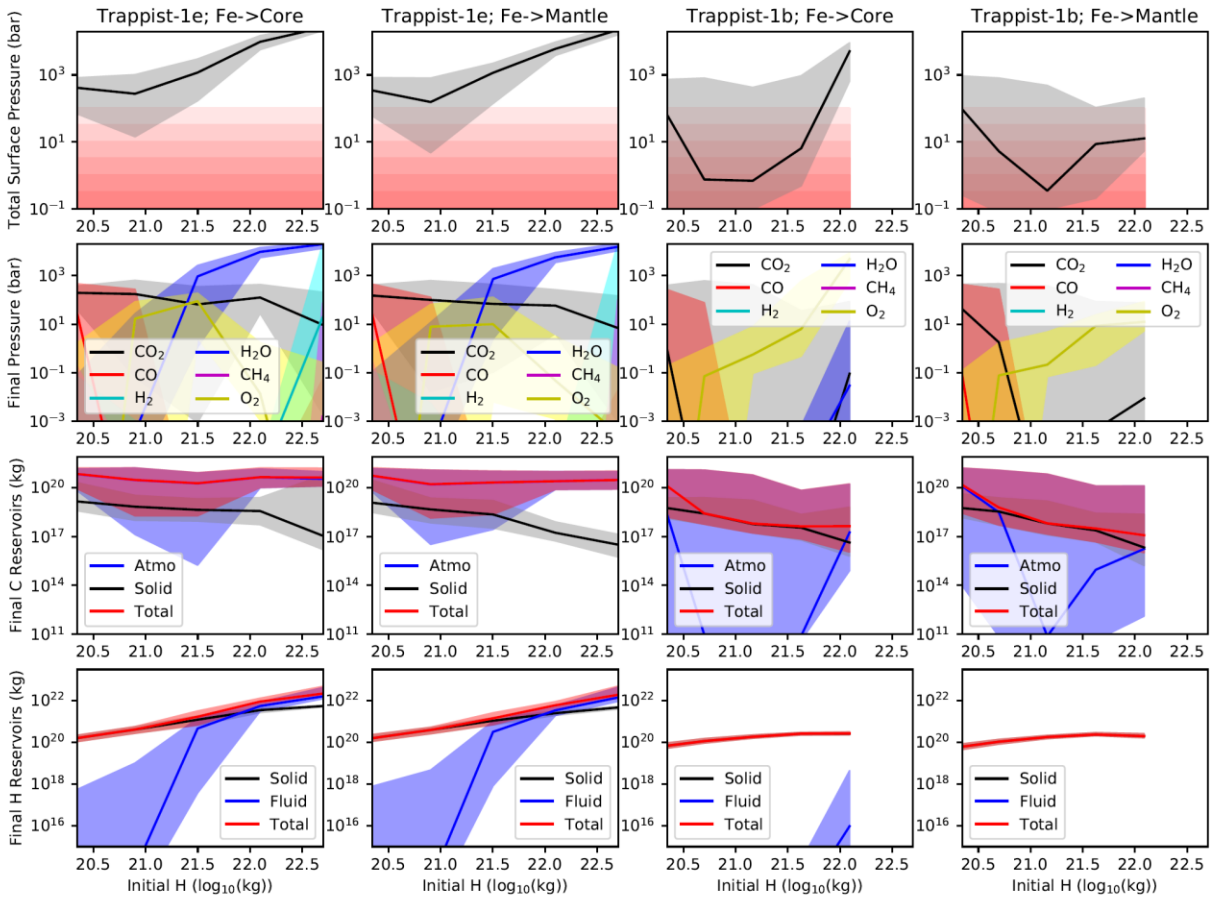


**Fig. S11:** Identical to Fig. 5 in the main text except that the initial mantle iron oxide content is three times greater than that of the Earth. Note that model failure rates are higher for high initial H due to the very large surface volatile inventories that are generated.

## Sensitivity to atmospheric structure

In all nominal calculations in the main text, an adiabatic deep atmosphere is assumed, which neglects the possibility of a transition to a deep radiative zone [27]. We thus recomputed our climate grid assuming an isothermal atmospheric structure below 100 bar to bookend the two plausible endmember cases for the deep atmosphere (adiabat vs. isotherm). Fig. S12 and S13 show the results of these calculations for TRAPPIST-1e. Unsurprisingly, an isothermal deep atmosphere leads to cooler surface temperatures and shorter duration magma oceans (Fig S13). However, overall qualitative outcomes for TRAPPIST-1e are similar to the nominal model because the escape fluxes are most strongly influenced by luminosity evolution and the runaway greenhouse duration, neither of which are changed by assuming a deep isothermal atmosphere. Hydrogen-rich atmospheres are slightly more likely to be retained for the cooler (deep isotherm) cases.

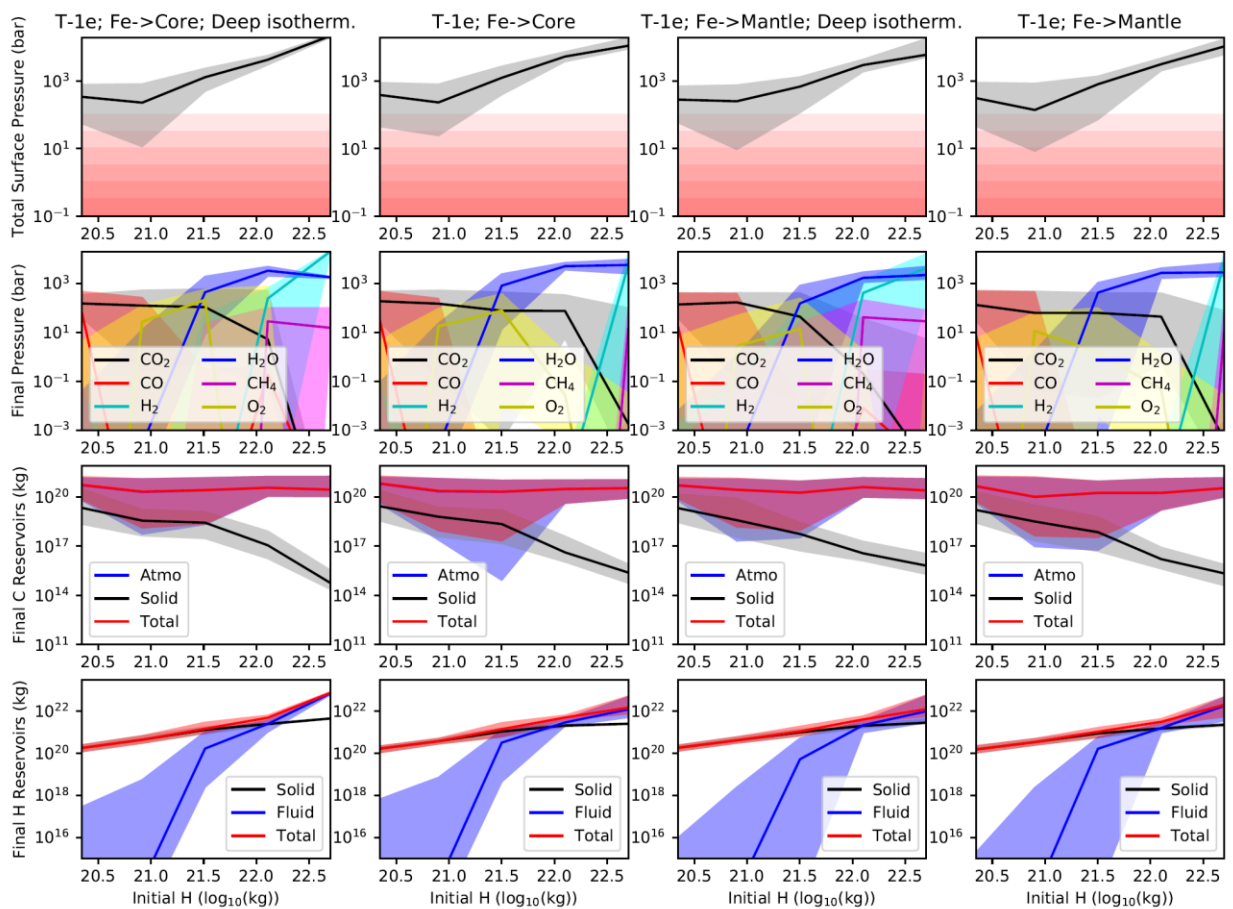


**Fig. S12:** Calculations repeated for TRAPPIST-1e using a climate model with a deep isotherm (below 100 bar) to simulate a radiative deep atmosphere. Results are qualitatively similar to nominal calculations because escape is primarily governed by stellar bolometric and XUV evolution, and not by the temperature evolution of the atmosphere-interior interface.

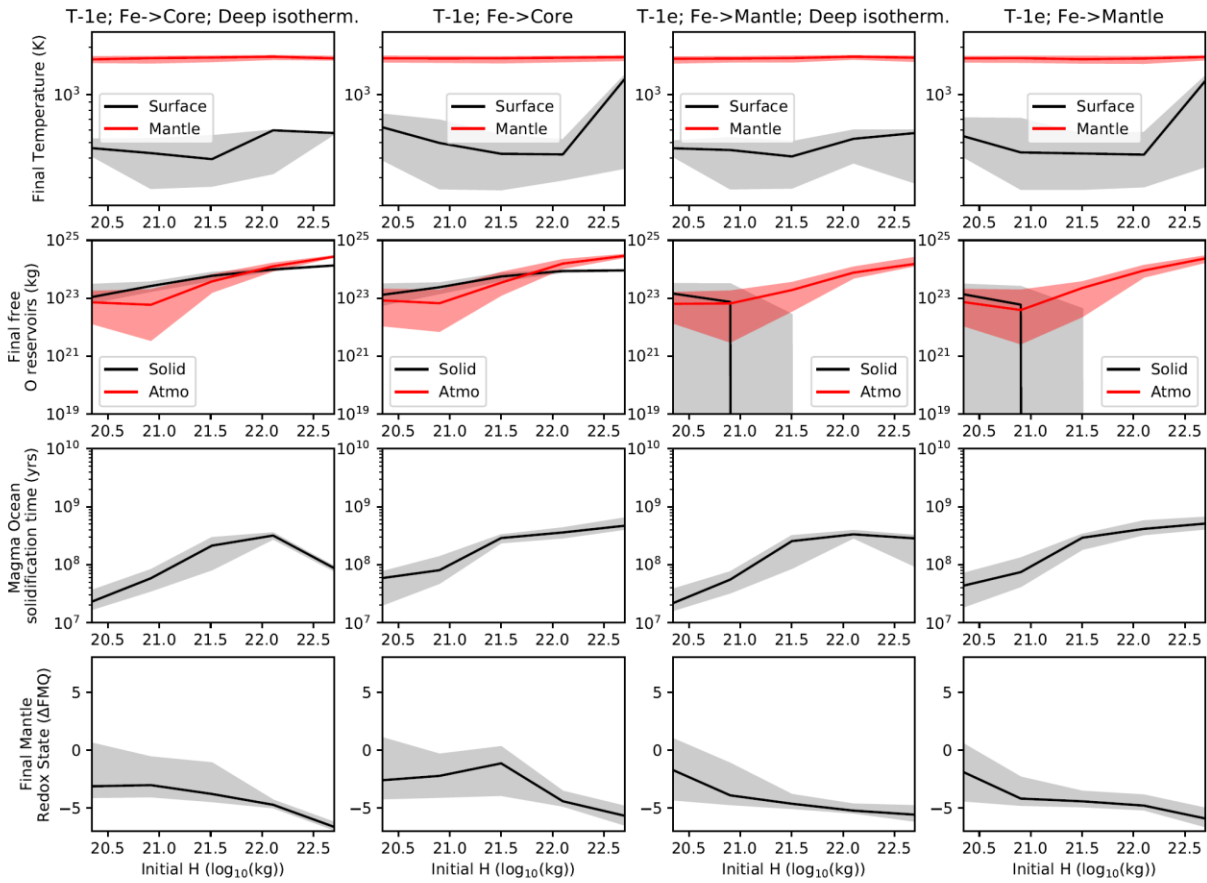


**Fig. S13:** Additional outputs from deep isotherm sensitivity test shown in Fig. S12 comparing outcomes for TRAPPIST 1e. A radiative deep atmosphere results in cooler surface temperatures and shorter duration magma oceans compared to nominal calculations.

## Sensitivity to clouds

In all nominal calculations in the main text a low albedo is assumed to represent the cloud-free magma ocean state (values between 0 and 0.2 are sampled in Monte Carlo calculations). This maximizes the duration of the runaway greenhouse compared to cloudy scenarios, and by extension the longevity of hydrodynamic escape. However, to test the effect of albedo on our results we repeated calculations using a higher albedo range (0.5-0.7) to represent continuously cloudy or hazy atmospheres, as shown in Fig. S14 and S15. While surface temperatures are slightly cooler and the typical duration of the magma ocean is a factor of a few shorter for the high albedo cases, atmospheric composition outcomes are largely unchanged.

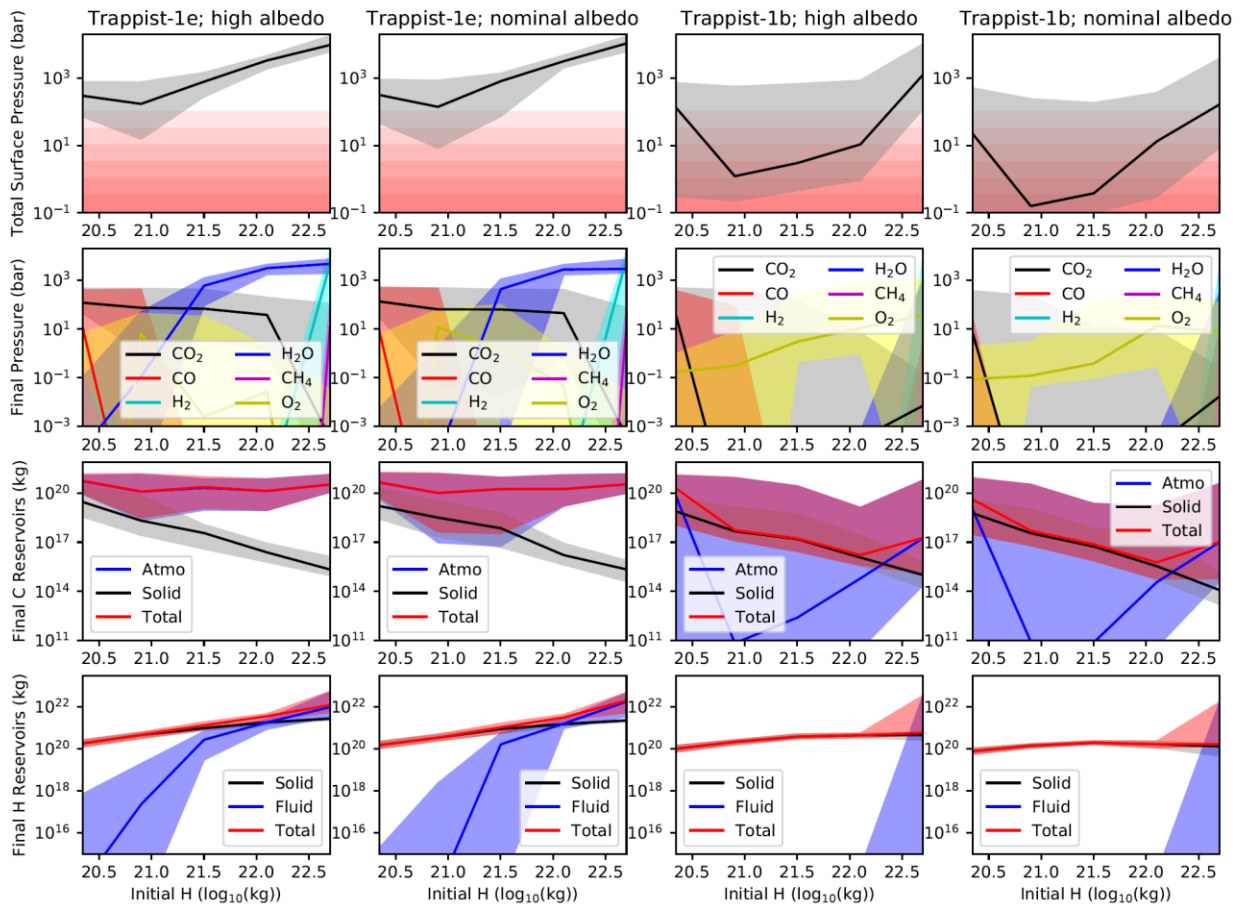


**Fig. S14:** Calculations repeated for TRAPPIST-1e and b but with a higher albedo range (0.5-0.7) compared to low albedos sampled in the nominal calculations (0-0.2). Slightly less C is lost in the cooler, high albedo cases, but results are qualitatively very similar to nominal calculations.

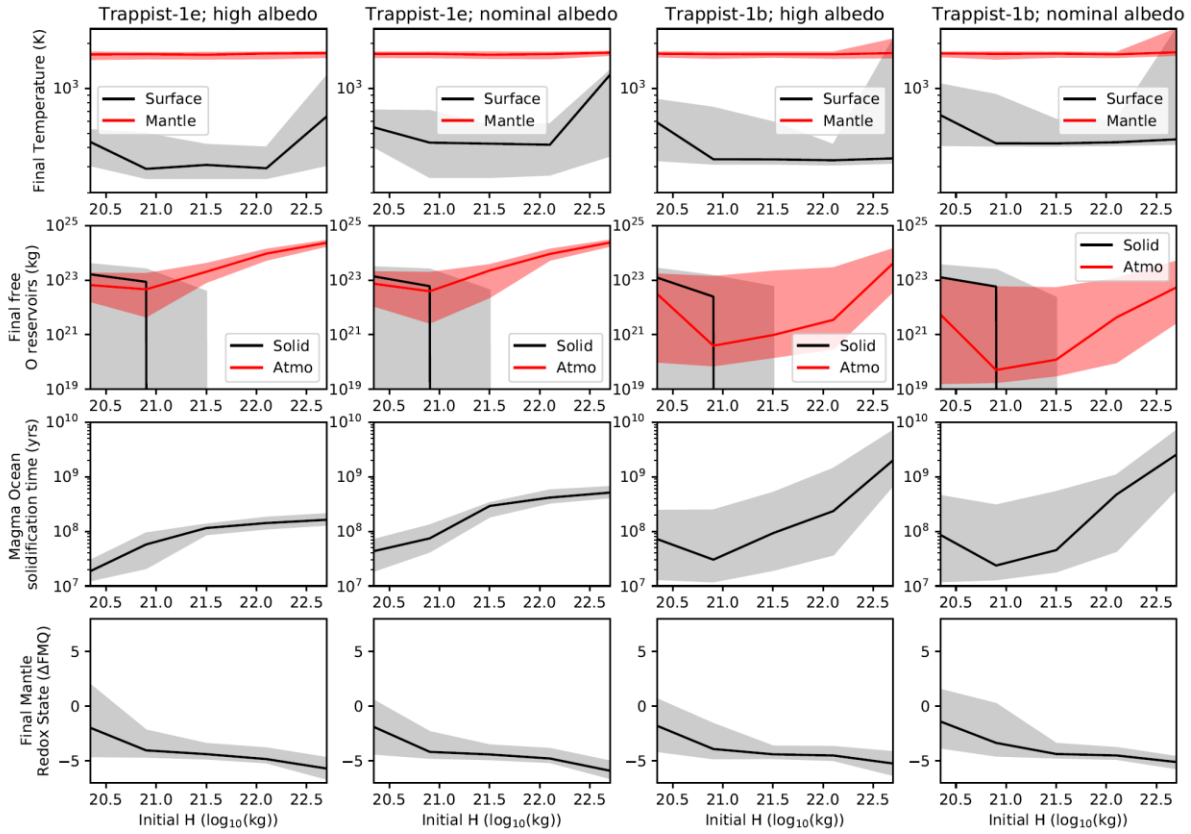


**Fig. S15:** Additional outputs from high albedo sensitivity test shown in Fig. S14 comparing outcomes for TRAPPIST 1e and b. Surface temperatures are cooler, and the typical duration of the magma ocean is a factor of a few smaller for the high albedo cases, but this is not sufficient to dramatically change atmosphere-interior evolution.

## Sensitivity to melt trapping

In all nominal calculations in the main text, melt is trapped in the solidifying mantle using the parameterization described in Krissansen-Totton and Fortney [28] and Hier-Majumder and Hirschmann [2], which does not permit trapped melt fractions above 0.3. This may potentially underestimate the amount of volatiles trapped inside the mantle if the rheological transition occurs at higher melt fractions [29], or if melt concentrations vary as a function of melt fraction [30]. To test the influence of greater melt trapping at higher solidification rates, we increased the maximum trapped melt fraction to 0.8 and repeated calculations for TRAPPIST-1b and e (Fig. S16). This does not substantially change atmospheric outcomes since the pace of magma ocean solidification is determined by stellar bolometric luminosity evolution and is typically slow. Because compaction is rapid compared to solidification timescales, equilibration of volatiles between melt phases and the atmosphere will occur.

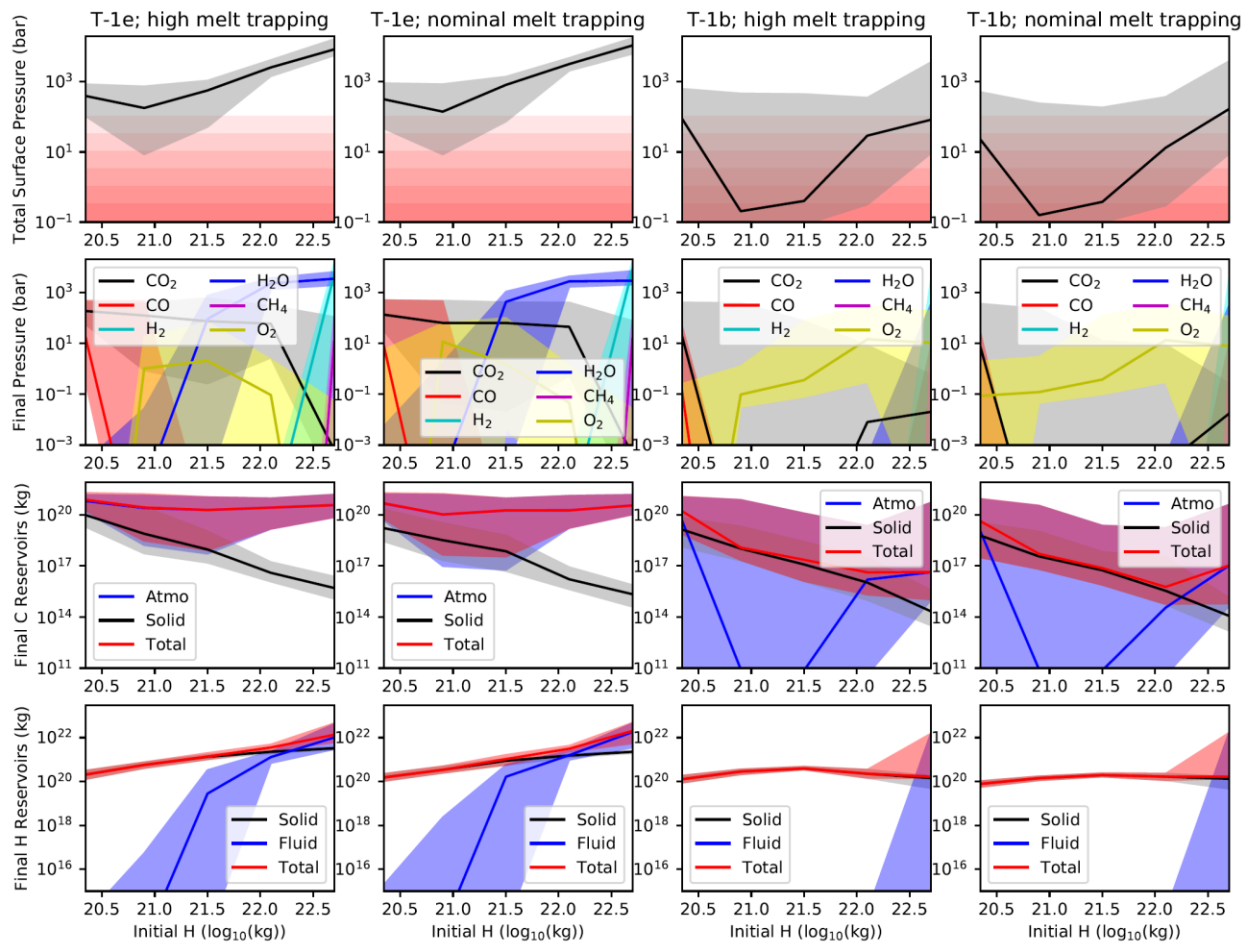


**Fig. S16:** Calculations repeated for TRAPPIST-1e and b but with a higher maximum trapped melt fraction (0.8) compared to nominal calculations (0.3). Results are largely insensitive to melt trapping assumptions, except that slightly more C is retained in the mantle for fast solidification (low initial H) model runs.

## Application to other planetary systems

To establish our results are not specific to the TRAPPIST-1 system, we repeated calculations for LP 890-9 (Fig. S17) and Proxima Centauri (Fig. S18). The LP 890-9 system [31] contains a highly irradiated super Earth, b ( $1.32R_{\oplus}$ , assumed mass  $2.3 M_{\oplus}$ ), and a potentially habitable super Earth, c ( $1.37 R_{\oplus}$ , assumed mass  $2.5 M_{\oplus}$ ) orbiting an M6 star. Proxima Centauri b is an Earth-sized ( $1.07 M_{\oplus}$ , assumed radius  $1.2 R_{\oplus}$ ) orbiting within the habitable zone ( $0.65 S_{\oplus}$ ) of its M5 host [32]. Calculations for TRAPPIST-1f are also included to show the potential impact of lowering equilibrium temperature. For all planets, bolometric luminosity evolution is interpolated from Baraffe et al. [33] and TRAPPIST-1 XUV evolution [23] is assumed to maximize XUV-driven escape potential. Despite this pessimistic assumption, we find all habitable zone planets are likely to retain substantial inventories of surface water for initial hydrogen endowments greater than BSE (analogous to TRAPPIST-1e in the main text). Similarly, the Venus analog LP 890-9 b is far more likely to have stripped of all surface volatiles, although note that this is slightly less likely than for TRAPPIST-1b owing to LP 890-9 b's higher gravity.

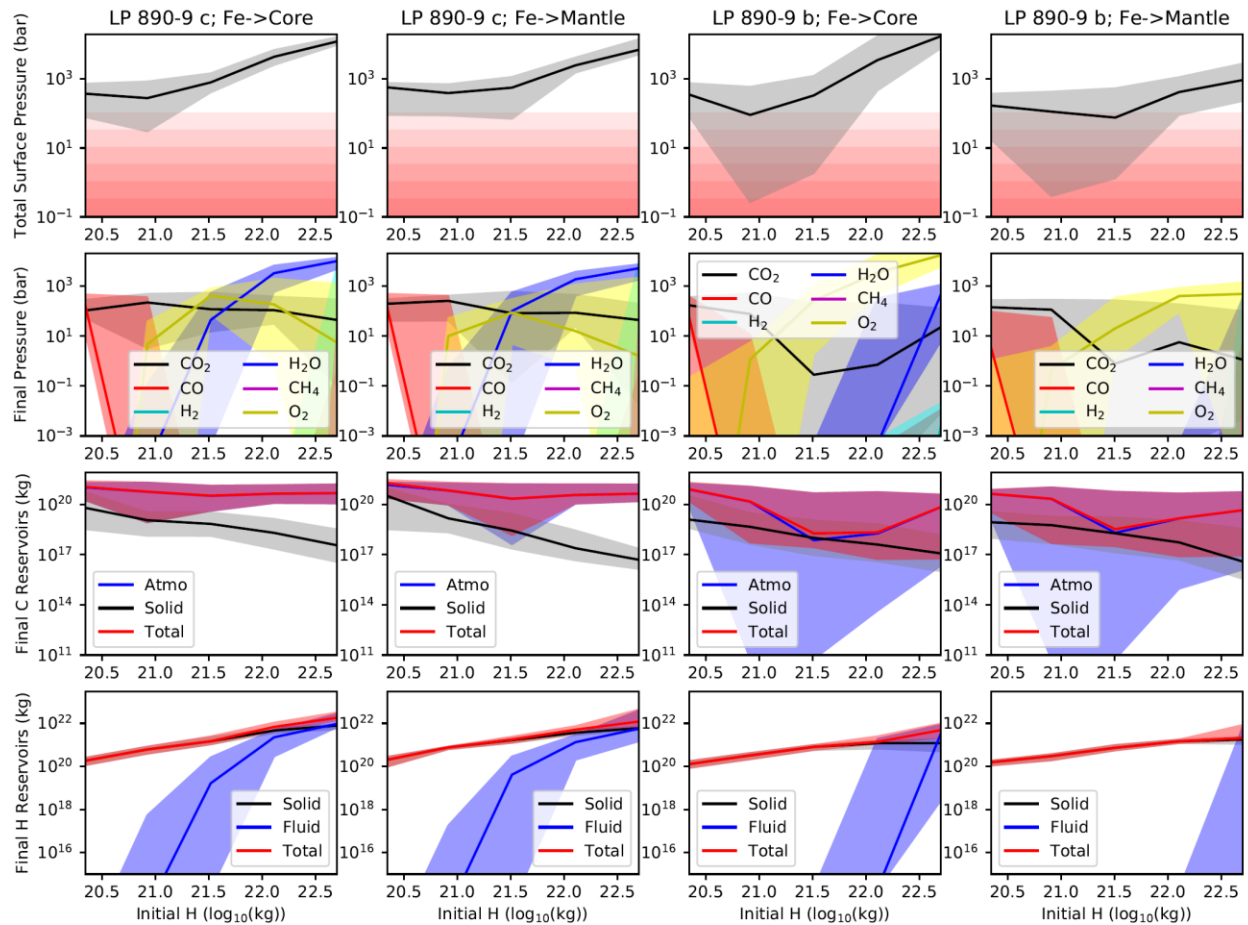


**Fig. S17:** Identical to Fig. 5 in the main text except calculations are applied to the potentially habitable  $0.906 \pm 0.026 S_{\oplus}$  LP 890-9 c (left) and the highly irradiated ( $4.09 \pm 0.12 S_{\oplus}$ ) LP 890-9 b (right).

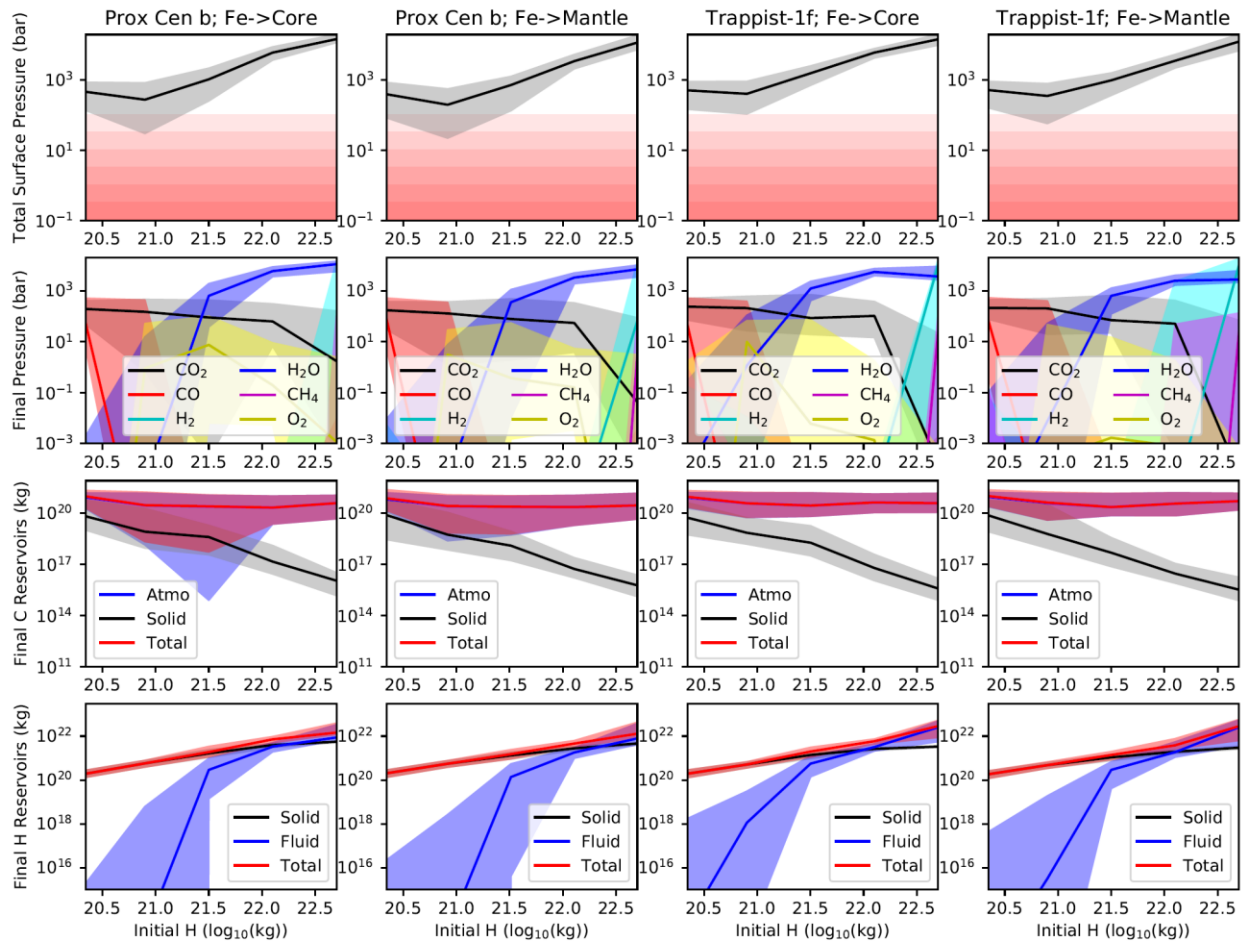


**Fig. S18:** Identical to Fig. 5 in the main text except calculations are applied to the habitable zone terrestrial planets Proxima Centauri b (left) and TRAPPIST-1f (right).

### Supplementary References

1. Miyazaki, Y. and J. Korenaga, *Inefficient water degassing inhibits ocean formation on rocky planets: An insight from self-consistent mantle degassing models*. *Astrobiology*, 2022. **22**(6): p. 713-734.
2. Hier-Majumder, S. and M.M. Hirschmann, *The origin of volatiles in the Earth's mantle*. *Geochemistry, Geophysics, Geosystems*, 2017. **18**(8): p. 3078-3092.
3. Bower, D.J., et al., *Retention of water in terrestrial magma oceans and carbon-rich early atmospheres*. *The planetary science journal*, 2022. **3**(4): p. 93.
4. Sossi, P.A., et al., *Solubility of water in peridotite liquids and the prevalence of steam atmospheres on rocky planets*. *Earth and Planetary Science Letters*, 2023. **601**: p. 117894.
5. Kadoya, S., J. Krissansen-Totton, and D.C. Catling, *Probable cold and alkaline surface environment of the Hadean Earth caused by impact ejecta weathering*. *Geochemistry, Geophysics, Geosystems*, 2020. **21**(1): p. e2019GC008734.

6. Sleep, N.H. and K. Zahnle, *Carbon dioxide cycling and implications for climate on ancient Earth*. Journal of Geophysical Research: Planets, 2001. **106**(E1): p. 1373-1399.
7. Hamano, K., Y. Abe, and H. Genda, *Emergence of two types of terrestrial planet on solidification of magma ocean*. Nature, 2013. **497**(7451): p. 607-610.
8. Lebrun, T., et al., *Thermal evolution of an early magma ocean in interaction with the atmosphere*. Journal of Geophysical Research: Planets, 2013. **118**(6): p. 1155-1176.
9. Salvador, A., et al., *The relative influence of H<sub>2</sub>O and CO<sub>2</sub> on the primitive surface conditions and evolution of rocky planets*. Journal of Geophysical Research: Planets, 2017. **122**(7): p. 1458-1486.
10. Ortenzi, G., et al., *Mantle redox state drives outgassing chemistry and atmospheric composition of rocky planets*. Scientific Reports, 2020. **10**(1): p. 1-14.
11. Kress, V.C. and I.S. Carmichael, *The compressibility of silicate liquids containing Fe<sub>2</sub>O<sub>3</sub> and the effect of composition, temperature, oxygen fugacity and pressure on their redox states*. Contributions to Mineralogy and Petrology, 1991. **108**: p. 82-92.
12. O'Neill, H., *Cosmochemical estimates of mantle composition*, in *Treatise on Geochemistry: Oxford*. 2014, Elsevier. p. 1-39.
13. Hirschmann, M., *Magma oceans, iron and chromium redox, and the origin of comparatively oxidized planetary mantles*. Geochimica et Cosmochimica Acta, 2022. **328**: p. 221-241.
14. Ma, Z., *Thermodynamic description for concentrated metallic solutions using interaction parameters*. Metallurgical and Materials Transactions B, 2001. **32**: p. 87-103.
15. Frost, B.R., *Introduction to oxygen fugacity and its petrologic importance*, in *Oxide minerals*. 2018, De Gruyter. p. 1-10.
16. Catling, D.C. and J.F. Kasting, *Atmospheric Evolution on Inhabited and Lifeless Worlds*. 2017: Cambridge University Press.
17. Marrero, T.R. and E.A. Mason, *Gaseous diffusion coefficients*. Journal of Physical and Chemical Reference Data, 1972. **1**(1): p. 3-118.
18. Zahnle, K.J. and J.F. Kasting, *Mass fractionation during transonic escape and implications for loss of water from Mars and Venus*. Icarus, 1986. **68**(3): p. 462-480.
19. Odert, P., et al., *Escape and fractionation of volatiles and noble gases from Mars-sized planetary embryos and growing protoplanets*. Icarus, 2018. **307**: p. 327-346.
20. Krissansen-Totton, J., et al., *Oxygen false positives on habitable zone planets around sun-like stars*. AGU Advances, 2021. **2**(e2020AV000294).
21. Wordsworth, R., L. Schaefer, and R. Fischer, *Redox Evolution via Gravitational Differentiation on Low-mass Planets: Implications for Abiotic Oxygen, Water Loss, and Habitability*. The Astronomical Journal, 2018. **155**(5): p. 195.
22. Owen, J.E. and H.E. Schlichting, *Mapping out the parameter space for photoevaporation and core-powered mass-loss*. Monthly Notices of the Royal Astronomical Society, 2024. **528**(2): p. 1615-1629.
23. Birky, J., R. Barnes, and D.P. Fleming, *Improved Constraints for the XUV Luminosity Evolution of Trappist-1*. Research Notes of the AAS, 2021. **5**(5): p. 122.
24. Agol, E., et al., *Refining the transit-timing and photometric analysis of TRAPPIST-1: masses, radii, densities, dynamics, and ephemerides*. The planetary science journal, 2021. **2**(1): p. 1.
25. Schlichting, H.E. and E.D. Young, *Chemical Equilibrium between Cores, Mantles, and Atmospheres of Super-Earths and Sub-Neptunes and Implications for Their Compositions, Interiors, and Evolution*. The Planetary Science Journal, 2022. **3**(5): p. 127.
26. Hinkel, N.R., et al., *Stellar abundances in the solar neighborhood: the Hypatia Catalog*. The Astronomical Journal, 2014. **148**(3): p. 54.
27. Selsis, F., et al., *A cool runaway greenhouse without surface magma ocean*. Nature, 2023. **620**(7973): p. 287-291.

28. Krissansen-Totton, J. and J.J. Fortney, *Predictions for Observable Atmospheres of Trappist-1 Planets from a Fully Coupled Atmosphere–Interior Evolution Model*. The Astrophysical Journal, 2022. **933**(1): p. 115.
29. Costa, A., L. Caricchi, and N. Bagdassarov, *A model for the rheology of particle-bearing suspensions and partially molten rocks*. Geochemistry, Geophysics, Geosystems, 2009. **10**(3).
30. Salvador, A. and H. Samuel, *Convective outgassing efficiency in planetary magma oceans: insights from computational fluid dynamics*. Icarus, 2023. **390**: p. 115265.
31. Delrez, L., et al., *Two temperate super-Earths transiting a nearby late-type M dwarf*. Astronomy & Astrophysics, 2022. **667**: p. A59.
32. Anglada-Escudé, G., et al., *A terrestrial planet candidate in a temperate orbit around Proxima Centauri*. Nature, 2016. **536**(7617): p. 437-440.
33. Baraffe, I., et al., *New evolutionary models for pre-main sequence and main sequence low-mass stars down to the hydrogen-burning limit*. Astronomy & Astrophysics, 2015. **577**: p. A42.